

A Multi-Phase Flow Model Incorporated with Population Balance Equation in a Meshfree Framework

Vikash Kumar Sharma

Vom Fachbereich Mathematik
der Technischen Universität Kaiserslautern
zur Verleihung des akademischen Grades
Doktors der Naturwissenschaften
(Doktor rerum naturalium, Dr. rer. nat.)
genehmigte Dissertation.

1. Gutachter: Prof. Dr. Axel Klar
2. Gutachter: Prof. Dipl.-Ing. Dr. techn. Hans-Jörg Bart

Datum der Disputation: 04 March 2011

D386

To the memories of my late father

Acknowledgements

The life of a PhD student has never been easy but I have certainly relished this experience. During this period I derived my inspiration from several sources and now I want to express my deepest gratitude to all those sources.

Foremost, I owe thanks to my supervisor Prof. Dr. Axel Klar who has not only encouraged me but has given his remarkable suggestions and invaluable supervision throughout my thesis.

Now I would like to express my sincere gratitude to Dr. Sudarshan Tiwari for his advices, continuous encouragement and support right from the start to the end which have always been the driving force towards the successful completion of my thesis.

I must thank Prof. Menwer Attarakih for his assistance and valuable suggestions and Dr. Jörg Kuhnert for his advices and discussions. I would like to thank to Prof. S. Sundar for his encouragements and Mr. Moutasem Jaradat for his cooperation.

I am very grateful for the fruitful working environments provided by the Department of Mathematics at the University of Kaiserslautern. I like to thank to my colleagues and friends with whom I had a wonderful time and had very helpful discussions. I special thanks to Mr. Mark Kimathi for proof-reading the manuscript and Mr. Prabhath Liyanage for his friendly nature and ready-to-help attitude.

Now I would like to express my deep obligation to my parents and relatives back home in India. Their consistent mental supports have always been the strong push for me during this period. I am greatly indebted to my wife Rajani Rai and my son Agrim Sharma for their support and patience.

Finally, I thank the financial support I received from DAAD (Deutscher Akademischer Austausch Dienst) for the pursuit of this research work. The partial support from the Technical University of Kaiserslautern is also acknowledged.

Contents

1	General Introduction	1
1.1	Overview	1
1.2	Outline of Contents	5
2	Multiphase Flow Model and Numerical Approach	7
2.1	CFD-PBM Coupled Model	7
2.1.1	General overview of a model	7
2.1.2	Spatially Distributed Population Balance Equation	9
2.1.3	Fluid Dynamics Equations	11
2.1.4	Reduced Model with OPOSPM	13
2.1.5	Model with MPOSPM	15
2.2	Hyperbolicity Analysis of the CFD-PBM Coupled Model	16
2.2.1	Formulations	16
2.2.2	Mathematical Property of the Model Equations	18
2.3	Finite Pointset Method (FPM)	20
2.3.1	Least Square Approximation	20
2.4	Numerical Approach	23
3	Population Balances	27
3.1	Population Balance Equation	27
3.1.1	Breakage Process	30
3.1.2	Aggregation Process	31
3.1.3	The Bivariate Population Balance Equation (BPBE)	32

3.2	Method of Solving the PBE	33
3.2.1	Analytical Methods	34
3.2.2	Numerical Methods	43
3.2.3	Comparison of Numerical Methods	67
4	Momentum Transfer Between Liquid-Liquid Phases	71
4.1	FPM-OPOSPM Solver	71
4.1.1	The PBE without Source Term	72
4.1.2	The PBE with Source Term	76
4.1.3	Non-Constant Breakage and Coalescence Kernels	80
4.1.4	Realistic Breakage and Coalescence Kernels	83
4.1.5	Pilot Plant RDC (height 2.55m)	84
4.1.6	Pilot Plant RDC (height 4.0m)	87
4.1.7	Simulation of a Kuehni Column (DN-150)	89
4.2	FPM-MPOSPM Solver	92
4.2.1	Two-Fluid Model	92
4.2.2	Multi-Fluid Model	99
5	Mass Transfer Between Liquid-Liquid Phases	105
5.1	Influence of Breakage and Coalescence Kernels	105
5.2	Influence of Mass Transfer Coefficient	107
5.2.1	Constant Mass Transfer Coefficient	107
5.2.2	Realistic Mass Transfer Coefficient	108
6	Conclusion	113
A		115
A.1	Analytical formulation of the velocity of the continuous phase	115
B		117
B.1	Length-based form of PBE (Population Balance Equation)	117
C		119
C.1	Product Difference Algorithm (P-D Algorithm)	119

Chapter 1

General Introduction

In this chapter a general overview of a meshfree coupled model of Computational Fluid Dynamics (CFD) and Population Balance Equation (PBE) is provided.

1.1 Overview

This thesis is concerned with the coupling of fluid dynamics equations and population balance modelling for a liquid-liquid extraction column (see Figure 1.1) in a mesh free framework. Liquid-liquid Extraction Columns (LLEC) are one of the major multiphase contacting equipment that received a wide industrial acceptance in many fields of engineering such as hydrometallurgical, nuclear, petrochemical, pharmaceutical, and food industries. These equipments are characterized by the presence of a continuous phase and a dispersed phase composed of particles (the particles are supposed to be drops or bubbles in the liquid-liquid extraction columns) with a distribution of properties. However, the optimal design of such equipment has not yet been fulfilled and is still dependent on the time consuming and expensive scale up methods. This is due to the complex nature of the macroscopic dispersed phase interactions as well as the microscopic inter phase mass transfer occurring in the continuously turbulent flow field. These macroscopic interactions such as droplet breakage and coalescence coupled with the interphase mass transfer result in a distributed population of droplets. This population is distributed not only in the spatial domain of the contacting equipment, but also randomly distributed with respect to the droplet state (properties) such as size, concentration and age. The hydrodynamic and mass transfer interactions could be simulated using the population balances as an effective

framework taking into account the bivariate nature (with respect to droplet size and concentration) of the spatially distributed population in the interacting liquid-liquid dispersions. So, in contrast to the previous spatially distributed population balance equation (SDPBE) describing the performance of the LLECs [1, 2], this modeling approach allows the dynamic interaction of the mass transfer and fluid hydrodynamics by leaving it open to introduce a suitable model for predicting the interfacial tension, which changes with the mass transfer and markedly affects the breakage and coalescence rates [3].

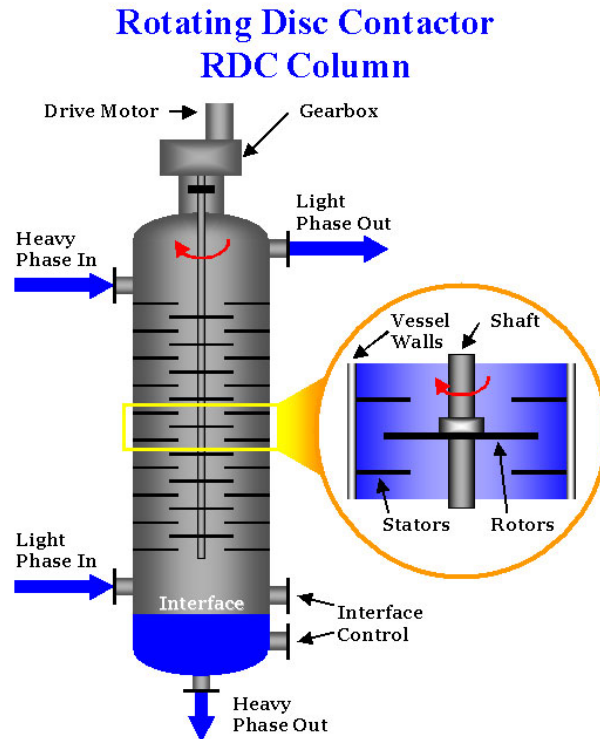


Figure 1.1: Rotating disc contactor (RDC).

In the simulation and layout of liquid-liquid extraction columns the dispersed phase is classically assumed as a pseudo homogeneous phase, where one parameter accounts for all deviations from the ideal plug flow behaviour. Furthermore, the accurate prediction of the dispersed phase evolution depends strongly on the proper modelling of the continuous flow fields and hydrodynamics in which the droplets are dispersed. Up to now the design of an extraction column without experimental pilot plant experiments has not been feasible. In current droplet Population Balance Model (PBM) codes [4], the

dispersion model is still used for the description of the hydrodynamics and results from small scale devices (single droplet experiments) are needed to predict the average diameter, number density and hold-up profiles [5, 45]. On the other hand, Computational Fluid Dynamics (CFD), based on a mono-disperse assumption, can predict the flow fields and hydrodynamics in a stirred liquid-liquid extraction column and deliver all necessary information for the population balance model [7, 8]. In order to properly model hydrodynamics and mass transfer interactions in an extraction column without the need for pilot plant or small scale device experiments, the population balance must be coupled with turbulent CFD modelling. Only a few researchers investigated combined CFD-PBM models in the field of liquid-liquid extraction so far and achieved encouraging results for the combined models [9, 10]. Hence, the work during this thesis focuses on a combined CFD and PBM to advance in this promising field of research.

In this study we use a meshfree Lagrangian method, called the Finite Pointset Method (FPM) to solve the model equations. Our main goal is to incorporate the PBM into the FPM code. We first start filling the fluid domain with finite number of points (or particles), which are the numerical grids. These points move with fluid velocities and together with them carry all fluid quantities, like velocity, density, etc., which are necessary to solve fluid dynamic equations. One of the most important process of this method is the maintenance of the good quality of particle distribution. After a movement of particles, they may scatter from each other and create holes in the computational domain and the method becomes unstable. Therefore, one has to add new particles if there exists holes. Moreover, particles may come very close to each other, in this case one can keep one particle and remove the other closer ones.

In most of the multiphase flows the secondary phase consists normally of moving bubbles, particles and droplets. Since the FPM is a fully Lagrangian method, it is a natural choice for the dispersed phase. Moreover, FPM is also an appropriate numerical method for simulation of, for example, free surface flows as well as flows with complicated and rapidly changing geometry since the classical methods like finite difference, finite element and finite volume methods are quite complicated and time consuming due to reconstruction of mesh in each time step. A first approach for Lagrangian mesh free method for solving fluid dynamic equations is the method of Smoothed Particle Hydrodynamics (SPH) [11, 12]. SPH was the originally invented to solve problems in astrophysics without geometry. This method has been further extended

to solve varieties of problems like compressible flows, incompressible flows, multiphase flows and others, see papers [13, 14] and references therein. The main difficulty of SPH is the incorporation of boundary conditions and higher order spatial derivatives.

Another widely used approach for solving fluid dynamics equations in a mesh-free framework is the moving least squares (MLS) or weighted least squares method [15, 16, 17, 18]. With this approach boundary conditions can be implemented in a natural way just by placing particles on boundaries and prescribing boundary conditions on them [17].

FPM has already been used in the two-fluid model in a liquid-liquid extraction column [8]. Furthermore, the mono-variate population balance equation (MPBE) has been incorporated in the two-fluid model [19, 21], where the MPBE is solved by the Sectional Quadrature Method of Moments (SQMOM) [22]. The details of SQMOM is presented in chapter [3].

In this work we have incorporated the mono-variate and the bivariate population balance equation (BPBE) in the multi fluid model in one-dimensional case, where the PBE is solved by the One Primary and One Secondary Particle Method (OPOSPM) [24] and Multi Primary One Secondary Particle Method (MPOSPM) [24]. Both of these methods are particular cases of Sectional Quadrature Method of Moments (SQMOM) [22]. This method is found to track accurately any set of low-order moments with the ability to reconstruct the shape of the distribution, so it unites the advantages of the Method of Classes (MC)[54] and the Quadrature Method of Moments (QMOM) [32], while it eliminates the drawbacks. The SQMOM is based on the concept of primary and secondary particles, whereas the primary particles are responsible for the reconstruction of the distribution (MC), while the secondary ones are responsible for breakage and coalescence events and carry information about the distribution (QMOM). As a first attempt in the coupling procedure, the normal limitation that only one set of Navier-Stokes equations is solved for all droplets [33] have been retained unchanged.

Some parts of this thesis have been presented in international conferences and published in proceedings; see [20, 21, 24, 25, 26, 27, 28, 29, 30].

1.2 Outline of Contents

We start in Chapter [2] with a brief overview of multiphase flow model equations and numerical approach to solve them. In particular, we focus in section 2.1 on the mathematical model and the existing schemes for solving the Population Balance Equation (PBE). One Primary and One Secondary Particle Method (OPOSPM) and Multi Primary and One Secondary Particle Method (MPOSPM) are addressed. At this point it is shown how the mathematical model can be reduced to a simple form. Next we present the Finite Pointset Method (FPM) and least square approximation to evaluate the spatial derivatives of a function. Furthermore, the idea of applying the FPM to the model equations is also discussed.

In Chapter [3], the formulation of population balance equation is discussed. We are primarily concerned with the analytical method to solve PBE and then the overview of numerical methods to solve PBE are discussed followed by the numerical results. The numerical results of PBE are validated with analytical solution of PBE in some particular cases. The comparison of numerical methods are discussed on the basis of accuracy, efficiency and complexity.

Chapter [4] presents the numerical results of CFD-PBM model. Mono-variate PBE is considered and the hydrodynamics of the model is provided. FPM-OPOSPM and FPM-MPOSPM solvers are discussed. In first section the results are provided for FPM-OPOSPM solver in the case of different breakage and coalescence kernels then the results are validated with the experimental data for pilot plants column and for the Kuehni column. In second section, the results of FPM-MPOSPM solver is shown. In the case of constant and non-constant breakage and coalescence kernels the results for both solvers are compared. Finally a three-fluid model is discussed and shown the better accuracy in the case of more turbulence.

We then proceed to consider the bivariate PBE or mass transfer into account in Chapter [5]. The effect of mass transfer coefficient on the solute concentration of both phases is shown followed by the significance of breakage and coalescence kernels. The results is compared with the experimental data in the case of RDC (DN-150) and Kuehni column (DN-150).

Chapter 2

Multiphase Flow Model and Numerical Approach

2.1 CFD-PBM Coupled Model

In this section, the governing equations are discussed. First, the general overview of the model is presented and then the brief description of spatially distributed population balance equation is given followed by the derivation of reduced model in the case of hydrodynamics and mass transfer between both phases in one-dimensional space.

2.1.1 General overview of a model

We consider the two-fluid model for multiphase flows, where both phases are liquids. We call them primary phase (aqueous continuous phase) and secondary phase (organic dispersed phase). All the quantities with the index c denotes the continuous phase and the index d is for the dispersed phase. All equations are written in Lagrangian form. The continuity equations for the continuous and dispersed phases are

$$\frac{d\alpha_c}{dt} = -\alpha_c(\nabla \cdot u_c) \quad (2.1)$$

$$\frac{d\alpha_d}{dt} = -\alpha_d(\nabla \cdot u_d), \quad (2.2)$$

where α_c and α_d are the volume fractions, u_c and u_d are the velocity vectors and $\frac{d}{dt}$ is the material derivative.

8CHAPTER 2. MULTIPHASE FLOW MODEL AND NUMERICAL APPROACH

In addition to Equations (2.1) and (2.2) the volume fractions must satisfy the following constraint

$$\alpha_c + \alpha_d = 1. \quad (2.3)$$

The conservation of momentum for the continuous phase is given by

$$\frac{du_c}{dt} = -\frac{\nabla p}{\rho_c} + \frac{1}{\alpha_c \rho_c} \nabla \cdot \tau_c + g + \frac{1}{\alpha_c \rho_c} F_{drag} \quad (2.4)$$

and for the secondary phase is given by

$$\frac{du_d}{dt} = -\frac{\nabla p}{\rho_d} + \frac{1}{\alpha_d \rho_d} \nabla \cdot \tau_d + \left(1 - \frac{\rho_c}{\rho_d}\right)g + \frac{1}{\alpha_d \rho_d} F_{drag}, \quad (2.5)$$

where ρ_c and ρ_d are the densities, p is the pressure shared by both phases, g is the gravitational force and F_{drag} represents the interfacial forces and τ is the stress tensor, for example, for the continuous phase it is given by

$$\tau_c = \alpha_c \mu_c [\nabla u_c + (\nabla u_c)^T - \frac{1}{3}(\nabla \cdot u_c)I], \quad (2.6)$$

where μ_c is the dynamic viscosity of the continuous phase. The inter-phase interaction term consists of different momentum exchange mechanisms. Only the drag force was taken into account, while the virtual mass force and the lift force can be neglected for a liquid-liquid interaction as shown by Wang and Mao [34] in a stirred tank. The interfacial momentum transfer (drag force) between two phases is given by

$$F_{drag} = \frac{3}{4} \alpha_d \rho_c \frac{C_D}{d_{30}} |u_d - u_c| (u_d - u_c) \quad (2.7)$$

where d_{30} is the diameter of the droplets of the dispersed liquid phase and the drag force coefficient C_D is given by ([44])

$$C_D = \begin{cases} \frac{24}{Re} (1 + 0.15 Re^{0.687}) & \text{if } Re \leq 1000 \\ 0.44 & \text{if } Re > 1000 \end{cases}$$

and Re is the relative Reynolds number defined as

$$Re = \frac{\rho_c |u_d - u_c| d_{30}}{\mu_c} \quad (2.8)$$

If the breakage and aggregation between droplets are not taking place, like in the mono-dispersed phase, the diameter of the droplet d_{30} is considered to be constant. In general, this is not a constant and droplets are assumed to have

a spectrum of sizes. This spectrum can be computed with the help of Population Balance Equation (PBE). One can construct the wide range of classes of droplets based on their sizes, however, the considerations of individual class may not be feasible in the computer simulations since momentum equations have to be solved for each class. Currently CFD-PBM models are based on the two-fluid Multiple Size Group (MUSIG) Model [33], where all droplets in the PBM share the same velocity field and only one momentum equation is solved for all droplet classes based on the area averaged droplet size, also called mean diameter and denoted by d_{30} . This quantity can be computed with the help of the solution of the population balance equation, described in the following subsections. A new strategy, the inhomogeneous MUSIG tries to divide the dispersed phase into a number N so-called velocity groups, where each of the velocity groups is characterized by its own velocity field, to get rid of the common simplification [35]. A drawback of this multi-fluid approach is that it is based on the CPU-time consuming classes method. In this connection, the MPOSPM seems to be another interesting alternative, since each primary particle could move with its own velocity group and hence having its own momentum equation resulting also in a multi-fluid model depending on the number of primary particles. As a benefit, in comparison to the inhomogeneous MUSIG model, MPOSPM is less CPU-time consuming, since it is based on the computational less expensive quadrature method of moments. PBE is an integro-partial differential equation (described in details in the next chapter). PBE is not possible to solve analytically as it has some complicated integro-partial terms. So we require numerical method to solve PBE. In literature, several numerical methods are available to solve PBE. We have chosen the method called OPOSPM (One Primary and One Secondary Particle Method) and MPOSPM (Multi Primary and One Secondary Particle Method).

2.1.2 Spatially Distributed Population Balance Equation

The general Spatially Distributed Population Balance Equation (SDPBE) [36] for describing the coupled hydrodynamics and mass transfer in Liquid-Liquid Extraction Columns (LLECs) can be written as

$$\frac{\partial n_{d,ca}(\psi)}{\partial t} + \nabla \cdot (u_d n_{d,ca}(\psi)) + \sum_{i=1}^2 \frac{\partial [\zeta_i n_{d,ca}(\Psi)]}{\partial \zeta_i} = \nabla \cdot [D_d \nabla n_{d,ca}(\psi)] + \mathcal{R}\{\psi\}. \quad (2.9)$$

In this equation the components of the vector $\psi = [d \ c_d \ x \ t]$ are those for the droplet internal coordinates (diameter and solute concentration), the external coordinate x and the time t , where the velocity vector along the internal coordinates is given by $\dot{\zeta} = [\dot{d} \ \dot{c}_d]$. The source term $\mathcal{Y}\{\psi\}$ represents the net number of droplets produced by breakage and coalescence per unit volume and unit time in the coordinates range $\zeta \pm \partial\zeta$. The left hand side is the continuity operator in both the external and internal coordinates, while the first part of the right hand side is the droplet axial dispersion characterized by the dispersion coefficient, D_d , which might be dependent on the energy dissipation and the droplet rising velocity [68]. The second term $\mathcal{Y}\{\psi\}$ of right hand side is the source term which could be expanded as :

$$\mathcal{Y} = B^b(d, c_d; t, x) - D^b(d, c_d; t, x) + B^c(d, c_d; t, x) - D^c(d, c_d; t, x),$$

where B^b and B^c are the rate of droplets birth due to droplet breakage and coalescence respectively, and D^b and D^c are the rates of droplet loss (death) due to droplet breakage and coalescence respectively and are expressed as follows :

$$B^b = \int_d^{d_{max}} \int_0^{c_{d,max}} \Gamma(d', \alpha_d) \beta(d|d') n_{d,c_d}(d', c'_d; t, x) \delta(c'_d - c_d) \partial d \partial c'_d \quad (2.10)$$

$$D^b = -\Gamma(d, \alpha_d) n_{d,c_d}(d', c'_d; t, x) \quad (2.11)$$

$$B^c = \frac{1}{2} \int_0^d \int_{c'_{d,min}}^{c'_{d,max}} \omega(d', \eta, \alpha_d) \left(\frac{d}{\eta}\right)^5 n_{d,c_d}(d', c'_d; t, x) n_{d,c_d}(d', c''_d; t, x) \partial d' \partial c'_d,$$

$$\eta = (d^3 - d'^3)^{(1/3)}, \quad c''_d = \frac{c_d v(d) - c'_d v(d')}{v(d) - v(d')}, \quad (2.12)$$

$$\begin{aligned} c'_{d,max} &= \min(c_{d,max}, (v(d)/v(d'))c_d), \\ c'_{d,min} &= \max(0, c_{d,max}(1 - v(d)/v(d')(1 - c_d/c_{d,max}))) \end{aligned} \quad (2.13)$$

$$D^c = n_{d,c_d}(d', c'_d; t, x) \int_0^{(d_{max}^3 - d^3)^{(1/3)}} \int_0^{c_{d,max} \omega(d, d'; \alpha_d)} n_{d,c_d}(d', c'_d; t, x) \partial d' \partial c'_d \quad (2.14)$$

If we consider only one internal coordinate (size of droplets) then we can write reduced SDPBE in the following form :

$$\frac{\partial f(V, x, t)}{\partial t} + \nabla \cdot (u_d f(V, x, t)) = S(f(V, x, t), V, x, t), \quad (2.15)$$

where

$$\begin{aligned}
S = & -\Gamma(V)f(V, x, t) + \int_V^{V_{max}} \Gamma(V', x, t)\beta(V|V')f(V', x, t) \\
& - f(V, x, t) \int_{V_{min}}^{V_{max}} \omega(V, V')f(V', x, t)dV' \\
& + \frac{1}{2} \int_{V_{min}}^V \omega(V - V', V')f(V - V', x, t)f(V', x, t)dV',
\end{aligned} \tag{2.16}$$

$f(V, x, t)$ is the number density function with particle size V as an independent variable. The vector u_d is the same particle velocity introduced in previous section. The source term S consists of loss term (preceded by minus sign) and gain term (preceded by plus sign) due to breakage and aggregation collisions of droplets. The breakage and aggregation of the droplets are governed by breakage and aggregation frequency, respectively. The breakage frequency $\Gamma(V)$ represents the fraction of droplets breaking per unit time, while the aggregation frequency $\omega(V, V')$ accounts for the probability of successful collisions between a pair of droplets. The splitting of mother droplet of size V' to daughter droplets having a spectrum of sizes is given by the daughter particle distribution $\beta(V|V')$.

2.1.3 Fluid Dynamics Equations

The solute concentration in the continuous phase (C_c) is predicted using a component solute balance on the continuous phase :

$$\begin{aligned}
\frac{\partial(\alpha_c C_c)}{\partial t} - \frac{\partial}{\partial z}(u_c \alpha_c C_c + D_c \frac{\partial(\alpha_c C_c)}{\partial z}) = & \frac{Q_c^{in} C_c^{in}}{A_c} \delta(z - z_c) \\
& - \int_0^\infty \int_0^{C_{d,max}} \dot{C}_d v(d) f_{d,C_d}(\Psi) \partial d \partial C_d,
\end{aligned} \tag{2.17}$$

here α_c is the volume fraction and u_c is the velocity. Note that the volume fraction for the continuous phase (α_c) satisfies the physical constraint:

$$\alpha_c + \alpha_d = 1, \tag{2.18}$$

where $v(d)$ is the droplet volume. The left hand side of Equation (2.17) is the continuity operator and the first term on the right hand side is a point source term representing the rate at which the continuous phase entering the column with volumetric flow rate (Q_c^{in}) that is the perpendicular to the column cross-sectional area (A_c) at a location (z_c). The last term appearing in Equation (2.17) is the total rate of solute transferred from the continuous to the dispersed phase, where the liquid droplets are treated as moving point sources. The presence of the diffusion flux in the second term of Equation (2.17) is to take into account the non ideal behavior of the turbulent continuous flow [38].

In this thesis, the simplified mass transfer model of Handlos and Baron [39] as well as the correlation of Kumar and Hartland [40] are used. However, the criterion based on the Reynolds number as suggested by Zhang [41] may be used as a guide for selecting the proper mass transfer model. The individual mass transfer coefficient for the continuous phase is essentially subjected to the aforementioned classification procedure, where two models are used to predict it. The first simple one is based on the film coefficient equation as recommended by Weinstein [42] and Wang [43], and the second one is based on the correlation of Kumar and Hartland [40] for RDC liquid-liquid extraction columns.

Now, once the individual mass transfer coefficients are estimated, the rate of change of solute concentration in the liquid droplet (\dot{C}_d) is expressed in terms of the droplet volume average concentration and the overall mass transfer coefficient (K_{od}) :

$$\dot{C}_d = \frac{6K_{od}}{d}(C_d^*(C_c) - C_d(z, t)). \quad (2.19)$$

Note that (K_{od}) may be function of the droplet diameter and time depending on the initial state of the droplet; that is, weather it is circulating or behaving like a rigid sphere. The overall mass transfer coefficient is usually expressed using the two-resistance theory in terms of the individual mass transfer coefficients for the continuous and the dispersed phases [38] and $C_d^* = mC_c$, where C_d^* is the maximum attainable thermodynamic equilibrium solute concentration and m is the distribution coefficient.

In this work we consider all model equations in the Lagrangian form. To get the velocity of the dispersed phase (u_d), we solve the momentum balance equation as we have discussed in subsection 2.1.1. The momentum balance

equation in one dimensional space can be written as

$$\frac{du_d}{dt} = -\frac{\partial P}{\partial z} + \left(1 - \frac{\rho_c}{\rho_d}\right)g - \frac{1}{\alpha_d \rho_d} F_{drag}, \quad (2.20)$$

where $\frac{d}{dt}$ is the material derivative and F_{drag} represents the interfacial force which is given in Equation (2.7), ρ_c and ρ_d are the densities, g is the gravitational force, μ_c is the dynamic viscosity and P is the pressure which is assumed the same for both phases and defined as

$$P = \rho_c g z. \quad (2.21)$$

2.1.4 Reduced Model with OOSPM

The one primary and one secondary particle method is the simplest discrete method that can reduce the continuous population balance equation. This representation is of moderate accuracy and reflects all the features contained in the continuous population balance equation. For example, the method conserves both total number and volume (mass) concentrations and is exact when the breakage and coalescence frequencies are constants. This corresponds to tracking directly the total number concentration N , volume fraction α_d and the solute concentration \overline{C}_d by solving their transport equations. To derive these equations, the bivariate density function is considered as Dirac delta function with weight N and locations d_{30} and \overline{C}_d :

$$n_{d,C_d}(d, C_d; t, z) = N(t, z) \delta(d - d_{30}(t, z)) \delta(C - \overline{C}_d(t, z)). \quad (2.22)$$

This is equivalent to replacing the bivariate density function by one primary and one secondary particle (in the special case they are identical) with weight N and internal states d_{30} (mean diameter) and \overline{C}_d (mean solute concentration). The total number, volume and mean solute concentrations are defined by :

$$N = \int_0^\infty \int_0^{C_d^*} n_{d,C_d} \partial d \partial C_d, \quad (2.23)$$

$$\alpha_d = \int_0^\infty \int_0^{C_d^*} v n_{d,C_d} \partial d \partial C_d, \quad (2.24)$$

and

$$\overline{C_d} = \frac{\int_0^\infty \int_0^{C_d^*} C_d v n_{d,C_d} \partial d \partial C_d}{\int_0^\infty \int_0^{C_d^*} v n_{d,C_d} \partial d \partial C_d}. \quad (2.25)$$

To get the transport equation for the total number concentration N , Equation (2.22) is substituted in Equation (2.9) and both sides are integrated with respect to d and C_d from 0 to ∞ and from 0 to C_d^* respectively. By doing this, the following transport equation is arrived at :

$$\frac{dN}{dt} + N \frac{\partial u_d}{\partial z} = (\nu(d_{30}) - 1) \Gamma(d_{30}, \overline{C_d}) N - \frac{1}{2} \omega(d_{30}, d_{30}, \overline{C_d}) N^2. \quad (2.26)$$

Note that the first term of Equation (2.26) is the rate of formation of particles with breakage frequency Γ . The mean number of daughter particles is given by ν that is determined by integrating the daughter droplet distribution function with respect to d_{30} . This distribution is determined using single droplet experiment in small devices [45]. The second term in Equation (2.26) is the net rate of droplet death due to coalescence of two droplets of the same mean size and concentration with frequency ω . It is clear that droplet breakage and coalescence follow first and second order mechanism based on N respectively.

The transport equations for α_d and $\overline{C_d}$ in Lagrangian form for one-dimensional case are derived by multiplying Equation (2.9) by $v(d_{30})$ for α_d and $C_d v(d_{30})$ for $\overline{C_d}$, substituting Equation (2.22) in Equation (2.9) and integrating from 0 to ∞ and 0 to C_d^* with respect to d and C_d respectively to get :

$$\frac{d\alpha_d}{dt} + \alpha_d \frac{\partial u_d}{\partial z} = 0 \quad (2.27)$$

and

$$\frac{dD}{dt} + D \frac{\partial u_d}{\partial z} - \frac{\partial}{\partial z} (D_d \frac{\partial D}{\partial z}) = \frac{6K_{od}(d_{30}, \overline{C_d})}{d_{30}} (m'C - D). \quad (2.28)$$

The solute balance in the continuous phase is found directly by substituting (2.22) in the integral of the right hand side of (2.17) :

$$\frac{dC}{dt} + C \frac{\partial u_c}{\partial z} - \frac{\partial}{\partial z} (D_c \frac{\partial C}{\partial z}) = -\frac{6K_{od}(d_{30}, \overline{C_d})}{d_{30}} (m'C - D), \quad (2.29)$$

where, $m' = \frac{\alpha_d}{\alpha_c}m$, $D = \alpha_d C_d$ and $C = \alpha_c C_c$. The Equation (2.29) is written in Lagrangian form for one-dimensional case.

The mean particle diameter d_{30} can be found from the mean mass of the secondary particle :

$$d_{30} = \begin{cases} \sqrt[3]{\frac{6}{\pi} \frac{\alpha_d}{N}} & \text{if } N > \sqrt{\epsilon} \\ d_{vs} & \text{otherwise,} \end{cases}$$

where, ϵ is a small number and d_{vs} is the feed mean droplet diameter. This is only required to avoid division by zero in the regions where there is no particle concentration. It is actually the mean diameter of secondary particle whose mass is given as the ratio between its volume and number concentrations.

To close the model, an expression for the continuous phase velocity u_c is derived by adding the continuity equations for the dispersed and the continuous phases assuming that the density of both phases is constant (See Appendix A). This assumption is justified when low mass transfer fluxes are encountered and the two liquids are considered to be incompressible. The resulting expression [5] is defined as :

$$u_c = \frac{Q_c^{in}}{A_c \alpha_c} \Delta_c + \frac{D_c}{\alpha_c} \frac{\partial \alpha_d}{\partial z}, \quad (2.30)$$

where,

$$\Delta_c = \begin{cases} 1 & \text{if } z \leq z_c \\ 0 & \text{otherwise} \end{cases} .$$

The discontinuity appearing in the continuous phase velocity u_c is due to the presence of the step function Δ_c .

2.1.5 Model with MPOSPM

To solve PBE if we use SQMOM by choosing one secondary particle then it becomes MPOSPM (Multi Primary and One Secondary Particle Method). Note that the primary and secondary particles coincide with each other in this case. So, the population density in each section is represented by a single particle whose position (size) is set according to the variation of the population density in this section and is given by :

$$d_{30,i} = \sqrt[3]{\frac{\pi}{6} \frac{\alpha_{d_i}}{N_i}}, \quad (2.31)$$

where N_i and α_{d_i} are the total number and volume concentrations of the population of real particles (assumed to have spherical shape) in the i th section. By assuming two distinct integral properties ($N_i, \alpha_{d_i}, i = 1, 2, \dots, N_{pp}$) to each particle, the secondary particles are exactly equivalent to a one-point Gauss-like quadrature according to the QMOM framework [32]. Mathematically this is equivalent to approximating the number density function $f(d, t)$ in each section by a Dirac delta function having weight N_i and centred at $d_{30,i}$:

$$f^{<i>}(d, t) = N_i \delta(d - d_{30,i}) \quad (2.32)$$

The transport equations for the integral quantities : N_i and α_{d_i} are obtained from Equation (2.15) and Equation (2.32) by first multiplying Equation (2.15) by $(v^r, r = 0, 1)$ followed by the integration with respect to (v) from 0 to ∞ to get

$$\frac{dN_i}{dt} + N_i(\nabla \cdot u_d) = \pi_{0,i} \quad (2.33)$$

$$\frac{d\alpha_{d,i}}{dt} + \alpha_{d,i}(\nabla \cdot u_d) = \pi_{3,i} \quad (2.34)$$

Where the source terms ($\pi_{0,i}$ and $\pi_{3,i}$) represent the net number and volume concentration due to breakage and coalescence events associated with i th primary particle are given in next chapter [3].

2.2 Hyperbolicity Analysis of the CFD-PBM Coupled Model

In this section, a study of the characteristics (hyperbolicity) of the model equations is discussed.

2.2.1 Formulations

In Eulerian frame of reference, the model after applying OPOSPM in the case of a one-dimensional incompressible liquid-liquid two-phase flow, in terms of conservative variables, can be written in vector form as

$$\frac{\partial U}{\partial t} + \frac{\partial F(U)}{\partial z} = S(U), \quad z \in R, \quad t \in R^+ \quad (2.35)$$

2.2. HYPERBOLICITY ANALYSIS OF THE CFD-PBM COUPLED MODEL 17

where

$$U = \begin{pmatrix} N \\ \alpha_d \\ \alpha_d u_d \\ \alpha_d C_d \\ \alpha_c C_c \end{pmatrix}, \quad F(U) = \begin{pmatrix} Nu_d \\ \alpha_d u_d \\ \alpha_d u_d^2 \\ \alpha_d C_d u_d \\ -\alpha_c C_c u_c \end{pmatrix}$$

and $S(U)$ is given in Equations (2.20,2.26,2.27,2.28) and (2.29). In Equation (2.35) U and F represent the vector of conservative variables and the flux vector respectively.

To determine the classification of the model equations we choose a standard formulation and analysis applicable to systems of first-order quasi-linear partial differential equations. The analysis requires that Equation (2.35) be written in the following quasi-linear form

$$\frac{\partial U}{\partial t} + A(U) \frac{\partial U}{\partial z} = S(U), \quad (2.36)$$

which is obtained by carrying out the differentiation of F with respect to z . The matrix $A(U)$ is the Jacobian matrix defined by

$$A(U) = \frac{\partial F}{\partial U}. \quad (2.37)$$

Now if we denote the components of U and F by u_i and f_i ($i=1, \dots, 5$), respectively, then $A(U)$ can be expressed as

$$A(U) = \begin{pmatrix} \frac{\partial f_1}{\partial u_1} & \frac{\partial f_1}{\partial u_2} & \cdots & \frac{\partial f_1}{\partial u_5} \\ \frac{\partial f_2}{\partial u_1} & \frac{\partial f_2}{\partial u_2} & \cdots & \frac{\partial f_2}{\partial u_5} \\ \vdots & \vdots & \vdots & \vdots \\ \frac{\partial f_5}{\partial u_1} & \frac{\partial f_5}{\partial u_2} & \cdots & \frac{\partial f_5}{\partial u_5} \end{pmatrix}.$$

By direct evaluation of all partial derivatives, the following expression is obtained for $A(U)$

$$A(U) = \begin{pmatrix} u_d & -\frac{Nu_d}{\alpha_d} & \frac{N}{\alpha_d} & 0 & 0 \\ 0 & 0 & 1 & 0 & 0 \\ 0 & -u_d^2 & 2u_d & 0 & 0 \\ c_d & -c_d u_d & c_d & u_d & 0 \\ 0 & 0 & 0 & 0 & -u_c \end{pmatrix}.$$

This matrix contains the number density, the volume concentration of dispersed phase, the velocities of both phases and the solute concentration of the dispersed phase.

The mathematical analysis of the model can be carried out using variables other than the conserved variables. Alternative choice of formulation then is the vector of primitive variables [46]. The primitive variables for a one-dimensional CFD-PBM coupled model would be

$$W = \begin{pmatrix} N \\ \alpha_d \\ u_d \\ C_d \\ C_c \end{pmatrix} \quad (2.38)$$

for which the governing equations take the form

$$B(W) \frac{\partial W}{\partial t} + A(W) \frac{\partial W}{\partial z} = Q(W), \quad (2.39)$$

where $Q(W) = \frac{\partial W}{\partial U} S(U)$ and the coefficient matrices are arranged as follows

$$B(W) = \begin{pmatrix} 1 & 0 & 0 & 0 & 0 \\ 0 & 1 & 0 & 0 & 0 \\ 0 & u_d & \alpha_d & 0 & 0 \\ 0 & C_d & 0 & \alpha_d & 0 \\ 0 & 0 & 0 & 0 & \alpha_c \end{pmatrix},$$

$$A(W) = \begin{pmatrix} u_c & 0 & N & 0 & 0 \\ 0 & u_d & \alpha_d & 0 & 0 \\ 0 & u_d^2 & 2\alpha_d & 0 & 0 \\ 0 & u_d C_d & \alpha_d C_d & \alpha_d u_d & 0 \\ 0 & 0 & 0 & 0 & -\alpha_c u_c \end{pmatrix}.$$

2.2.2 Mathematical Property of the Model Equations

The one-dimensional Equation (2.35) represent an initial value problem with initial conditions $U(z, 0) = U_0(z)$ in the range of $a \leq z \leq b$ and $t \geq 0$. This initial-value problem is well posed if system (2.35) has a unique solution on the differentiable interval value $U_0(z)$. In other words, if the coefficient matrix of the system has real eigenvalues, then the initial-value problem is said to be a well-posed problem. If all the corresponding eigenvalues are linearly independent then the system is hyperbolic. More precisely, it is well known that the eigenvalues do not depend on the source terms and they represent the wave propagating speeds characterized by fluid properties and their dynamic interactions. For the characteristics analysis therefore, one would

2.2. HYPERBOLICITY ANALYSIS OF THE CFD-PBM COUPLED MODEL 19

work with the homogeneous form of both formulations, conservative (2.36) and primitive (2.39). Thus, we set $S(U) \equiv 0$ or $Q(W) = 0$ to investigate the mathematical properties of the eigenvalues and eigenvectors. For both formulations, conservative and primitive, the eigenvalues associated with the CFD-PBM coupled model are determined by

$$\det[A - \lambda I] = 0. \quad (2.40)$$

As a result we derive a fifth-order polynomial equation as

$$P_5(\lambda) = (u_d - \lambda)^4(u_c + \lambda) = 0, \quad (2.41)$$

which gives the following real eigenvalues

$$\lambda_d = u_d \quad \lambda_c = -u_c. \quad (2.42)$$

Clearly, the first eigenvalue, a multiple eigenvalue, represent the dispersed phase velocity while the second eigenvalue is related to the continuous phase along the column. The two physical velocities appearing here might not be in agreement with all current proposals on this subject and have no analogy in one-phase fluid dynamics. However, our present theoretical knowledge in this area is still insufficiently mature that a definitive judgement is not yet possible.

The existence of only real eigenvalues is a necessary but not a sufficient condition for the existence of a well-posed hyperbolic system of partial differential equations. A further requirement is the existence of a complete set of independent eigenvectors. On the other hand, this is a prerequisite for the proper applications of a number of advanced numerical techniques which make explicit use of the hyperbolic nature of the governing field equations. The eigenvectors of matrix A , $K^{(j)}$ ($j = 1, \dots, 5$), are solutions of the eigenvalue problem

$$AK^{(j)} = \lambda_j K^{(j)} \quad (2.43)$$

If we choose to present the corresponding right eigenvectors for the conserved formulation (2.36). Then, the eigenvectors are

$$K^{(d)} = \begin{pmatrix} 0 \\ 1 \\ u_d \\ 0 \\ 0 \end{pmatrix}, \quad K^{(c)} = \begin{pmatrix} \frac{N}{\alpha_d} \\ 1 \\ -u_c \\ 0 \\ 0 \end{pmatrix},$$

where the first four eigenvectors correspond to the dispersed phase and fifth eigenvector correspond to the continuous phase.

We end this section with the nature of the characteristics fields associated with each pair $(\lambda_j, K^{(j)})$. The characteristic field associated with the continuous phase $(\lambda_c = -u_c)$ is found to be linearly degenerate

$$\nabla \lambda_c(U) \cdot K^{(c)}(U) = 0 \quad \forall U, \quad (2.44)$$

which is also the case for the dispersed phase $(\lambda_d = u_d)$ since

$$\nabla \lambda_d(U) \cdot K^{(d)}(U) = 0 \quad \forall U. \quad (2.45)$$

The established eigenstructure shows that the CFD-PBM coupled model is hyperbolic with eigenvectors being linearly degenerate. They correspond to contact discontinuities [47], [48]. In applications, it is fairly typical that the linearly degenerate eigenvectors correspond to a multiple eigenvalues. An important observation is that only contact discontinuities are present in the solution of the model equations.

2.3 Finite Pointset Method (FPM)

The basis of the computations in FPM is point cloud, which represents the flow field. The points of the cloud are referred to as particles or numerical grids. They are carriers of all relevant physical information. The particles have to completely cover the whole flow domain, i.e. the point cloud has to fulfil certain quality criteria (particles are not allowed to form holes which means particles have to find sufficiently many neighbors; also, particles are not allowed to cluster; etc.). The point cloud is a geometrical basis, which allows for a numerical formulation making FPM a general finite difference idea applied to continuum mechanics. That especially means, if the point cloud would receive to a classical finite difference method. The idea of general finite difference also means that FPM is not based on a weak formulation like the Galerkin's approach. Rather, FPM is a strong formulation which models differential equations by direct approximation of the occurring differential operators. The method used is a moving least square idea which was specially developed for FPM.

2.3.1 Least Square Approximation

Since the fluid information have to be communicated from one point to another and vice versa, we must interpolate these quantities accurately. Therefore, it is necessary to use the second order approximation. In this section,

we present the least square approximation of a function at an arbitrary position from the surrounding cluster of points.

Consider the computational domain $\Omega \subset R^n, n = 1, 2, 3$. Consider a set of clouds, grids or particles $P(x, h) = \{x_i : x_i \in \Omega, i = 1, \dots, N\}$. The distribution of particles does not necessarily have to be uniform and can be quite arbitrary. A typical distribution of particles, for example in 2D, looks like in Fig. 1.

Let $f(x)$ be a scalar function and f_i its values at x_i for $i = 1, 2, \dots, N$.

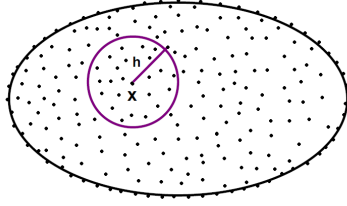


Figure 2.1: Flow domain with non-structured grid

Consider the problem to approximate $f(x)$ and its spatial derivatives at x in terms of the values of a set of neighbouring points. In order to limit the number of points we associate a weight function $w = w(x_i - x; h)$ with a small compact support, where h determines the size of the support, as shown in Fig. 1. In SPH, h is known as a smoothing length. The smoothing length defines a set of neighbouring particles around x . The weight function can be quite arbitrary but in our computations, we consider a Gaussian weight function in the following form

$$w(x_i - x; h) = \begin{cases} \exp(-C \frac{\|x_i - x\|^2}{h^2}), & \text{if } \frac{\|x_i - x\|}{h} \leq 1 \\ 0, & \text{otherwise} \end{cases}$$

with C a positive constant is considered to be in the range of 2 to 6 and depends upon the users.

For consistency reasons some obvious restrictions are required, namely for example, in $2D$, if we want the second order approximation there should be at least 6 neighbour particles including the central particle and they should neither be on the same line nor on the same circle. Hence we define the size of h such that the minimum number of neighbours is guaranteed for the approximation of derivatives. Hence, new particles will have to be introduced into the simulations as the particle distribution becomes too sparse or, particles will have to be removed from the computation as they become too dense.

Let $N(x, h) = \{x_i : i = 1, 2, \dots, m\}$ be the set of m neighbouring points of x . We approximate the function $f(x)$ by $f_h(x)$ as $f_h(x) = \sum_{i=1}^N f_i \phi(x_i, x)$, where the shape function $\phi(x_i, x)$ is computed at each point x by the least square method over its own compact support. We note that $\phi_i = 0$ for all $i \notin N(x, h)$. It is important to stress that this expression is consistent only if the function ϕ is 1 at x_i , namely $\phi(x_i, x_j) = \delta_{ij}$ for all $i, j = 1, 2, \dots, N$.

The approximation of the first and second order derivatives can be computed directly from $f_h(x)$ or directly by using the least square method. The first method is known in literature as moving least square method [16], [17]. Usually the function $f_h(x)$ and its derivatives $f_{kh}(x)$ are not smooth enough to be differentiable and therefore the second order derivatives can not be properly computed. We approximate the derivatives $\partial f(x)/\partial x_k$ by $f_{kh}(x) = \sum_{i=1}^N f_i \eta_k(x_i, x)$ for $k = 1, 2, 3$, where $\eta_k(x_i, x)$ is directly computed by the least squares interpolation. In a similar manner we define the approximation for the second order derivatives $\partial^2 f(x)/\partial x_l \partial x_k$ by $f_{klh}(x) = \sum_{i=1}^N f_i \Psi_{kl}(x_i, x)$ for $k, l = 1, 2, 3$. The determination of the function $f(x)$, $f_{kh}(x)$ and $f_{klh}(x)$ for $k, l = 1, 2, 3$ can be computed easily and accurately by using the Taylor series expansion and the least square approximation. We write a Taylor's expansion around the point x with unknown coefficients by minimizing a weighted error over the neighbouring points. The optimization is constrained to satisfy $\phi(x_1, x_1) = 1$ where x_1 is the closest point, namely the approximation must interpolate the closest point.

In order to approximate the function and its derivatives at x by using a quadratic approximation through the m neighboring points sorted with respect to its distance from x we let

$$\begin{aligned} f(x_i) &= f_h(x) + \sum_{k=1}^3 f_{kh}(x)(x_{ki} - x_k) \\ &+ \frac{1}{2} \sum_{k,l=1}^3 f_{klh}(x)(x_{ki} - x_k)(x_{li} - x_k) + e_i, \end{aligned} \quad (2.46)$$

where e_i is the error in the Taylor's expansion at the point x_i . The unknowns f_h, f_{kh} and f_{klh} for $k, l = 1, 2, 3$ are computed by minimizing the error e_i for $i = 2, 3, \dots, m$ and setting the constraint $e_1 = 0$. By subtracting the first equation with $e_1 = 0$ to all the other equations the system can be written as $e = Ma - b$, where M is the $m \times 9$ geometrical matrix, in $3D$, whose components consist of the directional distances from the

m -neighbours to the central particle x . The other vectors are denoted by $a = [f_{1h}, f_{2h}, f_{3h}, f_{11h}, f_{12h}, f_{13h}, f_{22h}, f_{23h}, f_{33h}]^T$, $b = [f_2 - f_1, f_3 - f_1, \dots, f_m - f_1]^T$, $e = [e_2, e_3, \dots, e_m]^T$. For $m > 9$, this system is over-determined for the nine unknowns f_{kh} and f_{klh} for $k, l = 1, 2, 3$.

The unknowns a are obtained from a weighted least squares method by minimizing the quadratic form

$$J = \sum_{i=1}^m w_i e_i^2. \quad (2.47)$$

The above equations can be expressed in the form

$$J = (Ma - b)^T W (Ma - b), \quad (2.48)$$

where $W = \delta_{ij} w_i$. The minimization of J formally yields

$$a = (M^T W M)^{-1} (M^T W) b. \quad (2.49)$$

Now from the equation for the closest point x_1 we can compute the value of $\Psi(x)$ at x as

$$f_h(x) = f(x_1) - \sum_{k=1}^3 f_{kh}(x)(x_{k1} - x_k) - \frac{1}{2} \sum_{k,l=1}^3 f_{lkh}(x)(x_{k1} - x_k)(x_{l1} - x_k) \quad (2.50)$$

since f_{kh} and f_{klh} for $k, l = 1, 2, 3$ are now known. The solution of the constrained least squares problem is straightforward and more sophisticated techniques can be used. For example minimization or singular decomposition techniques can be very helpful to determine efficiently the unknowns.

We note that if the approximation is computed at x_i we have $f_h(x_i) = f_i$ which implies $\phi(x_i, x_j) = \delta_{ij}$ can be approximated very closely performing the unconstrained least squares minimization over all the m equations.

2.4 Numerical Approach

We solve the model equations in one-dimensional frame by using Euler implicit method. The following steps are followed to compute the quantities.

(i) Compute the number concentration N^{n+1} implicitly by

$$N^{n+1} = \frac{N^n}{1 + \Delta t [\nabla \cdot u_d^n - (\nu - 1) \Gamma(d_{30}^n) + \frac{1}{2} \omega(d_{30}^n, d_{30}^n) N^n]} \quad (2.51)$$

(ii) Compute the volume fraction α_d^{n+1} implicitly as

$$\alpha_d^{n+1} = \frac{\alpha_d^n}{1 + \Delta t (\nabla \cdot u_d^n)} \quad (2.52)$$

and use the constraint (2.3) to compute volume fraction for continuous phase α_c^{n+1}

$$\alpha_c^{n+1} = 1 - \alpha_d^{n+1} \quad (2.53)$$

(iii) Compute the droplets velocity u_d^{n+1} as

$$u_d^{n+1} = \frac{u_d^n - \Delta t (\nabla P + (1 - \frac{\rho_c}{\rho_d})g) + \frac{3}{4} \frac{\alpha_d^n \rho_c}{\alpha_d^n \rho_d} \frac{C_{drag}}{d_{30}^n} |u_d^n - u_c^n|}{1 + \Delta t \frac{3}{4} \frac{\alpha_d^n \rho_c}{\alpha_d^n \rho_d} \frac{C_{drag}}{d_{30}^n} |u_d^n - u_c^n|} \quad (2.54)$$

(iv) Add the continuity equations of both phases to yield the velocity of continuous phase u_c^{n+1} :

$$u_c^{n+1} = \frac{1}{\alpha_c^n} \frac{Q_c^{in}}{A_{col}} \Delta z, \quad (2.55)$$

where Δz is a step function, defined as

$$\Delta z = \begin{cases} 1, & \text{if } z \leq z_c \\ 0, & \text{else} \end{cases}$$

for $z \in (z_d, z_c)$ with z_d and z_c are the inlets of the dispersed and continuous phase, respectively.

(v) Compute the solute concentration for dispersed phase implicitly as

$$D^{n+1} = \frac{D^n + \nabla (D_d \nabla D^n) \Delta t + \frac{6K_{od}^n}{d_{30}^n} m^n C^n \Delta t}{1 + \frac{6K_{od}^n}{d_{30}^n} \Delta t + \nabla \cdot u_d^n \Delta t}, \quad (2.56)$$

where $D^{n+1} = C_d^{n+1} \alpha_d^{n+1}$ and $m^n = \frac{\alpha_d^n}{\alpha_c^n}$.

(vi) Compute the solute concentration for continuous phase implicitly as

$$C^{n+1} = \frac{C^n + \nabla (D_c \nabla C^n) \Delta t + \frac{6K_{od}^n}{d_{30}^n} D^n \Delta t}{1 + \frac{6K_{od}^n}{d_{30}^n m^n} \Delta t + \nabla \cdot u_c^n \Delta t}, \quad (2.57)$$

where $C^{n+1} = C_c^{n+1} \alpha_c^{n+1}$.

(vii) Move particles

$$z^{n+1} = z^n + \Delta t u_d^{n+1} \quad (2.58)$$

Chapter 3

Population Balances

3.1 Population Balance Equation

In this section, the derivation of PBE [36] is discussed for one dimensional case.

Consider a population of particles distributed according to their size v which we shall take to be the mass of the particle and allow it to vary between 0 and ∞ . The particles are uniformly distributed in space so that the number density is independent of external coordinates. Further, we assume for now that the environment does not play any explicit role in particle behaviour.

Such situation can be approximated, for example, in a crystallizer containing a highly supersaturated solution of the crystallizing solute. The process involves nucleation resulting in the formation of a rudimentary particle and its subsequent growth by transferring solute from the solution phase to the particle surface.

In actuality, in addition to mass transfer, heat transfer also occurs, serving to remove the heat of crystallization, although the latter is generally considered negligible. If the nucleation and growth rates may remain relatively unaffected as crystallization progresses. This unnecessarily restrictive assumption is made only for simplifying the preliminary derivation of the PBE.

We let $G(v, t)$ be the growth rate of the particle size v . The particles may be viewed as distributed along the size coordinate and embedded on a string deforming with growth rate $G(v, t)$. Take an arbitrary region $[a, b]$

on the stationary size coordinate with respect to which the string with the embedded particles is deforming. We are interested in the rate of change of the number of particles in the size interval. As the string deforms, particles commute through the interval $[a, b]$ across the end point a and b , changing the number of particles in the interval.

If we denote the number density by $f(v, t)$, the rate of change in the number of particles in $[a, b]$ caused by this traffic at a and b is given by

$$G(a, t)f(a, t) - G(b, t)f(b, t).$$

The first term of which represents the particle in flux at a and the second particle out flux at b . Assume for the present that there is no other way in which the number of particles in the interval $[a, b]$ can change. Then we may write for the number balance in the interval $[a, b]$

$$\begin{aligned} \frac{d}{dt} \int_a^b f(v, t) dv &= G(a, t)f(a, t) - G(b, t)f(b, t) \\ \Rightarrow \int_a^b \left[\frac{\partial f(v, t)}{\partial t} + \frac{\partial}{\partial v} (G(v, t)f(v, t)) \right] &= 0 \end{aligned} \quad (3.1)$$

because all functions involved are assumed to be sufficiently smooth. Since the interval $[a, b]$ in equation (3.1) is arbitrary, the smoothness of the integrand implies that it vanishes altogether. Thus, we have PBE

$$\frac{\partial f(v, t)}{\partial t} + \frac{\partial}{\partial v} (G(v, t)f(v, t)) = 0. \quad (3.2)$$

The equation (3.2) must be supplemented with initial and boundary conditions. If we have started with no particles, we set $f(v, 0) = 0$. For the boundary condition we let the nucleation rate be n_0 particles per unit time and assume that the newly formed particles have mass zero. This rate should be the same as the particle in flux at $v = 0$. Thus

$$G(0, t)f(0, t) = n_0, \quad (3.3)$$

which is the required boundary condition. If equation (3.2) is integrated over all particle masses one obtains

$$\frac{dN}{dt} = \frac{d}{dt} \int_0^\infty f(v, t) dv = G(0, t)f(0, t) - G(\infty, t)f(\infty, t) = n_0. \quad (3.4)$$

The equality on the extreme right arises from the fact that particles can increase in number in this process only by nucleation. From Equations (3.3) and the (3.4), we conclude that

$$G(\infty, t)f(\infty, t) = 0, \quad (3.5)$$

which is sometimes referred to as a regularity condition. It does not insist that the number density itself vanish at infinite mass if the growth rate vanishes for large particles. If, however, the growth rate does not vanish for larger particles, Equation (3.5) implies that the number density must vanish for arbitrarily large sizes.

In the above derivation, we did not envisage the birth and death of particles in the interval $[a, b]$. For example, drops in RDC(Rotating Disc Contactor) may undergo breakage and/or aggregation contributing to the birth and death of particles in the interval of the interest. To assess the rate of this contribution, detailed modeling of breakage and aggregation processes will be needed. Suppose the net rate of generation of particles in the size range v to $v + dv$ is described by $h(v, t)dv$ where the identity of $h(v, t)$ would depend on the model of breakage and aggregation. In that case equation (3.1) must be replaced by

$$\int_a^b \left[\frac{\partial f(v, t)}{\partial t} + \frac{\partial}{\partial v}(G(v, t)f(v, t)) - h(v, t) \right] dv = 0$$

so that the PBE becomes

$$\frac{\partial f(v, t)}{\partial t} + \frac{\partial}{\partial v}(G(v, t)f(v, t)) = h(v, t). \quad (3.6)$$

Initial condition will be same. The total number balance will be

$$\frac{dN}{dt} = n_0 + \int_0^\infty h(v, t)dv$$

and the regularity condition also holds.

Suppose we relax the constraint that the above particle behaviour is independent of the environment. Consider the continuous phase to be described by a scalar quantity c , which is assumed to be uniform in space. In a well mixed crystallizer, c may represent the supersaturation at the surface of the drops. We introduce the following additional features,

- (1) The nucleation rate depends on c , $n_0 = n_0(c)$.
- (2) The growth rate may also be assumed to depend on c , i.e., $G = G(v, c, t)$.
- (3) The growth process depletes the supersaturation at a rate proportional to the growth rate of the drops, the proportionality being depend out on

particle size, i.e., at the rate $\alpha(v)G(v, c, t)$.

The net birth rate h may or may not depend on c . In this case, the process of the derivation of the PBE used earlier is not influenced in any way, and so the proper substitute for Equation (3.6) is given by

$$\frac{\partial f(v, t)}{\partial t} + \frac{\partial}{\partial v}(G(v, c, t)f(v, t)) = h(v, c, t). \quad (3.7)$$

The initial conditions remains the same as before while the boundary conditions recognizes the dependence of the nucleation and growth rates on c . Thus

$$G(0, c, t)f(0, t) = n_0(c). \quad (3.8)$$

Equation (3.7) must be coupled with a differential equation for c accounting for its depletion because of the growth of all the particles in the population. This is easily found to be

$$\frac{dc}{dt} = - \int_0^\infty \alpha(v)G(v, c, t)f(v, t)dv. \quad (3.9)$$

An initial condition for c now completes the formulation of the problem.

In general case, the PBE can be written as

$$\frac{\partial f}{\partial t} + \nabla_v \cdot Gf + \nabla_x \cdot uf = h. \quad (3.10)$$

where u is the velocity of the droplets.

3.1.1 Breakage Process

The net birth rate $h(v, t)$ which appears on the right hand side of the PBE (3.6) can be expressed as the difference between a "source" term $h^+(v, t)$ and a "sink" term $h^-(v, t)$, both of which are due to breakage processes. Our objective is to provide a characterization of the breakage process so as to calculate the foregoing source and sink terms.

The breakage functions

If breakup of particles occurs independently of each other and let $b(v, x, t)$ i.e. the specific "breakage rate" of particles at time t , to represents the fraction of particles breaking per unit time. Then we have

$$h^-(v, x, t) = b(v, x, t)f(v, x, t), \quad (3.11)$$

as the average number of particles of state (v, x) "lost" by breakage per unit time. In order to characterize the source term we should be concerned about the following quantities :

$\nu(v, x, t)$: The average number of particles formed from the breakup of a single particle.

$\beta(v | v')$: The probability of the drop of size v' breaking into the drop of size v . So we can write the source term for the particles of state (v, x) originating from break up as

$$h^+(v, x, t) = \int_0^\infty \nu(v', x, t)b(v', x, t)\beta(v | v')f(v', x, t)dv. \quad (3.12)$$

The spatially homogeneous population balance equation for the breakage process just discussed becomes

$$\frac{\partial f(v, t)}{\partial t} + \frac{\partial}{\partial v}(G(v, t)f(v, t)) = \int_0^\infty \nu(v', t)b(v', t)\beta(v | v')f(v', t)dv - b(v, t)f(v, t). \quad (3.13)$$

3.1.2 Aggregation Process

We are concerned here with particulate events in which two or more particles may be involved. Aggregation processes occur commonly in nature and engineering processes. It is conceivable that several adjacent particles could simultaneously aggregate.

The Aggregation Frequency

We let the probability that a particle of state (v, x) and another particle of state (v', x') , both present at time t in a continuous phase will aggregate in the time interval $[t, t + dt)$ to be given by

$$a(v, x; v', x', t)dt. \quad (3.14)$$

The source function, which represents the rate of formation of particles of volume v by aggregation of small particles, is computed as follows. From the conservation of mass, we have particle of volume $v - v'$ aggregating with particles of volume v' to produce particles of volume v . Clearly as v' varies between

0 and v , so also does $v - v'$ so that each pair in the set $[v - v', v']$; $0 < v' < v$ is considered twice. Thus the source term can be written as

$$h^+(v, x, t) = \frac{1}{2} \int_0^v a(v - v', v') f(v - v', x, t) f(v', x, t) dv'$$

and the sink term represents as :

$$h^-(v, x, t) = f(v, x, t) \int_0^\infty a(v, v') f(v', x, t) dv'$$

The number density function $f(v, x, t)$ must then satisfy the population balance equation

$$\begin{aligned} \frac{\partial f(v, t)}{\partial t} + \frac{\partial}{\partial v}(G(v, t)f(v, t)) &= \frac{1}{2} \int_0^v a(v - v', v') f(v - v', t) f(v', t) dv' \\ &\quad - f(v, t) \int_0^\infty a(v, v') f(v', t) dv'. \end{aligned} \quad (3.15)$$

By combining the Equation (3.13) and Equation (3.15), we get the complete spatial homogeneous population balance equation as following

$$\begin{aligned} \frac{\partial f(v, t)}{\partial t} + \frac{\partial}{\partial v}(G(v, t)f(v, t)) &= \frac{1}{2} \int_0^v a(v - v', v') f(v - v', t) f(v', t) dv' \\ &\quad - f(v, t) \int_0^\infty a(v, v') f(v', t) dv' \\ &\quad + \int_0^\infty \nu(v', t) b(v', t) \beta(v | v') f(v', t) dv - b(v, t) f(v, t). \end{aligned} \quad (3.16)$$

3.1.3 The Bivariate Population Balance Equation (BPBE)

In the previous subsection, the derivation of mono-variate PBE was shown where we considered only one internal coordinate (mass of the particle). In this subsection, the form of bivariate PBE is discussed where two internal coordinates are considered. In a continuous liquid extraction column, the state of any given droplet is represented by a bivariate (joint) density function $n(v, cy; z, t)$ per unit volume of the contractor. This allows the discontinuous macroscopic (breakage and coalescence) and the continuous microscopic (interphase mass transfer) events to be coupled in a single spatially distributed

population balance equation (SDPBE). All the quantities with the index c denotes the continuous phase and index d denotes the dispersed phase. The general SDPBE for describing the hydrodynamics and mass transfer in one spatial domain can be written as [5]:

$$\begin{aligned} \frac{\partial n(\Psi)}{\partial t} + \frac{\partial[u_d n(\Psi)]}{\partial z} + \sum_{i=1}^2 \frac{\partial[\zeta_i n(\Psi)]}{\partial \zeta_i} = \frac{\partial}{\partial z} \left[D_d \frac{\partial n(\Psi)}{\partial z} \right] \\ + \frac{Q_d^{in}}{A_c} n^{in}(v, c_d; t) \delta(z - z_d) + \Upsilon\{\Psi\}. \end{aligned} \quad (3.17)$$

In this equation the components of the vector Ψ are those for the droplet internal coordinates (volume and solute concentration), the external coordinate z and the time t . The velocity vector ζ represents particle growth along size and concentration coordinates. The source term $\Upsilon\{\Psi\}$ represents the net number of droplets produced by breakage and coalescence per unit volume and unit time in the coordinates range $\zeta \pm \partial\zeta$, where, u_d is the velocity and D_d is the axial dispersion coefficient. The first term on the right hand side is a point source term representing the rate at which the droplets entering the column with volumetric flow rate (Q_d^{in}) that is perpendicular to the column cross-sectional area (A_c) at a location (z_d) with an inlet number density (n^{in}). Note that equation (3.17) is coupled to the solute balance in the continuous phase through the velocity vector ζ and hence they have to be solved simultaneously.

3.2 Method of Solving the PBE

This section is devoted to the methods to solve PBE. In some particular cases, it is possible to solve spatially homogeneous PBE analytically but in general the numerical solution is required because of the nature of PBE as it is an integro-partial differential equation. First, the possible analytical solutions of PBE are shown. Ramkrishna [36] has used the Laplace transform to solve spatially homogeneous PBE in the case of some particular aggregation kernels. Later on McCoy and Madras [52] have extended it for the case of a particular constant aggregation and non-constant breakage kernels both. In this work, we extend the analytical solution of spatially homogeneous PBE to the case of non-constant and non-linear breakage and coalescence kernels.

3.2.1 Analytical Methods

In this subsection, we solve the PBE analytically using the Laplace transform; first, we consider the PBE with aggregation term only and after that we take the PBE with both aggregation and breakage terms.

Aggregation

We can write spatially homogeneous PBE without growth process for aggregation as

$$\begin{aligned} \frac{\partial f_1(v, t)}{\partial t} = & \frac{1}{2} \int_0^v a(v-v', v') f_1(v-v', t) f_1(v', t) dv' \\ & - f_1(v, t) \int_0^\infty a(v, v') f_1(v', t) dv' \end{aligned} \quad (3.18)$$

subject to the initial condition

$$f(v, 0) = N_0 g(v). \quad (3.19)$$

Assuming that particle volume v has been nondimensionalized with respect to the average particle size at $t = 0$, so that

$$\int_0^\infty v g(v) dv = 1. \quad (3.20)$$

It is convenient to nondimensionalize the PBE using dimensionless variables by introducing the dimensionless quantities

$$\begin{aligned} \tau \equiv a_0 N_0 t, \quad f(v, \tau) \equiv \frac{1}{N_0} f_1(v, t), \quad \alpha(v, v') \equiv \frac{a(v, v')}{a_0}, \\ \nu(\tau) \equiv \int_0^\infty f(v, \tau) dv = \frac{N(t)}{N_0} \end{aligned}$$

where a_0 is some characteristic value of the aggregation frequency. And so the dimensionless PBE may be written as

$$\begin{aligned} \frac{\partial f(v, \tau)}{\partial \tau} = & \frac{1}{2} \int_0^v \alpha(v-v', v') f(v-v', \tau) f(v', \tau) dv' \\ & - f(v, \tau) \int_0^\infty \alpha(v, v') f(v', \tau) dv' \end{aligned} \quad (3.21)$$

which must subject to the initial condition

$$f(v, 0) = g(v). \quad (3.22)$$

Because of Equation (3.20) and the conservation of mass, it emerges that

$$\int_0^{\infty} v f(v, \tau) dv = 1. \quad (3.23)$$

We shall develop the solution for Equation (3.21) and Equation (3.22) by defining the Laplace transform with respect to the size variable volume v as

$$\bar{f}(s, \tau) = \int_0^{\infty} f(x, \tau) e^{-sv} dv. \quad (3.24)$$

Note in particular that

$$\bar{f}(0, \tau) = \nu(\tau). \quad (3.25)$$

The constant aggregation kernel

Taking the Laplace transform of equation (3.21) for the case $\alpha(v, v') \equiv 1$, we obtain

$$\begin{aligned} \frac{\partial \bar{f}(s, \tau)}{\partial \tau} &= \frac{1}{2} \int_0^{\infty} dv \quad e^{-sv} \int_0^v f(v - v', t) f(v', t) dv' \\ &\quad - \int_0^{\infty} dv \quad e^{-sv} f(v, t) \times \int_0^{\infty} f(v', \tau) dv'. \end{aligned}$$

By modifying the limits of integration in the first term on the right-hand side of the preceding equation, we get

$$\begin{aligned} \frac{\partial \bar{f}(s, \tau)}{\partial \tau} &= \frac{1}{2} \int_0^{\infty} dv' f(v', \tau) e^{-sv'} \int_0^{\infty} e^{-su} f(u, t) du \\ &\quad - \int_0^{\infty} dv \quad e^{-sv} f(v, t) \times \int_0^{\infty} f(v', \tau) dv' \end{aligned} \quad (3.26)$$

where we have set $v - v' = u$ as a new integration variable. Equation (3.26) becomes

$$\frac{\partial \bar{f}(s, \tau)}{\partial \tau} = \frac{1}{2} \bar{f}(s, \tau)^2 - \nu(\tau) \bar{f}(s, \tau). \quad (3.27)$$

Taking the Laplace transform of the initial condition (3.22), we have the initial condition for (3.27) given by

$$\bar{f}(s, 0) = \bar{g}(s). \quad (3.28)$$

By letting $s = 0$ in Equation (3.27), and noting $\bar{f}(s, 0) = \nu(\tau)$, we obtain the following ordinary differential equation in $\nu(\tau)$:

$$\frac{d\nu(\tau)}{d\tau} = -\frac{1}{2} \nu(\tau)^2, \quad \nu(0) = 1$$

whose solution is given by

$$\nu(\tau) = \frac{2}{(2 + \tau)}. \quad (3.29)$$

Dividing Equation (3.29) by \bar{f}^2 , we may rewrite it as the following linear differential equation in $\frac{1}{\bar{f}}$:

$$\frac{\partial}{\partial \tau} \left[\frac{1}{\bar{f}} \right] = -\frac{1}{2} + \nu(\tau) \left[\frac{1}{\bar{f}} \right].$$

After solving above equation, we get

$$\bar{f}(s, \tau) = \left(\frac{2}{2 + \tau} \right)^2 \frac{\bar{g}(s)}{1 - \left(\frac{\tau}{2 + \tau} \right) \bar{g}(s)}. \quad (3.30)$$

If the initial size distribution is monodisperse with dimensionless size unity, then $\bar{g}(s) = e^s$ and the transform (3.30) may be inverted by using the expansion of $(1 - w)^{-1}$ in powers of w , which converges for w less than unity. Thus

$$\bar{f}(s, \tau) = \left(\frac{2}{2 + \tau} \right) \sum_{n=0}^{\infty} \left(\frac{\tau}{2 + \tau} \right)^n e^{-s(n-1)},$$

After taking inverse Laplace transform of above equation, we get

$$f(v, \tau) = \left(\frac{2}{2 + \tau} \right) \sum_{n=0}^{\infty} \left(\frac{\tau}{2 + \tau} \right)^n \delta(v - n - 1). \quad (3.31)$$

The sum aggregation kernel

Taking the Laplace transform of Equation (3.21) for the case $\alpha(v, v') \equiv v + v'$, we get

$$\begin{aligned} \frac{\partial \bar{f}(s, \tau)}{\partial \tau} &= \frac{1}{2} \int_0^{\infty} dv \ e^{-sv} \int_0^v v f(v - v', t) f(v', t) dv' \\ &\quad - \int_0^{\infty} dv \ e^{-sv} f(v, t) \times \int_0^{\infty} (v + v') f(v', \tau) dv'. \end{aligned}$$

By modifying the limits of integration in the first term on the right-hand side of the preceding equation, we get

$$\begin{aligned} \frac{\partial \bar{f}(s, \tau)}{\partial \tau} &= \frac{1}{2} \int_0^{\infty} dv' f(v', \tau) e^{-sv'} \int_0^{\infty} (v' + u) e^{-su} f(u, t) du \\ &\quad - \int_0^{\infty} dv \ e^{-sv} f(v, t) \times \int_0^{\infty} (v + v') f(v', \tau) dv'. \end{aligned} \quad (3.32)$$

Considering that

$$\frac{\partial \bar{f}(s, \tau)}{\partial s} = - \int_0^\infty v f(v, \tau) e^{-sv} dv$$

and using Equation (3.20), we may write

$$\frac{\partial \bar{f}(s, \tau)}{\partial \tau} = - \frac{\partial \bar{f}(s, \tau)}{\partial s} [\bar{f}(s, \tau) - \nu(\tau)] - \bar{f}(s, \tau), \quad (3.33)$$

which is subject to the initial condition (3.28). By letting $s = 0$ in Equation (3.32), we obtain the following ordinary differential equation in $\nu(\tau)$

$$\frac{d\nu(\tau)}{d\tau} = -\nu(\tau), \quad \nu(0) = 1$$

whose solution is given by $\nu(\tau) = e^{-\tau}$. Equation (3.33) may be solved by the method of characteristics. The characteristics in the three dimensional space (τ, s, \bar{f}) coordinates are given by

$$\frac{ds}{d\tau} = (\bar{f} - \nu), \quad \frac{d\bar{f}}{d\tau} = -\bar{f}, \quad s[0] = s_0, \quad \bar{f}[0] = \bar{g}(s_0). \quad (3.34)$$

After solving above Equations (3.15), we obtain the value for \bar{f} along the characteristic starting at $s = s_0$ and $\tau = 0$ as :

$$\bar{f}[\tau] = \bar{g}(s_0) e^{-\tau}. \quad (3.35)$$

Using the solution for $\nu(\tau)$, we solve the differential equation for s to obtain

$$\begin{aligned} \frac{ds}{d\tau} &= [\bar{g}(s_0) - 1] e^{-\tau} \\ s - s_0 &= (1 - e^{-\tau}) [\bar{g}(s_0) - 1], \end{aligned} \quad (3.36)$$

which is difficult to solve analytically for s_0 in terms of s and τ and therefore thwarts this approach to a solution. Now we define one transformation for \bar{f} as

$$\bar{f}(s, \tau) = \bar{\phi}(s, \tau) \psi(\tau) \quad (3.37)$$

where $\psi(\tau)$ will be chosen so that the partial differential equation in $\bar{\phi}(s, \tau)$ arising from Equation (3.33) displays only derivative of $\bar{\phi}(s, \tau)$ with respect to τ and s . Substituting (3.37) in (3.33), one obtains

$$\psi \frac{\partial \bar{\phi}(s, \tau)}{\partial \tau} = -\psi \frac{\partial \bar{\phi}(s, \tau)}{\partial s} [\bar{\phi}(s, \tau) \psi - \nu(\tau)] - \bar{\phi}(s, \tau) \left[\frac{d\psi}{d\tau} + \psi \right].$$

In order to eliminate the term $\bar{\phi}(s, \tau)$, we must set its coefficient in the preceding equal to zero, which gives $\psi(\tau) = e^{-\tau}$ interestingly the same as $\nu(\tau)$. If we use this result, the partial differential equation in $\bar{\phi}(s, \tau)$ becomes

$$\frac{\partial \bar{\phi}(s, \tau)}{\partial \tau} = -\psi \frac{\partial \bar{\phi}(s, \tau)}{\partial s} [\bar{\phi}(s, \tau) - 1]. \quad (3.38)$$

It is now convenient to define an alternative independent variable T by

$$dT = \psi(\tau) d\tau, \quad T = 1 - e^{-\tau},$$

the second of which follows from the first by arbitrarily setting $T = 0$ at $\tau = 0$. Then Equation (3.38) may be written as

$$\frac{\partial \bar{\Phi}(s, T)}{\partial T} = -\frac{\partial \bar{\Phi}(s, T)}{\partial s} [\bar{\Phi}(s, T) - 1], \quad (3.39)$$

where we have set $\bar{\Phi}(s, T) = \bar{\phi}(s, \tau)$. The initial condition for $\bar{\Phi}(s, T)$ is given by

$$\bar{\Phi}(s, 0) = \bar{g}(s). \quad (3.40)$$

The characteristic equations are then given by

$$\frac{ds}{dT} = (\bar{\Phi} - 1), \quad \frac{d\bar{\Phi}}{dT} = 0, \quad s[0] = s_0, \quad \bar{\Phi}[0] = \bar{g}(s_0).$$

The above are readily solved to obtain

$$s = s_0 + [\bar{g}(s_0) - 1]T, \quad \bar{\Phi}(s, T) = \bar{g}(s_0),$$

$$\bar{\Phi}(s, T) = \bar{g}(s + (1 - \bar{\Phi}(s, T))T), \quad (3.41)$$

The expression (3.41) can also be considered for direct inversion of the Laplace transform of the function $\bar{\Phi}(s, T)$ by expanding it in Taylor series about $T = 0$

$$\bar{\Phi}(s, T) = \bar{g}(s) + \sum_{k=1}^{\infty} \frac{T^k}{k!} \left. \frac{\partial^k \bar{\Phi}(s, T)}{\partial T^k} \right|_{T=0}. \quad (3.42)$$

From (3.41), we can write

$$\left. \frac{\partial^k \bar{\Phi}(s, T)}{\partial T^k} \right|_{T=0} = \frac{-1}{(k+1)} \frac{d^k}{ds^k} [1 - \bar{g}(s)]^{k+1},$$

which may be written using the binomial expansion as

$$\left. \frac{\partial^k \bar{\Phi}(s, T)}{\partial T^k} \right|_{T=0} = -\frac{-1}{(k+1)} \sum_{r=1}^{k+1} (-1)^r \frac{(k+1)!}{r!(k+1-r)!} \frac{d^k \bar{g}(s)^r}{ds^k}. \quad (3.43)$$

Substituting (3.43) in (3.42), one obtains

$$\bar{\Phi}(s, T) = \bar{g}(s) - \sum_{k=1}^{\infty} \sum_{r=1}^{k+1} (-1)^r \frac{T^k}{r!(k+1-r)!} \frac{d^k \bar{g}(s)^r}{ds^k}. \quad (3.44)$$

It can be written as

$$\bar{\Phi}(s, T) = \sum_{r=1}^{\infty} \sum_{k=r-1}^{\infty} (-1)^{r-1} \frac{T^k}{r!(k+1-r)!} \frac{d^k \bar{g}(s)^r}{ds^k}.$$

If we redefine the summation index within the inner sum on the right hand side of the equation as $j = k + 1 - r$, the foregoing expression becomes

$$\bar{\Phi}(s, T) = \sum_{r=1}^{\infty} \frac{(-1)^{r-1} T^{r-1}}{r!} \sum_{j=1}^{\infty} \frac{T^j}{j!} \frac{d^{j+r-1} \bar{g}(s)^r}{ds^{j+r-1}}. \quad (3.45)$$

It is now convenient to invert the preceding Laplace transform within the inner sum as follows. The inverse Laplace transform of the derivative appearing in the inner sum of (3.45) is given by

$$L^{-1} \left[\frac{d^{j+r-1} \bar{g}(s)^r}{ds^{j+r-1}} \right] = (-v)^{j+r-1} L^{-1}(\bar{g}(s)^r).$$

which, on substitution into the Laplace inverse of (3.45), gives

$$\begin{aligned} \Phi(v, T) &= \sum_{r=1}^{\infty} \frac{(vT)^{r-1}}{r!} L^{-1}(\bar{g}(s)^r) \sum_{j=0}^{\infty} \frac{(-vT)^j}{j!}. \\ \implies \Phi(v, T) &= e^{-vT} \sum_{r=1}^{\infty} \frac{(vT)^{r-1}}{r!} L^{-1}(\bar{g}(s)^r). \end{aligned} \quad (3.46)$$

If we now assume that the initial particle size distribution is the Dirac delta distribution $\delta(v - 1)$, then $\bar{g}(s) = e^{-s}$ and the foregoing expression becomes

$$\Phi(v, T) = e^{-vt} \sum_{r=1}^{\infty} \frac{(vT)^{r-1}}{r!} \delta(v - r). \quad (3.47)$$

Thus the dimensionless number density $f(v, t)$ for the aggregation problem with the sum frequency is obtained as

$$f(v, \tau) = e^{-[\tau + v(1 - e^\tau)]} \sum_{r=1}^{\infty} \frac{[x(1 - e^\tau)]^{r-1}}{r!} \delta(v - r).$$

Solution for other initial conditions can of course be obtained by inverting afresh the Laplace transform (3.46).

The product aggregation kernel

Taking the Laplace transform of Equation (3.21) for the case $\alpha(v, v') \equiv v.v'$, we obtain

$$2\frac{\partial \bar{f}(s, \tau)}{\partial \tau} - 2\frac{\partial \bar{f}(s, \tau)}{\partial s} - \left(\frac{\partial \bar{f}(s, \tau)}{\partial s}\right)^2 = 0 \quad (3.48)$$

which is subject to the initial condition (3.28). By letting $s = 0$ in Equation (3.48), we obtain the following ordinary differential equation in $\nu(\tau)$

$$2\frac{d\nu(\tau)}{d\tau} + 1 = 0, \quad \nu(0) = 1$$

whose solution is given by $\nu(\tau) = 1 - \frac{1}{2}\tau$. After solving the Equation (3.48), we get

$$\bar{f}(s, \tau) = -C\tau + s(1 + \sqrt{1 - 2C}). \quad (3.49)$$

By using the initial condition $f(s, 0) = g(s)$, we obtain

$$C = \frac{1}{2} \frac{g(s)(-g(s) + 2s)}{s^2}.$$

If we take initial distribution $g(\tau) = e^{-\tau}$ then $g(s)$ will be $\frac{1}{(1+s)}$. Now replacing $g(s)$ in above equation, we obtain

$$C = \frac{1}{2} \frac{2s^2 + 2s - 1}{s^2(1+s)^2}.$$

So Equation (3.49) becomes

$$\bar{f}(s, \tau) = -\frac{1}{2} \frac{2s^2 + 2s - 1}{s^2(1+s)^2} \tau + s \left(1 + \frac{\sqrt{s^4 + 2s^3 - s^2 - 2s + 1}}{s(1+s)}\right). \quad (3.50)$$

After taking the inverse Laplace transform of above equation, we get

$$f(v, \tau) = -\frac{\tau}{2}(4 - v - 4e^{-v} - ve^{-v}) + 2\delta(v - 1) - e^{-v}. \quad (3.51)$$

Aggregation and Breakage both

The nondimensionalized PBE for the case of aggregation and breakage both will be written as

$$\begin{aligned} \frac{\partial f(v, t)}{\partial t} = & \frac{1}{2} \int_0^v \alpha(v - v', v') f(v - v', t) f(v', t) dv' \\ & - f(v, t) \int_0^\infty \alpha(v, v') f(v', t) dv' \\ & + \int_0^\infty m(v', t) b(v') \beta(v | v') f(v', t) dv - b(v) f(v, t). \end{aligned} \quad (3.52)$$

We solve the PBE (3.52) for different combination of breakage and coalescence kernels which are shown in following subsections.

The constant aggregation kernel and the non-constant breakage kernel

By taking the Laplace transform of above Equation (3.52) for the case $\alpha(v, v') = k_1$, $\beta(v | v') = \frac{1}{v'}$, $m(v, t) = 2$ and $b(v) = k_2 v$, where k_1 and k_2 are constants, we get

$$\begin{aligned} \frac{\partial \bar{f}(s, \tau)}{\partial \tau} = & \frac{1}{2} [\bar{f}(s, \tau)]^2 - \bar{f}(s, \tau) \nu(\tau) \\ & + [\nu(\infty)]^2 \frac{\nu \tau - \bar{f}(s, \tau)}{s} + \frac{1}{2} [\nu(\infty)]^2 \frac{\partial \bar{f}(s, \tau)}{\partial s} \end{aligned} \quad (3.53)$$

with initial conditions

$$\bar{f}(s, 0) = \frac{1}{(1 + s)} \quad \text{and} \quad \bar{f}(0, \tau) = \nu(\tau), \quad (3.54)$$

where $\nu(\infty) = \sqrt{2k_2 N_1 / k_1}$, N_1 is the first moment given by $N_1(t) = \int_0^\infty f_1(v, t) v dv$. Letting $s = 0$ in Equation (3.53) gives the following ordinary differential equation in $\nu(\tau)$

$$\frac{d\nu(\tau)}{d\tau} = \frac{[\nu(\infty)]^2 - [\nu(\tau)]^2}{2}, \quad \nu(0) = 1 \quad (3.55)$$

which has the solution

$$\nu(\tau) = \frac{\nu(\infty) [1 + \nu(\infty) \tanh(\nu(\infty) \tau / 2)]}{\nu(\infty) + \tanh(\nu(\infty) \tau / 2)}. \quad (3.56)$$

After solving the Equation (3.53), we get

$$\bar{f}(s, \tau) = \frac{[\nu(\tau)]^2}{s + \nu(\tau)}. \quad (3.57)$$

Taking inverse Laplace transform of Equation (3.57), one obtains

$$f(v, \tau) = [\nu(\tau)]^2 e^{-v\nu(\tau)}, \quad (3.58)$$

where $\nu(\tau)$ is given by Equation (3.56). Thus we get the dimensionless number density $f(v, t)$ for the constant aggregation and non-constant breakage kernels.

The non-constant aggregation and breakage kernels

Case1 : By taking the Laplace transform of Equation (3.52) for the case $\alpha(v, v') = v + v'$, $\beta(v | v') = \frac{1}{v'}$, $m(v, t) = 2$ and $b(v) = kv$, where k is a constant, we get

$$\begin{aligned} \frac{\partial \bar{f}(s, \tau)}{\partial \tau} = & -\frac{\partial \bar{f}(s, \tau)}{\partial s} (\bar{f}(s, \tau) - \nu(\tau)) - \bar{f}(s, \tau) + \frac{k}{a_0 N_0} \frac{\partial \bar{f}(s, \tau)}{\partial s} \\ & + \frac{2k}{a_0 N_0 s} (\nu(\tau) - f(s, \tau)). \end{aligned} \quad (3.59)$$

By letting $s = 0$ in Equation (3.59), and noting $\bar{f}(s, 0) = \nu(\tau)$, we obtain the following ordinary differential equation in $\nu(\tau)$:

$$\frac{d\nu(\tau)}{d\tau} + \nu(\tau) = \frac{k}{a_0 N_0}, \quad \nu(0) = 1. \quad (3.60)$$

After solving Equation (3.60), we obtain

$$\nu(\tau) = \frac{k}{a_0 N_0} + \left(1 - \frac{k}{a_0 N_0}\right) e^{-\tau}. \quad (3.61)$$

By putting $\nu(\tau) = \frac{N(t)}{N_0}$ and $\tau = a_0 N_0 t$, we get the expression for the number density as

$$N(t) = \frac{1}{a_0} [k + (a_0 N_0 - k) e^{-a_0 N_0 t}]. \quad (3.62)$$

Case2 : By taking the Laplace transform of Equation (3.52) for the case $\alpha(v, v') = v.v'$, $\beta(v | v') = \frac{1}{v'}$, $m(v, t) = 2$ and $b(v) = kv$, where k is a constant, we get

$$\frac{\partial \bar{f}(s, \tau)}{\partial \tau} = \frac{1}{2} \left(\frac{\partial \bar{f}(s, \tau)}{\partial s} \right)^2 + \left(\frac{a_0 N_0 + k}{a_0 N_0} \right) \frac{\partial \bar{f}(s, \tau)}{\partial s} + \frac{2k}{a_0 N_0} \frac{1}{s} (\nu(\tau) - f(s, \tau)). \quad (3.63)$$

By letting $s = 0$ in Equation (3.63), and noting $\bar{f}(s, 0) = \nu(\tau)$, we obtain the following ordinary differential equation in $\nu(\tau)$:

$$\frac{d\nu(\tau)}{d\tau} + \frac{1}{2} = \frac{k}{a_0 N_0}, \quad \nu(0) = 1. \quad (3.64)$$

The above Equation (3.64) is readily solved to obtain

$$\nu(\tau) = 1 + \left(\frac{k}{a_0 N_0} - \frac{1}{2} \right) \tau. \quad (3.65)$$

By putting $\nu(\tau) = \frac{N(t)}{N_0}$ and $\tau = a_0 N_0 t$, we get the expression for the number density as

$$N(t) = N_0 \left[1 - \frac{1}{2} (a_0 N_0 - 2k)t \right]. \quad (3.66)$$

Thus we get the number density or zeroth moment for non-constant aggregation and breakage kernels.

3.2.2 Numerical Methods

We have seen in the previous section that the analytical solutions of PBEs are available for a few cases where the coalescence and breakup kernels have a simple form and when the particle size distribution (PSD) has a particular initial shape.

In many cases, even though the analytical solution of the PSD is available, some properties of PSD (e.g. mean diameter, mean surface area, etc.) need to be derived by numerical integration of the analytical solution. Computationally speaking, this procedure is more expensive than solving the PBE by discretization techniques.

However, the analytical solutions remain a valuable source for testing and validating numerical techniques. In applications of particular interest, numerical techniques are needed to solve the PBE. The most commonly used

techniques are Monte Carlo method, the Methods of Classes (MC) and the method of moments. Hereafter, because of their relevance in CFD applications, the method of classes, the quadrature method of moments (QMOM), the parallel parent and daughter classes technique (PPDC), the sectional quadrature method of moments (SQMOM), one primary and one secondary particle method of moments (OPOSPM) and the multi primary and one secondary particle method of moments (MPOSPM) are discussed.

We will validate the numerical methods for following two cases :

case 1 : Splitting in a continuous stirred vessel with simplified splitting functions [22]. The distribution is exponential with respect to the particle volume at inflow boundary ($f^{in} = 3d^2e^{-d^3}$), the splitting frequency is proportional to the square of the particle volume ($\Gamma = d^6$), the daughter particle distribution is uniform with respect to the mother particle volume ($\beta = 6d^2/d^3$), the initial condition is zero ($f(d, 0) = 0$), the minimum and maximum particle sizes are 0.001 and 2 respectively and the vessel residence time τ is 50 sec.

case 2 : Splitting and aggregation in a batch stirred tank with dimensionless time $T = 10$, constant aggregation frequency = 1, non-constant splitting frequency = $0.1v$, $d_{min} = 0.001$ and $d_{max} = 3$. The analytical solution is given by McCoy and Madras (2003).

Method of classes

Using the method of classes, the internal coordinate size range is subdivided into M subintervals in a partition $P_M \equiv \{0 = v_1, v_2, \dots, v_M, v_{M+1} = \infty\}$. The number of particles between the i^{th} subinterval is

$$N_i(t) = \int_{v_i}^{v_{i+1}} f(v, t) dv. \quad (3.67)$$

Approximating f by a finite set of Dirac's delta functions

$$f(v; t) \approx \sum_{i=1}^M N_i \delta(v - x_i) \quad (3.68)$$

the i^{th} class consists of all particles per unit of volume, N_i , present in the interval $I_i \equiv [v_i, v_{i+1})$, and is represented by a pivot size of abscissa, x_i , with $x_i \in [v_i, v_{i+1})$. When Equation (3.68) is substituted into PBE, and the latter

is integrated in the i^{th} generic subinterval, it yields

$$\begin{aligned} \frac{dN_i}{dt} &= \frac{1}{2} \sum_{j=1}^{i-1} N_j \sum_{(x_j+x_k) \in I_i} N_k a(x_j, x_k) - N_i \sum_{j=1}^M N_j a(x_i, x_j) \\ &+ \sum_{j=1}^M \gamma(x_j) N_j b(x_j) \int_{v_i}^{v_{i+1}} \beta(v/x_j) dv - b(x_i) N_i \quad (3.69) \\ &i = 1, \dots, M. \end{aligned}$$

Here $\int_{v_i}^{v_{i+1}} \beta(v/x_j) dv$ represents the fraction of daughter particles generated from the breakup of particles of size x_i , present in the size range $[v_i, v_{i+1})$.

When a linear grid partitioning is used, i.e. $x_i = ih$, where h is a constant, the consistency on the total number of particles is ensured as well as conservation of mass [36]. For a linear grid the discretized form of the PBE yields

$$\begin{aligned} \frac{dN_i}{dt} &= \frac{1}{2} \sum_{j=1}^{i-1} N_j N_{i-j} a(x_j, x_{i-j}) - N_i \sum_{j=1}^M N_j a(x_i, x_j) \\ &+ \sum_{j=1}^M \gamma(x_j) N_j b(x_j) \int_{v_i}^{v_{i+1}} \beta(v/x_j) dv - b(x_i) N_i \quad (3.70) \\ &i = 1, \dots, M. \end{aligned}$$

We solve the spatially homogeneous PBE by method of classes in the case of particular breakage and aggregation kernels. Then we compare the analytical results with numerical results for cases 1 and 2.

MC is validated for both cases. We can see good agreement of sauter mean diameter in Figures 3.2.2,3.2 but unfortunately, to get this agreement, we have to take 130 classes which is expensive in terms of computation. We have taken a fixed time step of 0.01 sec in both cases.

Since a uniform grid partitioning may require several hundreds of classes, with an unfeasible computational workload, several different methods of classes have been developed in the past in order to solve the PBE with a lower number of classes.

For the method of classes based on a fixed pivot size discretization with non-uniform grid there is a problem related to the allocation of the daughter

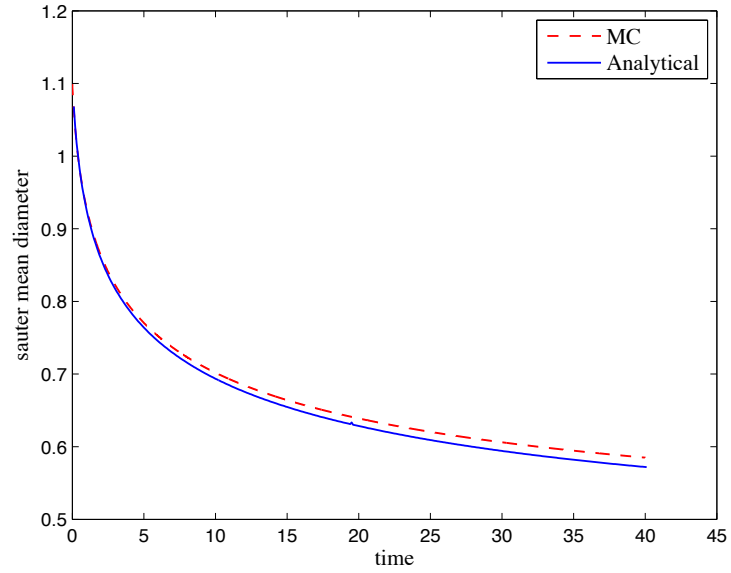


Figure 3.1: The sauter mean diameter for the breakage only.

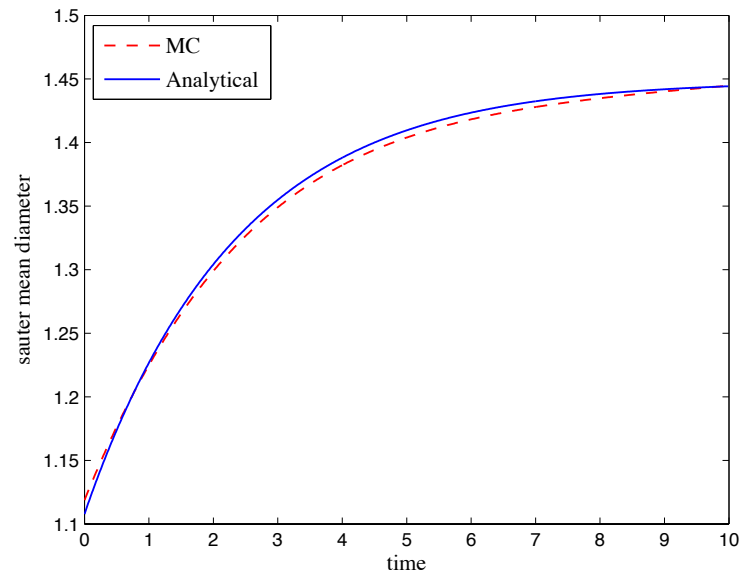


Figure 3.2: The sauter mean diameter for the breakage and aggregation both.

particles generated by breakup and coalescence, with different sizes than the pivot sizes. If these particles are assigned to the class they are falling into without any adjustment then only the zero order moment or total number density would be conserved but not the total population mass.

In the work of Batterham [53] the size domain is discretized in a geometrical series such that $v_{i+1}/v_i = 2$ and the daughter particles are allocated between the nearest neighbor in such a way to preserve the total population mass. Hounslow [54] used a correction parameter to predict correctly both mass and total number density of the population. Lister [55] extended the work of Hounslow [54] to an adjustable discretization of the size domain of the form $v_{i+1}/v_i = 2^{1/q}$, where q is an integer greater than zero. In the approach of Kumar and Ramkrishna [56], partition functions are determined so that from 2 to M arbitrary properties can be correctly predicted on an arbitrary domain size discretization. This redistribution is however responsible for numerical diffusion problems.

Method of Moments

Instead of solving the Particle Size Distribution (PSD) directly, as attempted by method of classes, the method of moments aim is to solve some of the PSD properties, for instance the lower order moments of the distribution. The solution of the population balance equation has been first proposed by Hulburt and Katz [57]. In their work they highlighted the promising possibilities but also the strong limitations of the method. Thus if $f(v;x,t)$ is the PSD in terms of the particle volume v , the k^{th} moments of the PSD is defined as follows :

$$m^{(k)}(x, t) = \int_0^{\infty} f(v; x, t) v^k dL. \quad (3.71)$$

The moments give important statistical descriptions on the population. The zero order moment ($k = 0$) represents the total number density of the population; the first order moment ($k = 1$) is the total mass per unit of volume of the population, and the fractional moments, $k = 1/3$ and $k = 2/3$ gives information on the mean diameter and on the mean surface area respectively. Considering the volume as the only initial coordinate, the generic k^{th} moment balance equation can be derived by multiplying PBE Equation (3.16)

by v^k and integrating over the internal coordinate domain

$$\begin{aligned} \frac{\partial}{\partial t} \int_0^\infty v^k f(v, t) dv &= \frac{1}{2} \int_0^\infty v^k \int_0^v \alpha(v - v', v') f(v - v', t) f(v', t) dv' dv \\ &\quad - \int_0^\infty v^k f(v, t) \int_0^\infty \alpha(v, v') f(v', t) dv' dv \\ &+ \int_0^\infty v^k \int_0^\infty m(v', t) b(v') \beta(v | v') f(v', t) dv' dv - \int_0^\infty v^k b(v) f(v, t) dv. \end{aligned} \quad (3.72)$$

Using the definition of moments of the particle size distribution given by Equation (3.71), Equation (3.72) yields

$$\begin{aligned} \frac{\partial m^{(k)}(v, t)}{\partial t} &= \frac{1}{2} \int_0^\infty v^k \int_0^v \alpha(v - v', v') f(v - v', t) f(v', t) dv' dv \\ &\quad - \int_0^\infty v^k f(v, t) \int_0^\infty \alpha(v, v') f(v', t) dv' dv \\ &+ \int_0^\infty v^k \int_0^\infty m(v', t) b(v') \beta(v | v') f(v', t) dv' dv - \int_0^\infty v^k b(v) f(v, t) dv. \end{aligned} \quad (3.73)$$

As can be noted, Equation (3.73) needs to be written in closed form before being solved. The terms on the RHS are not in closed form. They must be expressed as a function of moments or other known quantities in order to close the equation.

The method of moments are differentiated from each other by the way they handle the closure problem. Some of the methods assume that the PSD shape is known a-priori, e.g. Gaussian, lognormal, etc. Then, the equations of the moments yield equations for the assumed PSD parameters. Another way to proceed is to reconstruct the PSD from the lower order moments by interpolation polynomials or exponential function [58]. One of the most promising is the QMOM that was first proposed by McGraw [32] for studying aerosol evolution.

Quadrature Method of Moments (QMOM)

QMOM is based on the solution of the integrals involving the PSD $f(L; x, t)$ in terms of particle diameter L through a quadrature approximation :

$$f(L; , x, t) \equiv \sum_{j=1}^N w_j \delta(L - L_j) \quad (3.74)$$

which implies

$$m^{(k)}(x, t) = \int_0^{\infty} f(L; x, t) L^k dL \equiv \sum_{j=1}^N w_j L_j^k, \quad (3.75)$$

where abscissas L_j and weights w_j are calculated from the lower-order moments by Product-Difference (PD) algorithm [59] (see appendix C).

The method has been validated in the case of molecular growth and aggregation through comparison with analytical solutions and Monte Carlo simulations [60] and compared with other available approaches, such as Laguerre quadrature approximation and the finite element method, for the solution of the aerosol general dynamic equation [61]. Moreover, lately the QMOM has been extended to the description of bivariate population balance [62, 63], where the PSD is written in terms of more than one internal coordinate (e.g. particle volume and solute concentration). The length based spatially homogeneous PBE (see appendix B) can be written as

$$\frac{\partial f'(L, t)}{\partial t} + \frac{\partial}{\partial L}(G(L, t)f'(L, t)) = B_a(L; t) - D_a(L; t) + B_b(L; t) - D_b(L; t), \quad (3.76)$$

where

$$\begin{aligned} D_a(L; t) &= f(L, t) \int_0^{\infty} a(L, L') f(L', t) dL' \\ B_a(L; t) &= \frac{L^2}{2} \int_0^L \frac{a((L^3 - L'^3)^{1/3}, L')}{(L^3 - L'^3)^{2/3}} f((L^3 - L'^3)^{2/3}; t) f(L', t) dL' \\ B_b(L; t) &= \int_L^{\infty} b(L) \beta(L | L') f(L', t) dL' \\ D_b(L; t) &= b(L) f(L; t). \end{aligned}$$

Multiplying Equation (3.76) by L^k and then integrate from 0 to ∞ , we get

$$\frac{\partial m^k(t)}{\partial t} = \overline{B}_a(L; t) - \overline{D}_a(L; t) + \overline{B}_b(L; t) - \overline{D}_b(L; t), \quad (3.77)$$

where

$$\begin{aligned} \overline{B}_a(L; t) &= \frac{1}{2} \int_0^{\infty} f(L', t) \int_0^{\infty} a(L', L'') (L' + L'')^{k/3} f(L'', t) dL' dL'' \\ \overline{D}_a(L; t) &= \int_0^{\infty} L^k f(L, t) \int_0^{\infty} a(L, L') f(L', t) dL' dL \end{aligned}$$

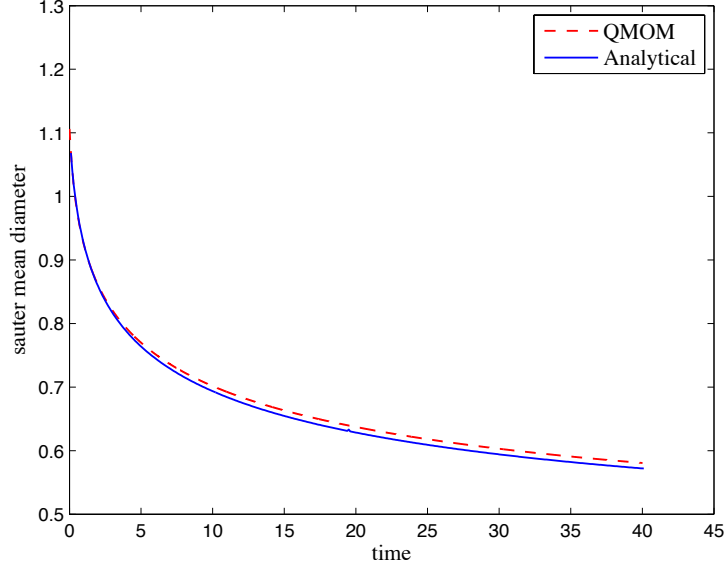


Figure 3.3: The sauter mean diameter for the breakage only.

$$\begin{aligned}\overline{B}_b(L; t) &= \int_0^\infty L^k \int_0^\infty b(L') \beta(L | L') f(L', t) dL' dL \\ \overline{D}_b(L; t) &= \int_0^\infty L^k b(L) f(L, t) dL.\end{aligned}$$

When the QMOM is used, all the integral terms included in the above equations are calculated through a quadrature approximation leading to

$$\begin{aligned}\frac{\partial m^k(t)}{\partial t} &= \frac{1}{2} \sum_{i=1}^N w_i \sum_{j=1}^N w_j (L_i^3 + L_j^3)^{k/3} a_{ij} + \sum_{i=1}^N b_i \overline{\beta}_i^{(k)} w_i \\ &\quad - \sum_{i=1}^N L_i^k w_i \sum_{j=1}^N w_j a_{ij} - \sum_{i=1}^N L_i^k b_i w_i,\end{aligned}\quad (3.78)$$

where $a_{ij} = a(L_i, L_j)$, $b_i = b(L_i)$ and $\overline{\beta}_i^{(k)} = \int_0^\infty L^k \beta(L | L_i) dL$. The number of nodes N used in the quadrature approximation determines the number of moments to be tracked. In fact, in order to calculate a quadrature approximation of order N , the first $2N$ moments have to be calculated. The QMOM is found very efficient from accuracy and computational cost point of view as we can see very good agreement between the solution by QMOM and analytical solution in Figures 3.3, 3.4. But QMOM has some drawbacks like

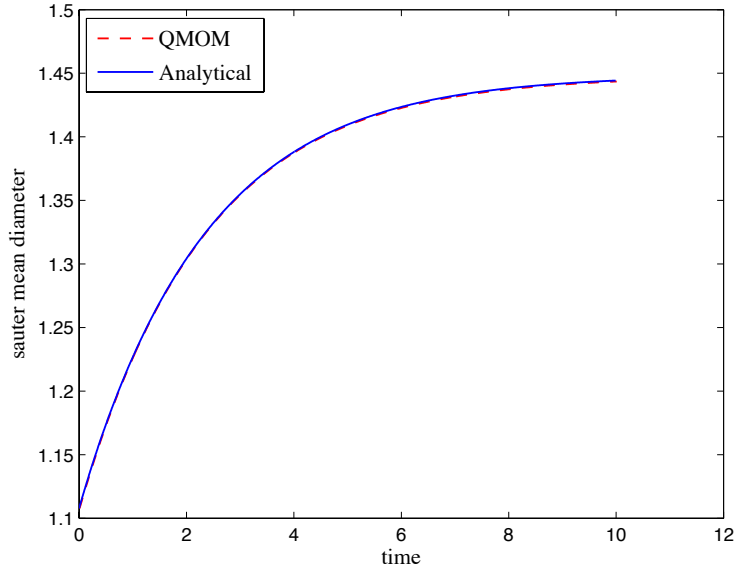


Figure 3.4: The sauter mean diameter for the breakage and aggregation both.

destroying the shape of the distribution and retaining the information about it only through that stored in the moments. The other drawback of QMOM appears in the solution of the abscissas and weights used in this quadrature which requires the solution of an eigenvalue problem in terms of the population low-order moments as one has to invert the system (3.75) by using product difference algorithm (see appendix C). These eigenvalues are roots of a polynomial equation resulting from the approximation of the number density function by a polynomial of a specified degree that equals the desired number of low-order moments [64]. Unfortunately as the number of the low-order moments increases, the solution of the associated eigenvalue problem become difficult due to ill-conditioning. Or equivalently, if the weights and abscissas are tracked directly [65] the solution of the resulting linear system becomes ill-conditioned and hence difficult to solve with sufficient accuracy.

Parallel Parent and Daughter Classes (PPDC)

Bove [66] introduced PPDC after QMOM to solve PBE. According Bove, it is possible to split the PBE based on the specific process as it is shown below.

The expanded PSD function can be written as

$$\begin{aligned}
f_E(v, t) &= \sum_{i=1}^M N_i(t) \delta(v - x_i) \\
&+ \sum_{i=1}^M \sum_{j=1}^M A_{ij}(t) \delta(v - y_{ij}) \\
&+ \sum_{i=1}^M \sum_{k=1}^{NB(i)} B_k^{(i)}(t) \delta(v - z_k^{(i)}) \\
&= f_p(v, t) + \sum_{i=1}^M \sum_{j=1}^M f_a^{ij}(v, t) + \sum_{i=1}^M f_b^{(i)}(v, t). \tag{3.79}
\end{aligned}$$

Considering the expanded PSD function, PBE can be written as

$$\begin{aligned}
\frac{\partial f_p(v, t)}{\partial t} + \sum_{i=1}^M \sum_{j=1}^M \frac{\partial f_a^{(ij)}(v, t)}{\partial t} + \sum_{i=1}^M \frac{\partial f_b^{(i)}(v, t)}{\partial t} \\
= S_{B,a}(f(v, t); v, t) + S_{D,a}(f(v, t); v, t) \\
+ S_{B,b}(f(v, t); v, t) + S_{D,b}(f(v, t); v, t). \tag{3.80}
\end{aligned}$$

On the LHS, the first term represents the change of the PSD of the parent classes, the second term represents the change of the PSD of coalescence daughter classes and the third term represents the change of the PSD of the breakage daughter classes.

Then, above equation can be split as follows :

$$\frac{\partial f_p(v, t)}{\partial t} = S_{D,a}(f(v, t); v, t) + S_{D,b}(f(v, t); v, t) \tag{3.81}$$

$$\sum_{i=1}^M \sum_{j=1}^M \frac{\partial f_a^{(ij)}(v, t)}{\partial t} = S_{B,a}(f(v, t); v, t) \tag{3.82}$$

$$\sum_{i=1}^M \frac{\partial f_b^{(i)}(v, t)}{\partial t} = +S_{B,b}(f(v, t); v, t). \tag{3.83}$$

Integrating Equations (3.81)-(3.83) over the range $[0, \infty)$, which is equivalent to discretize the equations in the internal coordinate domain, yields

$$\sum_{i=1}^M \frac{\partial N_i(t)}{\partial t} = - \sum_{i=1}^M N_i(t) \sum_{j=1}^M a(v_i, v_j) N_j(t) - \sum_{i=1}^M b(v_i) N_i(t) \quad (3.84)$$

$$\sum_{i=1}^M \sum_{j=i}^M \frac{\partial A_{ij}(t)}{\partial t} = \frac{1}{2} \sum_{i=1}^M \sum_{j=1}^M a(v_i, v_j) N_i(t) N_j(t) \quad (3.85)$$

$$\sum_{i=1}^M \sum_{k=1}^{NB(i)} \frac{\partial B_k^{(i)}(t)}{\partial t} = \sum_{i=1}^M \sum_{j=1}^M \gamma(v_j) b(v_j) N_j(t) \int_{v_i}^{v_{i+1}} \beta(v|x_j) dv. \quad (3.86)$$

In the particular framework with parallel process based grids and explicit discretization in time. Equations (3.84)-(3.86) can be split as follows :

$$\frac{\partial N_i(t)}{\partial t} = -N_i(t) \sum_{j=1}^M a(v_i, v_j) N_j(t) - b(v_i) N_i(t) \quad (3.87)$$

$$i = 1, \dots, M,$$

$$\frac{\partial A_{ij}(t)}{\partial t} = (1 - \frac{1}{2} \delta_{ij}) a(v_i, v_j) N_i(t) N_j(t) \quad (3.88)$$

$$i, j = 1, \dots, M, \quad j \geq i,$$

$$\frac{\partial B_k^{(i)}(t)}{\partial t} = \gamma(v_i) b(v_i) N_i(t) \int_{v_k}^{v_{k+1}} \beta(v|x_j) dv \quad (3.89)$$

$$i = 1, \dots, M \quad k = 1, \dots, NB(i).$$

After solving the system of Equations (3.87)-(3.89), the expanded PSD function becomes available :

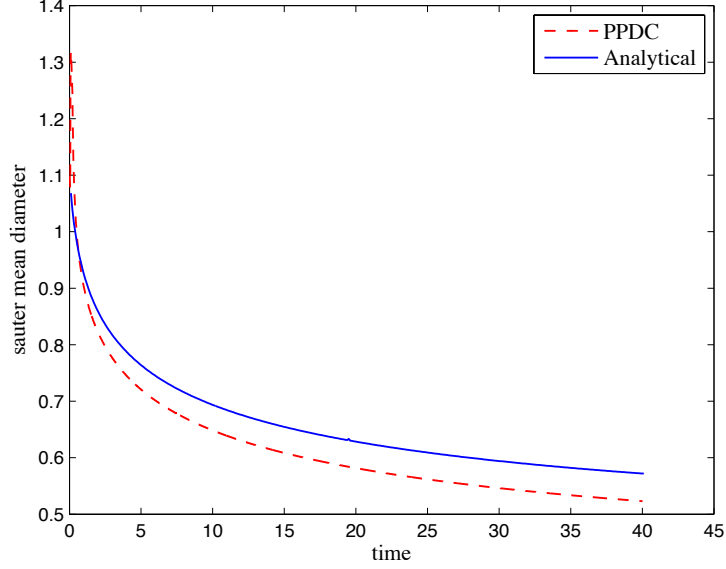


Figure 3.5: The sauter mean diameter for the breakage only.

$$\begin{aligned}
 f_E(v, t) &= f_p(v, t) + \sum_{i=1}^M \sum_{j=1}^M f_a^{ij}(v, t) + \sum_{i=1}^M f_b^{(i)}(v, t) \quad (3.90) \\
 &= \sum_{i=1}^M N_i(t) \delta(v - v_i) \\
 &\quad + \sum_{i=1}^M \sum_{j=i}^M A_{ij}(t) \delta(v - y_{ij}) \\
 &\quad + \sum_{i=1}^M \sum_{k=1}^{NB(i)} B_k^{(i)}(t) \delta(v - z_k^{(i)}).
 \end{aligned}$$

In order to work with the same number of parent classes for the next time step, the expanded PSD function should be reduced again to M Dirac's delta function

$$f_E(v, t) \equiv f_R(v, t) = \sum_{i=1}^M \tilde{N}_i \delta(v - \tilde{x}_i) \quad (3.91)$$

and imposing the equivalence of $2M$ properties for both the distributions, it yields a system of $2M$ non-linear equations in the unknowns \tilde{N}_i and \tilde{x}_i .

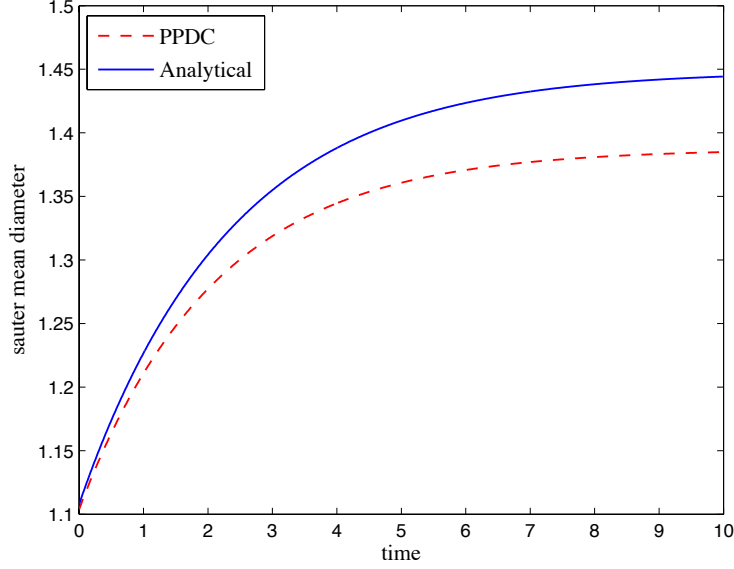


Figure 3.6: The sauter mean diameter for the breakage and aggregation both.

If the first $2M$ lower order moments are the chosen properties, the system of equations can be written as follows :

$$\sum_{i=1}^M \tilde{N}_i \tilde{x}_i^k = m_E^k(t) \quad k = 0, \dots, 2M - 1. \quad (3.92)$$

The inversion of the above non-linear system will give the weights and the abscissas of the reduced PSD which will be used as start up conditions for the next time step solution.

In Figures 3.5,3.6 show the comparison of the sauter mean diameter which solved by PPDC and analytically for the aforementioned cases 1 and 2. As we find that to get more accurate solution, one has to increase the number of classes which increases the complexity and time of computation.

Sectional Quadrature Method of Moments (SQMOM)

Attarakih [22] introduced the idea of SQMOM. In the finite difference or sectional methods the particle size (here it is denoted by the particle diameter d) is discretized into finite number of sections N_{pp} . The population in

each section is considered to behave like a single particle, and hence it is concentrated at a representative size usually at the middle of the section. In SQMOM, this single particle is called the primary particle and it is responsible for the reconstruction of the distribution. Unfortunately, the large number of primary particles in the classical sectional methods is required, not only to reconstruct the shape of distribution, but also to estimate the desired integral quantities associated with the distribution (such as the total number of particles and the mean particle size). This in turn increase the computational loads extensively when the population balance equation is coupled.

The interaction between primary particles in different sections, due to breakage or/and coalescence events for example, results in a new primary particle with no representative size due to the discrete approximation of the distribution. Because the newly-birtherd particle could not conserve any of its low order moments but one (if it is located at the middle of the section), the rest of the low-order moments are predicted with low accuracy and hence the associated integral quantities. To overcome this fundamental problem of the sectional methods, N_{sp} secondary particles are generated in each section with positions (abscissas) that are given by: $d_i^{(j)} : j = 1, 2, \dots, N_{sp}, i = 1, 2, \dots, N_{pp}$. The classical quadrature method of moments as introduced by McGraw [32] treats the population as a whole quantity without paying attention to any local variation of the density function between the limits of integration $(0, \infty)$. This is because the first use of the QMOM was done by Gordon [59] who was interested only in integrating functions over the domain: $(0, \infty)$. The only restriction that Gordon placed on the distribution function is that $F(d, t)$ (the commulative distribution of $f(d, t)$ is a non decreasing function and the values of its first $2N_{sp}$) moments exist.

The idea behind the SQMOM is to devide the PDF (praobability density function) into sections followed by the application of the QMOM to each section. It is clear to this point that any section of $F(d, t)$ will remain non decreasing even when $f(d, t)$ vanishes in certain sections. In the special case where $f(d, t) = 0$ (especially at the two ends of the distribution due to regulatory conditions [67]), the PDF is uniformly distributed and hence the positions of the secondary particles could be set arbitrarily. So, there is no need to use the QMOM for the special case. It is obvious that by applying the QMOM to certain sections of the population, the rules of Gordon [59] were not violated. This in fact allows the application of the classical QMOM to any arbitrary section of the population resulting in a set of local particle

positions (abscissas) and weights. To this end it remains how to relate the positions and weights of the secondary particles in the i th section to the sectional moments of the unknown function $f(d, t)$.

These operations of averaging are carried out for all primary particles as follows :

$$\tilde{w}_i(t) = \frac{1}{\Delta d_i} \sum_{j=1}^{N_{sp}} w_j^{(i)}, \quad i = 1, 2, \dots, N_{pp} \quad (3.93)$$

$$\tilde{d}_i(t) = \frac{\sum_{j=1}^{N_{sp}} w_j^{(i)} d_j^{(i)}}{\sum_{j=1}^{N_{sp}} w_j^{(i)}}, \quad i = 1, 2, \dots, N_{pp}. \quad (3.94)$$

In pure mathematical sense, the above presentation is equivalent to applying the QMOM to each section of an arbitrary width : $[d_{i-1/2}, d_{i+1/2}]$: $i = 1, 2, \dots, N_{pp}$ resulting in a set of sectional moments that could be written as :

$$m_k^{(i)}(t) = \int_{d_{i-1/2}}^{d_{i+1/2}} d^k f(d, t) \partial d, \quad k = 0, 2, \dots, 2N_{sp} - 1. \quad (3.95)$$

Now, let the population density in the i th section ($[d_{i-1/2}, d_{i+1/2}]$: $i = 1, 2, \dots, N_{pp}$) be represented in terms of local secondary particles weights and positions in the following form :

$$f^{(i)}(d, t) = \sum_{j=1}^{N_{sp}} w_j^{(i)}(t) \delta(d - d_j^{(i)}), \quad (3.96)$$

where $\delta(d - d_j^{(i)})$ is the Dirac Delta function placed at the secondary particle position: $d_j^{(i)}$ with strength $w_j^{(i)}$. Similarly, the whole population density could now be reconstructed using the same form of above equation. But now making use of the mean weights and positions assigned to the primary particles given by Equations (3.93) and (3.94), we have

$$f(d, t) = \sum_{i=1}^{N_{sp}} \tilde{w}_i(t) \delta(d - \tilde{d}_i(t)). \quad (3.97)$$

By making use of above equation, we get the sectional moments as

$$m_k^{(i)}(t) = \sum_{j=1}^{N_{sp}} w_j^{(i)} (d_j^{(i)})^k, \quad r = 0, 2, \dots, 2N_{sp} - 1. \quad (3.98)$$

The discretization of the general PBE is performed by partitioning the particle size (diameter) into contiguous sections of an arbitrary width $[d_{i-1/2}, d_{i+1/2}]$: $i = 1, 2, \dots, N_{pp}$. By multiplying the both sides of PBE (3.76) by d^k and integrating with respect to d over the section width $[d_{i-1/2}, d_{i+1/2}]$: $i = 1, 2, \dots, N_{pp}$, the transformed equations could be written as:

$$\begin{aligned} \frac{\partial m_k^{(i)}(t)}{\partial t} = & -D_k^{(i)} [\Gamma^{(i)} \cdot w^{(i)}]^T + \sum_{p=i}^{N_{pp}} C_k^{(i,p)} [\Gamma^{(i)} \cdot w^{(i)}]^T \\ & + \sum_{r=1}^{i \times N_{sp}} \left\{ \sum_{j=r}^{i \times N_{sp}} \Psi_{r,j,k}^{(i)} a_{j,r} w'_j w'_r - \eta_k \sum_{n=1}^{N_{sp} \times N_{pp}} (d_r)^k a_{r,n} w'_r w'_n \right\} \end{aligned} \quad (3.99)$$

Where,

$$\begin{aligned} \eta_r &= \begin{cases} 1 & \text{if } (i-1)N_{sp} + 1 \leq r \leq iN_{sp} \\ 0 & \text{otherwise} \end{cases} \\ \Psi_{r,j,k}^{(i)} &= \begin{cases} (1 - \frac{1}{2}\delta_{r,j}) & \text{if } (d_{i-1/2})^3 \leq [(d'_r)^3 + (d'_j)^3] \frac{k}{3} < (d_{i+1/2})^3 \\ 0 & \text{otherwise} \end{cases} \\ C^{(i,p)} &= \begin{bmatrix} \pi_{0,1}^{(i,p)} & \dots & \pi_{0,N_{sp}}^{(i,p)} \\ \dots & \dots & \dots \\ \vdots & \vdots & \vdots \\ \pi_{2N_{sp}-1,1}^{(i,p)} & \dots & \pi_{2N_{sp}-1,N_{sp}}^{(i,p)} \end{bmatrix} \\ \pi_{k,j}^{(i,p)} &= \int_{d_{i-1/2}}^{\min(d_{i+1/2}, d_j^{(p)})} d^r \beta(d|d_j^{(p)}) \partial d \quad (3.100) \\ D_k^{(i)} &= [(d_1^{(i)})^k \quad (d_2^{(i)})^k \quad \dots \quad (d_{N_{sp}}^{(i)})^k] \\ w^{(i)} &= [w_1^{(i)} \quad w_2^{(i)} \quad \dots \quad w_{N_{sp}}^{(i)}] \\ \Gamma^{(i)} &= [\Gamma(d_1^{(i)}) \quad \gamma(d_2^{(i)}) \quad \dots \quad \Gamma(d_{N_{sp}}^{(i)})] \\ d' &= [d_1^{(1)} \quad \dots \quad d_{N_{sp}}^{(1)} \quad \dots \quad d_1^{(N_{pp})} \quad \dots \quad d_{N_{sp}}^{(N_{pp})}] \\ w' &= [w_1^{(1)} \quad \dots \quad w_{N_{sp}}^{(1)} \quad \dots \quad w_1^{(N_{pp})} \quad \dots \quad w_{N_{sp}}^{(N_{pp})}] \\ k &= 0, 1, \dots, 2N_{sp} - 1, \quad i = 1, 2, \dots, N_{pp}. \end{aligned}$$

The integral appearing in Equation (3.100) preserves the low-order moments

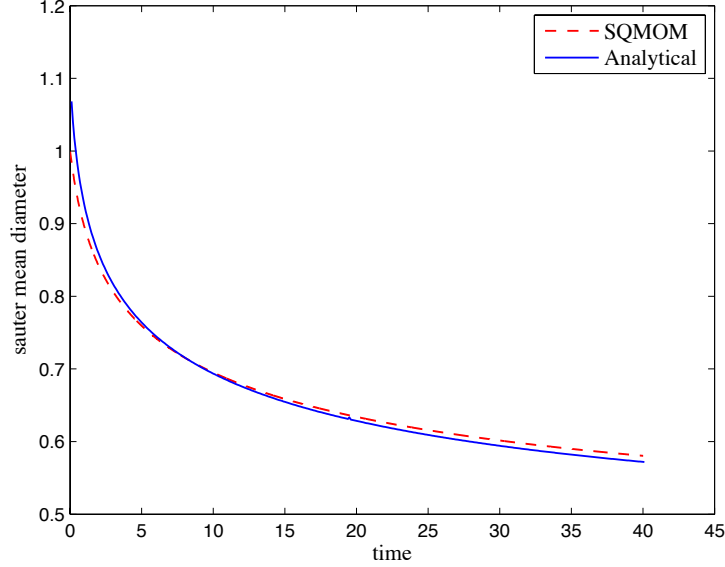


Figure 3.7: The sauter mean diameter for the breakage only.

of the newly birthed particles in the i^{th} section due to splitting of a mother particle of size $d_j^{(p)}$. This integral could be easily evaluated if the form of the daughter particle distribution ($\beta(d|d_j^{(p)})$) is known. The function (η_k) is used to select the secondary particles disappearing due to aggregation in the i^{th} section, while $\Psi_{r,j,k}^{(i)}$ is a sparse aggregation matrix whose nonzero elements represent the successful aggregation events between any pairs of secondary particle with locations and weights that are given by the augmented vectors : d' and w' . It is clear that the solution of the discretized PBE guarantees the exact preservation of $2N_{sp}$ first low order moments ($m_k : k = 0, 1, \dots, 2N_{sp} - 1$).

In Figures 3.7, 3.8, the sauter mean diameter as predicted using the SQMOM ($N_{pp} = 2, N_{sp} = 2$) is compared with the analytical solution for the aforementioned cases. It is clear that using 2 primary particles is enough to predict the sauter mean diameter very accurately. Figure 3.9 shows the comparison of the sauter mean diameter as predicted using the SQMOM with different combination of number of primary particles and number of secondary particles for case 2. It is clear that 2 primary particles and 2 secondary particles

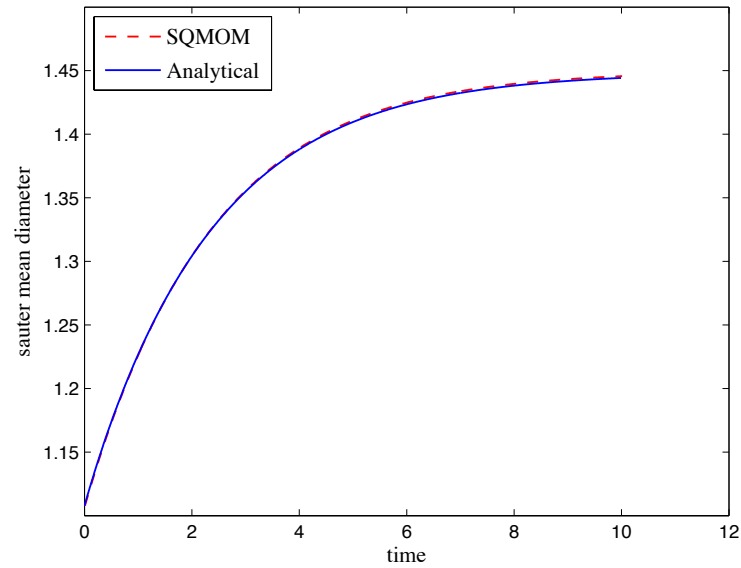


Figure 3.8: The sauter mean diameter for both the breakage and aggregation.

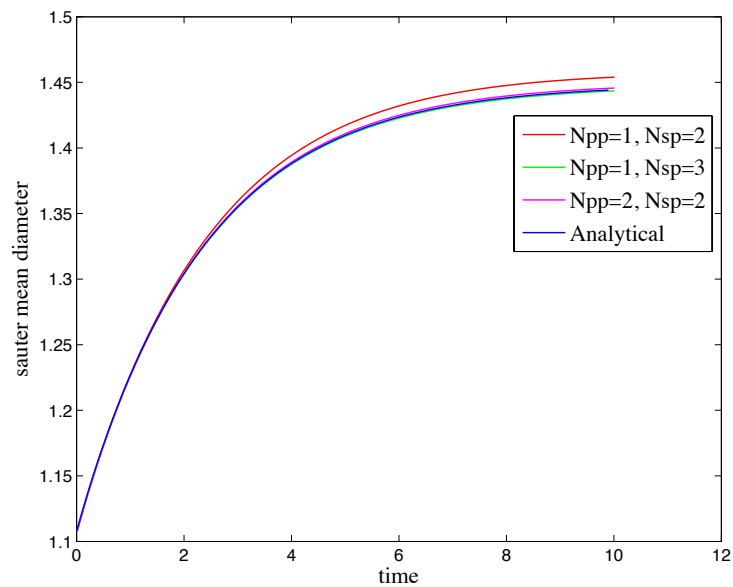


Figure 3.9: The comparison of the sauter mean diameter for both the breakage and aggregation for different number of primary and secondary particles.

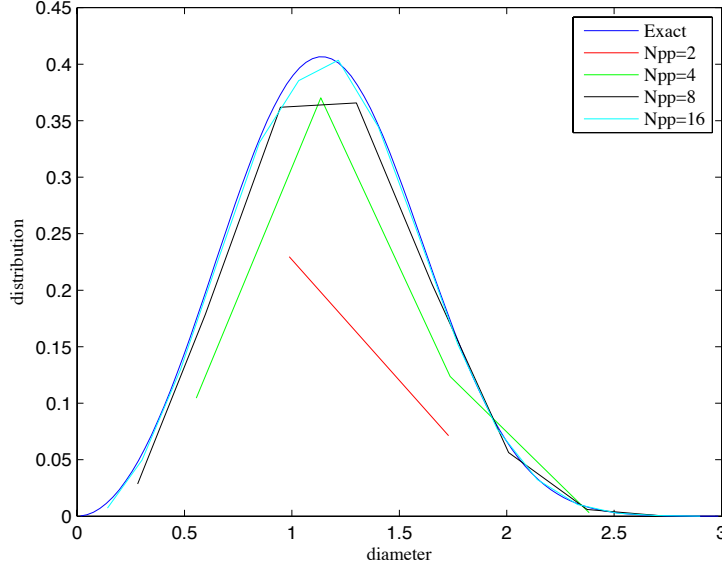


Figure 3.10: Average number concentration using different primary particles as predicted by the SQMOM.

predictions are same as those of 1 primary particle and 3 secondary particles (which is equivalent to QMOM with 3 quadratures). Figure 3.10 shows the comparison of average number concentration using different primary particles as predicted by the SQMOM with the analytical solution for case (2). It is clear that 16 primary particles are enough to reconstruct the distribution or predict the average number concentration accurately.

Multi Primary and One secondary Particle Method (MPOSPM)

Note that when we take one secondary particle only then SQMOM becomes a Multi Primary and One Secondary Particle Method (MPOSPM). In this case we need to evaluate only 2 moments (zeroth and third) and we evaluate average diameter by following formula :

$$d_{30} = \left(\frac{6 m_0}{\pi m_3} \right)^{1/3} . \quad (3.101)$$

In Figure 3.1, the average diameter as predicted using MPOSPM is compared with the analytical solution for case 1. In case 1, the breakage kernel is non-linear ($0.1d^6$) in the size so to accurately predict the average diameter, we

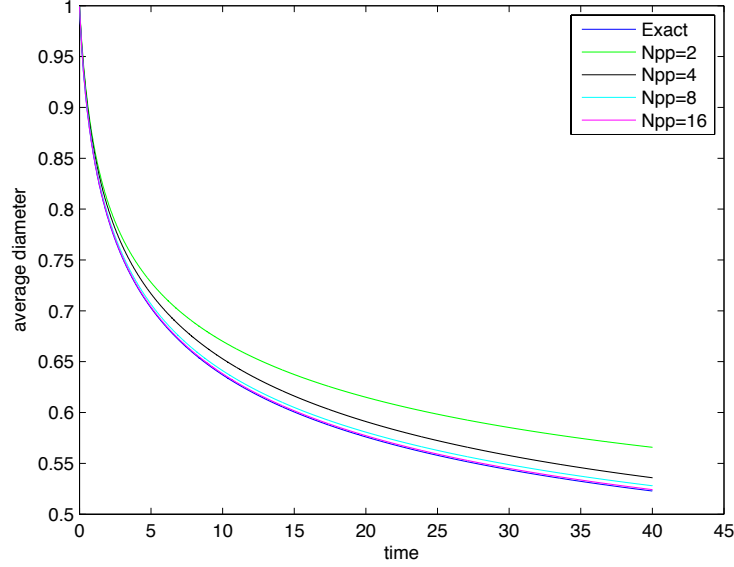


Figure 3.11: The sauter mean diameter for the breakage only.

have to increase the number of primary particles and find that 16 primary particles are enough to predict the average diameter very accurately.

One Primary and One Secondary Particle Method (OOSPM)

When we restrict the number of primary particles and the number of secondary particles to one, a one primary and one secondary particle method (OOSPM) results, whereby the number density function can be written as

$$f(d, t) = N\delta(d - d_{30}).$$

The one primary and one secondary particle method is the simplest discrete method that can reduce the continuous population balance equation. This representation is of moderate accuracy and reflects all the features contained in the continuous population balance equation. For example, the method conserves both total number and volume (mass) concentrations and is exact when the breakage and coalescence frequencies are constants. This corresponds to tracking directly the total number concentration (N), volume fraction (α_d) and the solute concentration ($\overline{C_d}$) by solving their transport equations. To derive these equations, the bivariate density function is con-

sidered as Dirac delta function with weight (N) and locations (d_{30} and \overline{C}_d):

$$n_{d,C_d}(d, C_d; t, z) = N(t, z)\delta(d - d_{30}(t, z))\delta(C - \overline{C}_d(t, z)). \quad (3.102)$$

This is equivalent to replacing the bivariate density function by one primary and one secondary particle (in the special case they are identical) with weight (N) and internal states (d_{30} : mean diameter and \overline{C}_d : mean solute concentration).

We have validated the OPOSPM for the aforementioned two cases and for the following three more cases :

Case 3: Aggregation in a batch vessel with product aggregation frequency.

Case 4: Splitting and aggregation in a batch vessel with linear splitting and sum aggregation frequencies.

Case 5: Splitting and aggregation in a batch vessel with linear splitting and product aggregation frequencies.

We have evaluated the analytical solution for cases 3,4 and 5 and are presented in the previous subsection 3.2.1.

Figures 3.12,3.13 compares the predicted average diameter by using OPOSPM and analytical solution for cases (1 and 2) which shows good agreement between both solutions. Figure 3.14 compares the average number density as predicted by the OPOSPM and the analytical solution which shows that OPOSPM predicts quite accurately the average number density for case (3). In Figures 3.15,3.17, the comparison between the analytical solution and predicted solutions using the OPOSPM are shown for cases (4 and 5) respectively. Figures 3.16,3.18 compares the average diameter as predicted by OPOSPM and analytical solution for cases (4 and 5). It is clear that OPOSPM is able to predict quite accurately the average number density and average diameter for all the cases.

Now, we deal with numerical experiments for the convergence analysis of the MPOSPM. We consider two cases only breakage in continuous vessel and aggregation and breakage both in the batch vessel.

Let us begin with the first case of a non-linear breakage kernel ($0.1 \times d^6$) in a continuous vessel. The numerical results are presented in Table 3.1. Which shows the convergence of second order.

Now we consider the second test case of non-linear breakage kernel ($0.1 \times d^6$) and non linear aggregation kernel ($d^6 \times d'^6$) in a batch vessel. The numerical results of the convergence analysis have been summarized in Table 3.2. Once again, as expected, in both cases, the MPOSPM approximately converges to

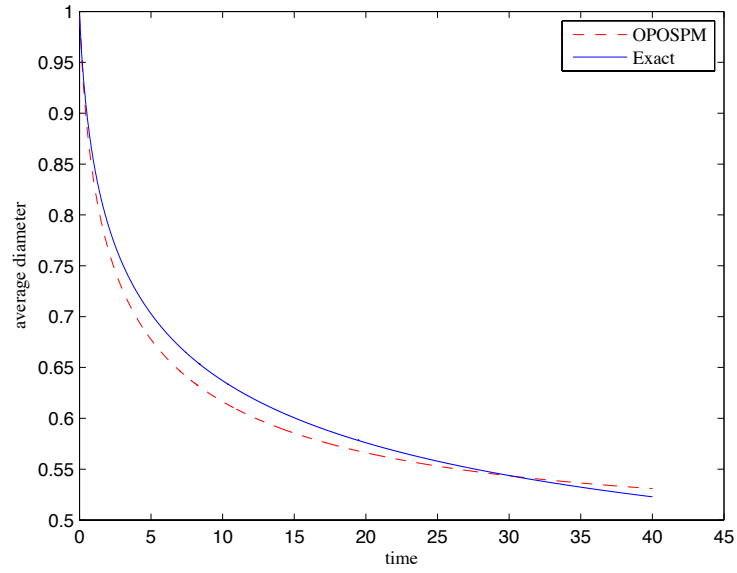


Figure 3.12: The sauter mean diameter for the breakage only.

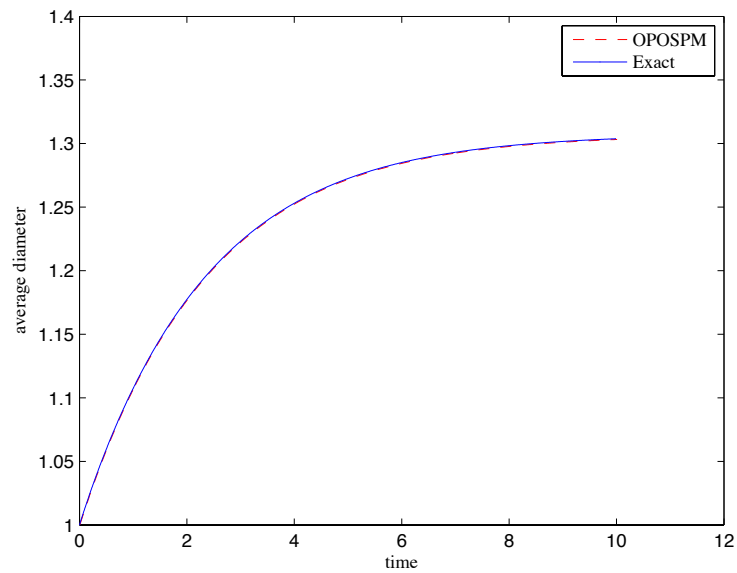


Figure 3.13: The sauter mean diameter for both the breakage and aggregation.

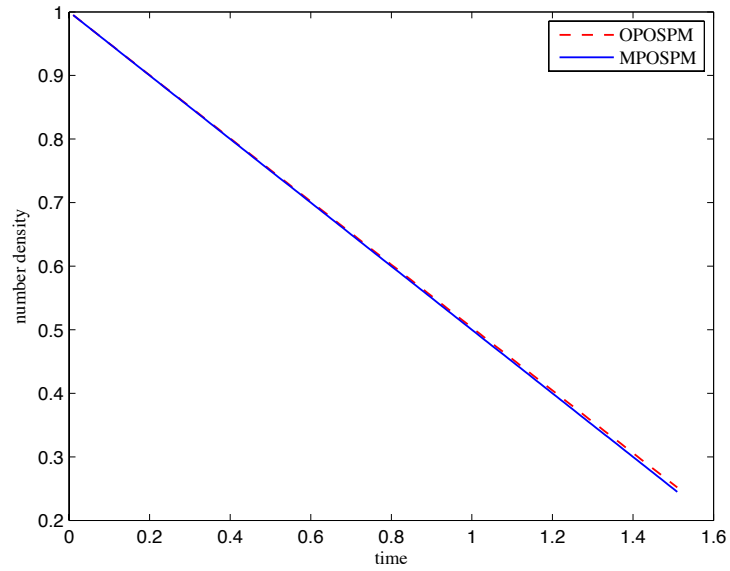


Figure 3.14: The number density for the product coalescence kernel.

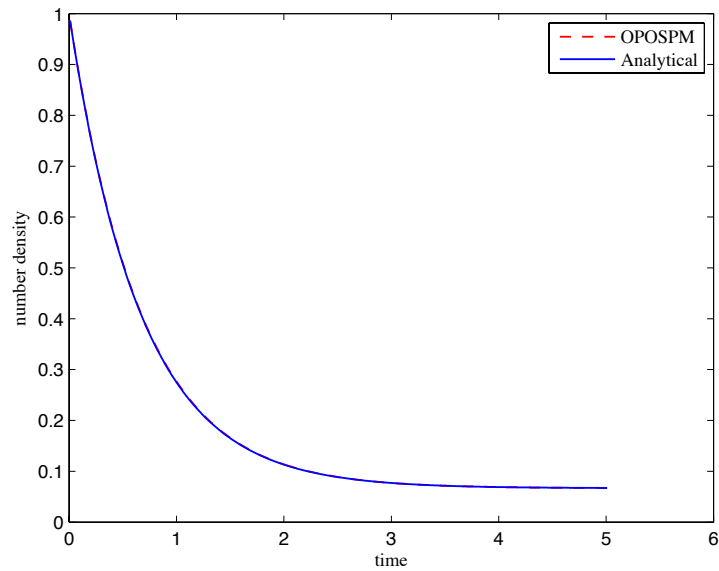


Figure 3.15: The number density for the additive coalescence kernel and linear breakage kernel.

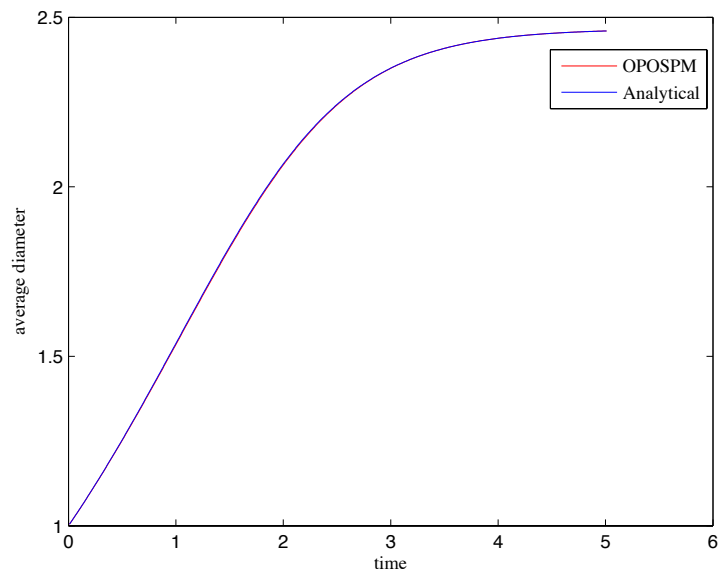


Figure 3.16: The average diameter for the additive coalescence kernel and linear breakage kernel.

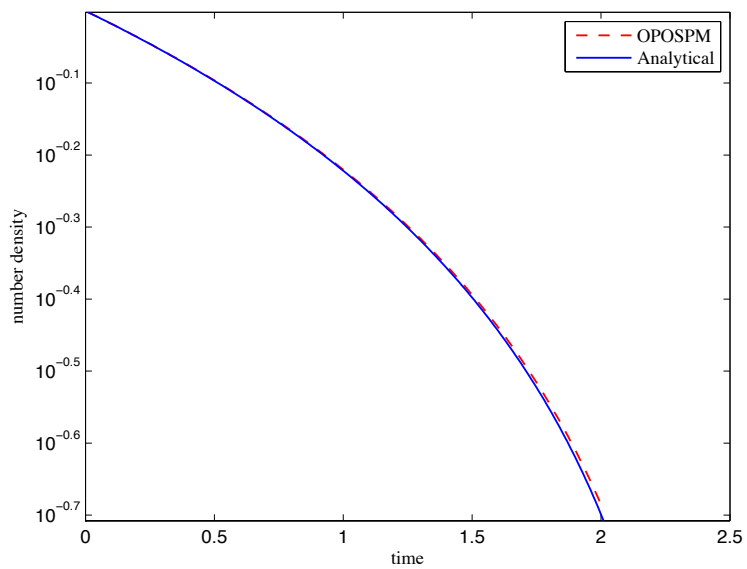


Figure 3.17: The number density for the productive coalescence kernel and linear breakage kernel.

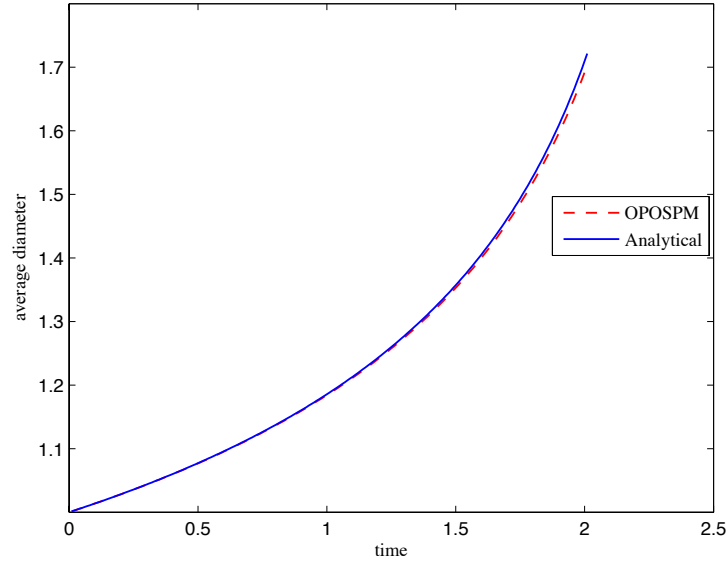


Figure 3.18: The average diameter for the productive coalescence kernel and linear breakage kernel.

second order.

Table 3.1: Error analysis of MPOSPM for the case of breakage only

N_{pp}	L^1 Error	EOC for L^1	L^2 Error	EOC for L^2
2	142.8219		2.3180	
4	56.4930	1.3381	0.9009	1.3635
8	18.0500	1.6461	0.2881	1.6445
16	4.8988	1.8815	0.0779	1.8869
32	1.3664	1.8442	0.0235	1.7292

3.2.3 Comparison of Numerical Methods

In this section, we compare the numerical methods in terms of accuracy, complexity and time of computation.

Tables 3.3,3.4 show the comparison among the methods for aforementioned

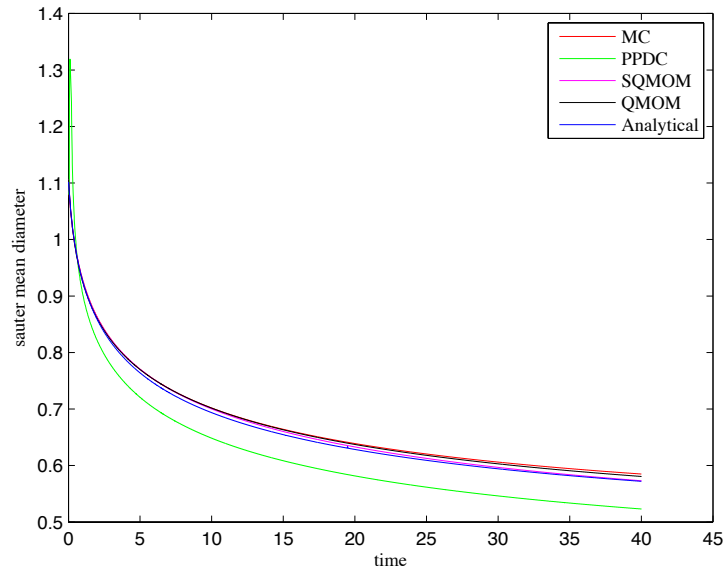


Figure 3.19: The sauter mean diameter for the breakage only.

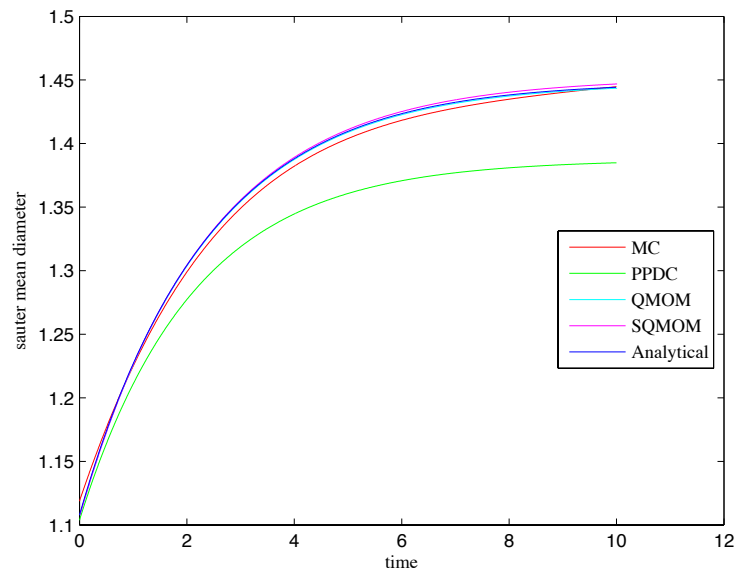


Figure 3.20: The sauter mean diameter for the aggregation and breakage both.

Table 3.2: Error analysis of MPOSPM for the case of both the breakage and aggregation

Npp	L1 Error	EOC for L1	L2 Error	EOC for L2
2				
4	62.341		2.2931	
8	23.9580	1.3800	0.7881	1.5408
16	61.586	1.9598	0.2031	1.9559
32	1.7659	1.8022	0.0575	1.8216
64	0.5423	1.7032	0.0175	1.7178

Table 3.3: Comparison of numerical methods to solve PBE for the case of breakage only

Methods	No. of Equations	Error	CPU Time (Sec)
MC	100	0.0129	15.5324
PPDC	8	0.0489	0.0765
QMOM	6	0.0086	0.0360
SQMOM	8	0.0009	0.0257

cases 1 and 2. It is clear that QMOM and SQMOM are comparably better in terms of accuracy and time of computation. As we know that in case 1, the breakage kernel is non-linear ($0.1 \times d^6$) in the volume of the droplets which creates some difficulty in predicting the diameter accurately. But, we can see in Table 3.3 that SQMOM predicts the sauter mean diameter quite accurately and takes minimum time to compute as compared to the other methods.

Table 3.4: Comparison of numerical methods to solve PBE for the case of breakage and aggregation both.

Methods	No. of Equations	Error	CPU Time (Sec)
MC	130	4.3425×10^{-4}	18.0220
PPDC	12	0.0594	0.0755
QMOM	6	7.4551×10^{-4}	0.0187
SQMOM	8	0.0026	0.0119

Chapter 4

Momentum Transfer Between Liquid-Liquid Phases

In this chapter, the solution of CFD-Monovariate PBE coupled model is discussed. We consider two phase (continuous and dispersed) and the momentum transfer between them. We begin with the two fluid model with only one primary particle, but later on we consider more primary particles and then take the average diameter for all primary particles. Finally the numerical results for the multi fluid model are shown whereby each primary particle is considered as a separate fluid. To solve the model we have used two solvers. First solver is OPOSPM and MPOSPM to simplify the PBE and then FPM solver to solve the model equations numerically.

4.1 FPM-OPOSPM Solver

First we reduce the model equations by using OPOSPM. When we apply OPOSPM on the PBE then we directly get two equations for the number concentration (N) and the volume concentration (α_d) of the droplets from the PBE and then we evaluate the average diameter of the droplets. After having the average diameter of the droplets we plug it in the momentum equation of droplets to calculate the velocity (u_d) of the droplets. To calculate the velocity of the continuous phase, we use the analytical formulation which we get after adding the conservation of mass equations of the continuous and dispersed phases (see appendix A). To evaluate the volume concentration of the continuous phase, we use the constraint $\alpha_c + \alpha_d = 1$. The model is simulated with the initial and boundary conditions given in Table (4.1) for

the column geometry shown in Table (4.2).

Table 4.1: Initial and inlet boundary conditions for the RDC liquid-liquid extraction columns.

Initial Conditions	Inlet boundary conditions
$N(z, t_0) = 0.0$	$N(z_d, t) = \frac{Q_d^{in}}{A_c v^{in}}$
$\alpha_d(z, t_0) = 0.0$	$\alpha_d(z_d, t) = \frac{Q_d^{in}}{A_C}$
$u_d(z, t_0) = 0.0$	$u_d(z_d, t) = \frac{d_s}{4.2} \left(\frac{g \Delta \rho}{\rho_c} \right)^{2/3} \left(\frac{\rho_c}{\mu_c} \right)^{1/3}$

Table 4.2: Column Geometry

Column diameter	0.15 m
Stator diameter	0.105 m
Rotor diameter	0.090 m
Compartment height	0.030 m
Column height	2.55 m
Dispersed phase inlet	0.250 m
Continuous phase inlet	2.250 m

4.1.1 The PBE without Source Term

First we solve the model by supposing that average diameter of droplets is fixed which means that the breakage kernel and aggregation kernels are zero. Figure 4.1 and 4.2 show the response of the total number concentration and volume concentration of the droplets at steady state respectively. It is clear that the number concentration and volume concentration of droplets decreases from its initial value to a terminal value as the particles accelerate from their initial velocity to their terminal velocity which is shown in Figure 4.3 because of this we can see a peak in Figures 4.1 and 4.2 at the inlet of dispersed phase. We can also conclude from Figures 4.1, 4.2 and 4.3 that the solutions for number density, volume concentration and velocity of droplets reach a steady state after $t = 20$ sec with time step 5×10^{-3} without breakage and aggregation kernels.

The velocity profile of the continuous phase is shown in Figure 4.4. It is

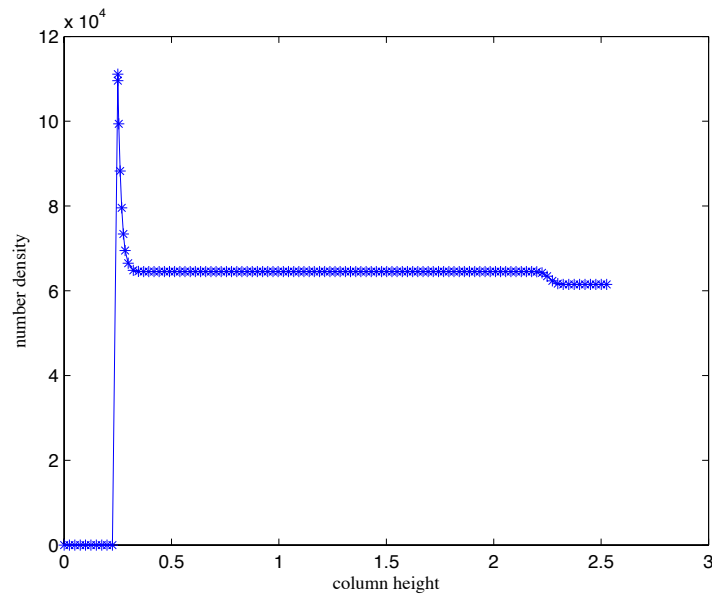


Figure 4.1: The number density of the droplets without breakage and coalescence kernels.

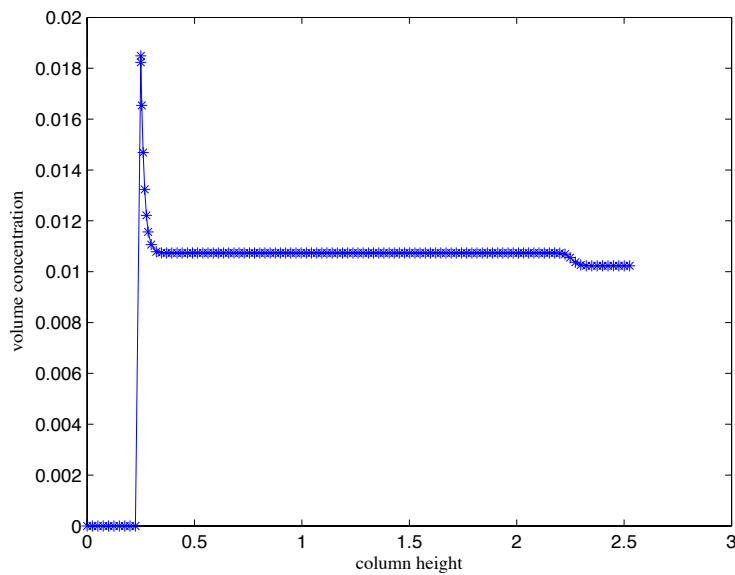


Figure 4.2: The volume concentration of the droplets without breakage and coalescence kernels.

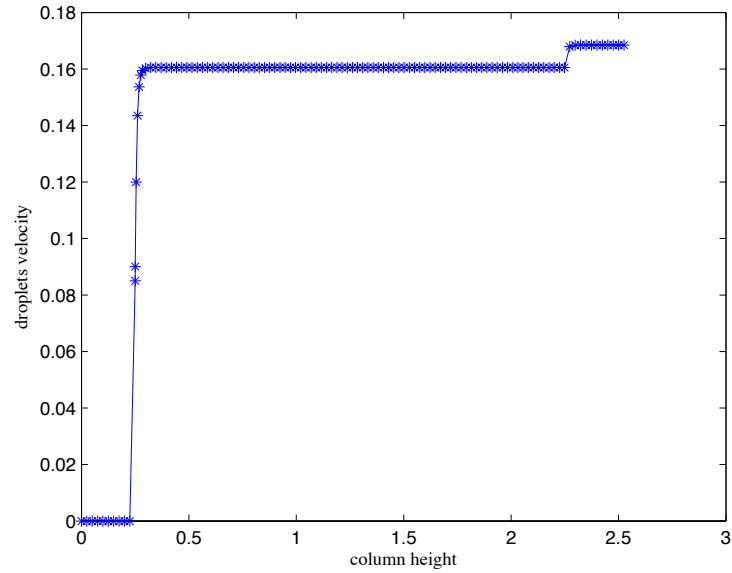


Figure 4.3: The average velocity of the droplets without breakage and coalescence kernels.

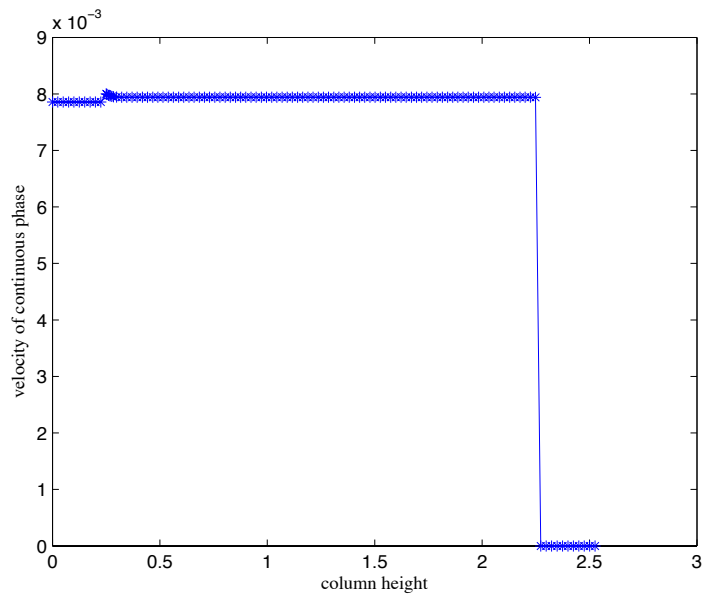


Figure 4.4: The velocity of the continuous phase without breakage and coalescence kernels.

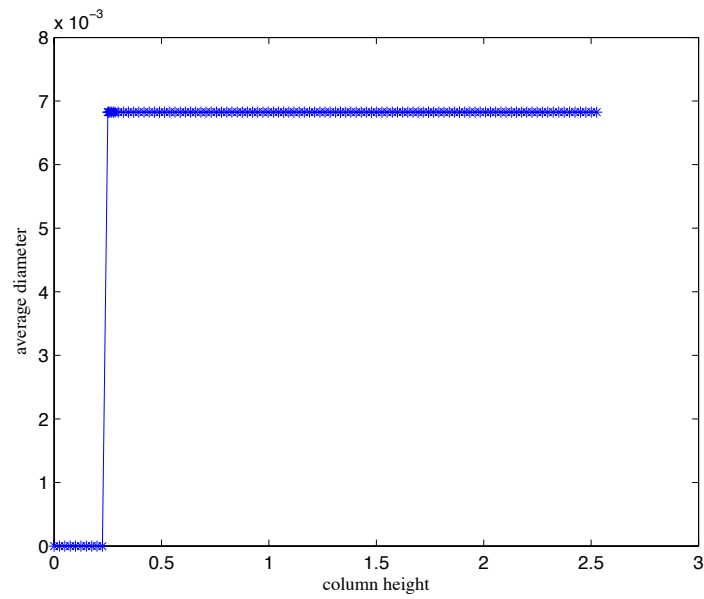


Figure 4.5: The average diameter of the droplets without breakage and coalescence kernels.

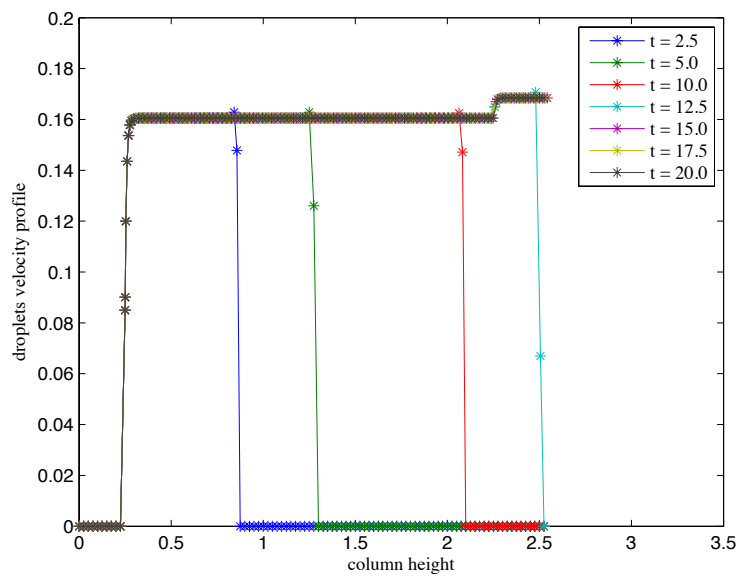


Figure 4.6: The droplets velocity profile on the different time frames.

Table 4.3: Physical Quantities

ρ_c	1000.0	kg/m^3
ρ_d	860.0	kg/m^3
μ_c	9.2×10^{-4}	$kg/m.s$
g	9.81	m/s^2
Q_d^{in}	2.77×10^{-5}	m^3/s
Q_c^{in}	1.38×10^{-4}	m^3/s
d^{in}	3.0	mm
d_{min}	0.001	mm
d_{max}	6.0	mm

clear from Figure 4.4 that the two spatial discontinuities at the inlets of dispersed phase and continuous phase are also correctly resolved. We can see the average diameter of droplets in Figure 4.5 which is constant through the whole column after the inlet of the dispersed phase; which was expected since the breakage kernel and aggregation kernel are zero.

Figure 4.6 shows the time history for the dispersed phase velocity. This figure clearly shows that for $t = 20$ we get a fairly good description of the two-phase flow inside the column.

4.1.2 The PBE with Source Term

In this section, the effect of non-zero source term is discussed. Initially, we show the effect of constant breakage and aggregation kernels and then non-constant kernels followed by real kernels.

Constant kernels

We have taken the constant breakage kernel 0.03 and coalescence kernel 10^{-6} to solve the model. Figures 4.7 and 4.8 show the number density and volume concentration of droplets. We can see from Figure 4.7 that the coalescence kernel is dominating as the number density is decreasing which is clear from Figure 4.10 too as the average diameter is increasing.

Figure 4.9 gives the velocity profiles of the dispersed phase. It shows that the velocity increases due to the increase of average diameter (Figure 4.10). This fact is reflected from the momentum equation, where drag force is the

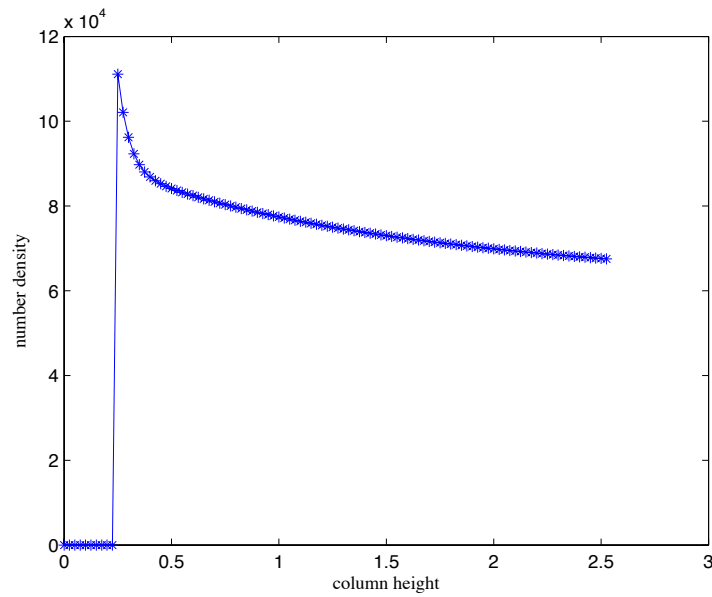


Figure 4.7: The number density of the droplets with constant breakage kernel 0.03 and coalescence kernel 10^{-6} .

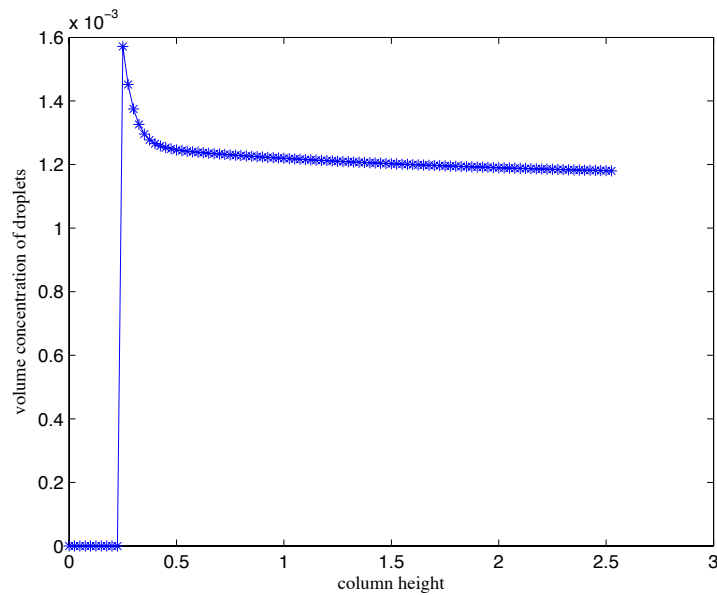


Figure 4.8: The volume concentration of the droplets with constant breakage kernel 0.03 and coalescence kernel 10^{-6} .

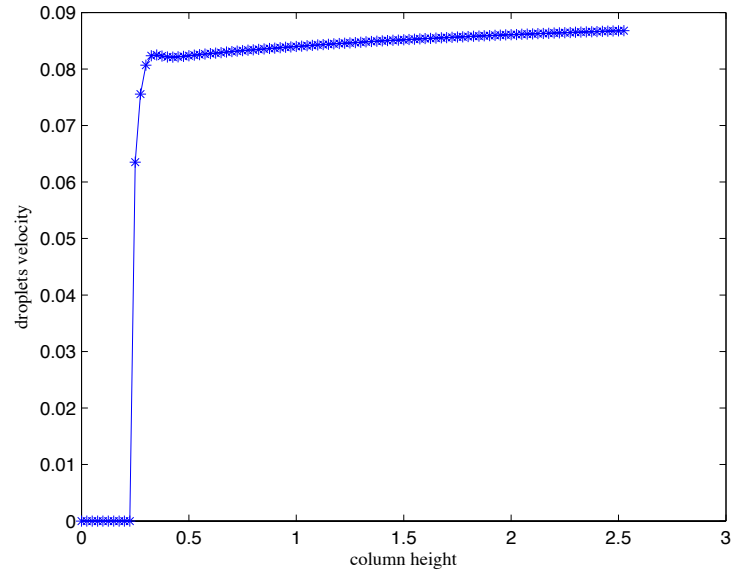


Figure 4.9: The average velocity of the droplets with constant breakage kernel 0.03 and coalescence kernel 10^{-6} .

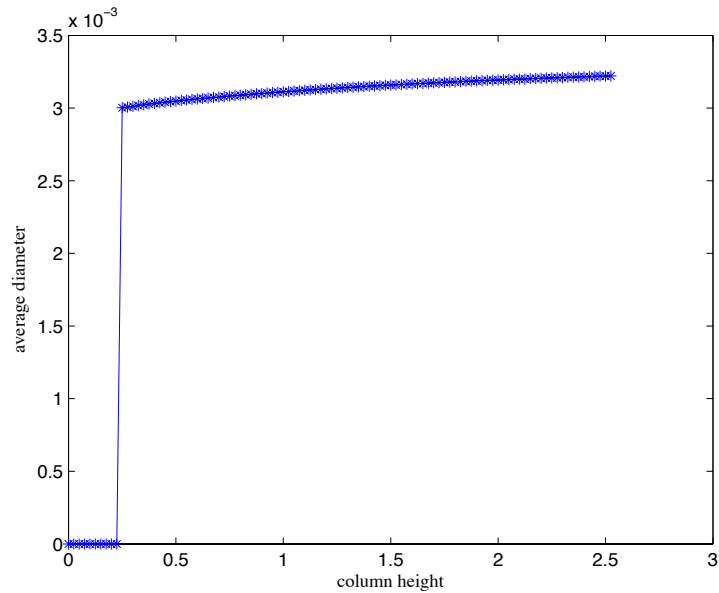


Figure 4.10: The average diameter of the droplets with constant breakage kernel 0.03 and coalescence kernel 10^{-6} .

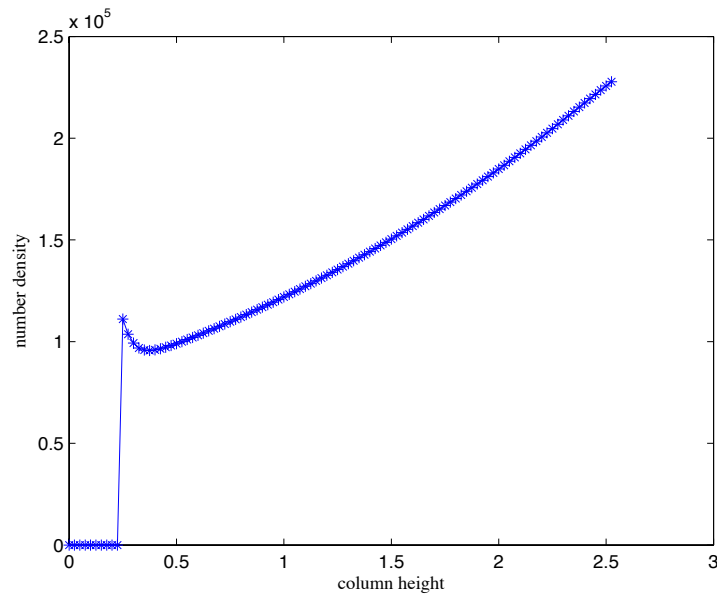


Figure 4.11: The number density of the droplets with constant breakage kernel 0.03 and coalescence kernel 10^{-7} .

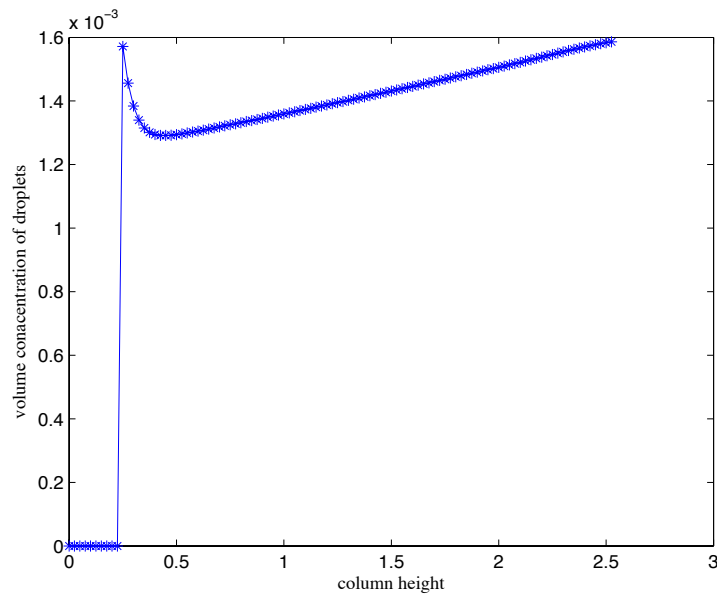


Figure 4.12: The volume concentration of the droplets with constant breakage kernel 0.03 and coalescence kernel 10^{-7} .

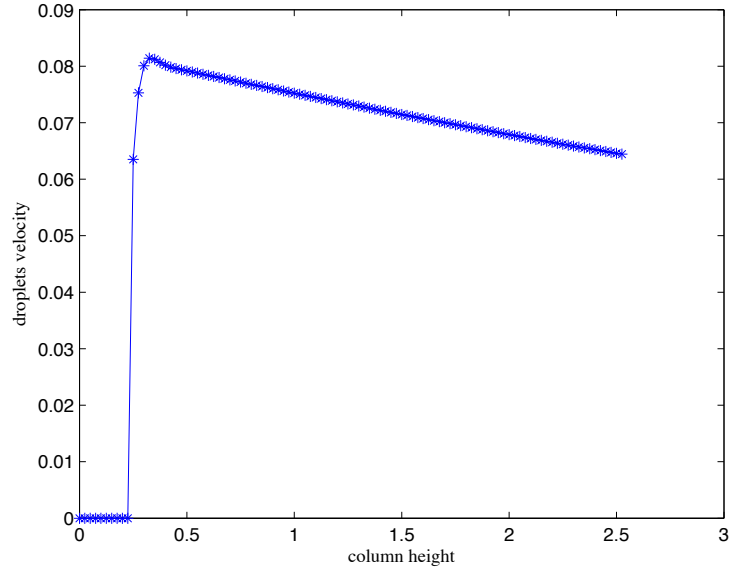


Figure 4.13: The average velocity of the droplets with constant breakage kernel 0.03 and coalescence kernel 10^{-7} .

function of average diameter. So when the average diameter increases then drag force decreases and as a result, the droplets velocity increases.

Now if we decrease the coalescence kernel from 10^{-6} to 10^{-7} and we find that the breakage kernel dominates resulting to increment of the number density, decrease of the droplets velocity as well as decrease of the average diameter which is clear from Figures 4.11, 4.13 and 4.14. Figure 4.12 depicts the volume concentrations of dispersed phase which decreases at the inlet of dispersed phase as particles accelerate from their initial velocity to terminal velocity (Figure 4.13). But after that the volume concentration of dispersed phase increases as droplet velocity decreases and spatial derivative of velocity becomes negative. This fact is reflected from the equation of volume concentration (i. e. continuity equation).

4.1.3 Non-Constant Breakage and Coalescence Kernels

In this section, the effect of non-constant breakage and coalescence kernels is discussed. We take the breakage kernel as $0.1 \times d^3$ and coalescence kernel as $d^3 + d'^3$ and see the physical quantities of fluid. In this case, we find that

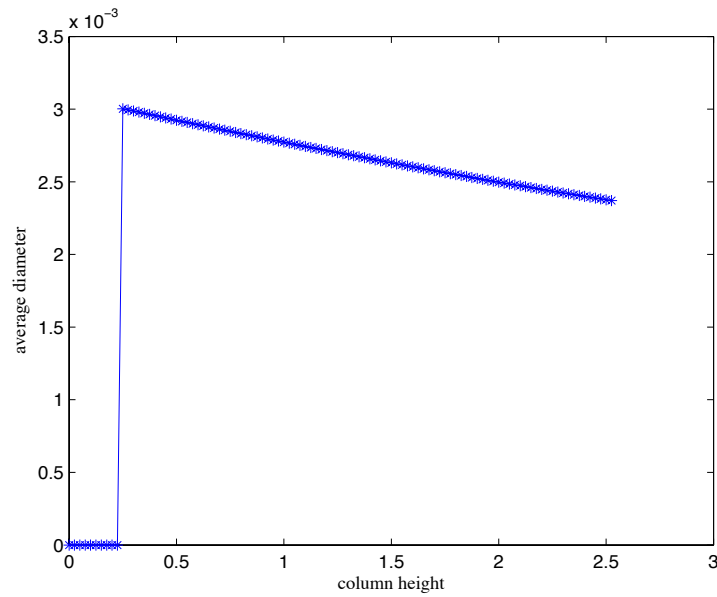


Figure 4.14: The average diameter of the droplets with constant breakage kernel 0.03 and coalescence kernel 10^{-7} .

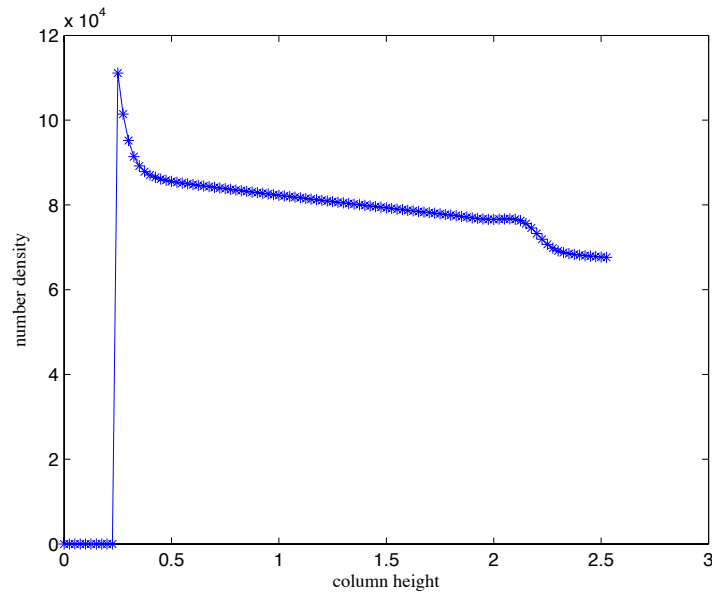


Figure 4.15: The number density of the droplets with non-constant breakage kernel and coalescence kernel.

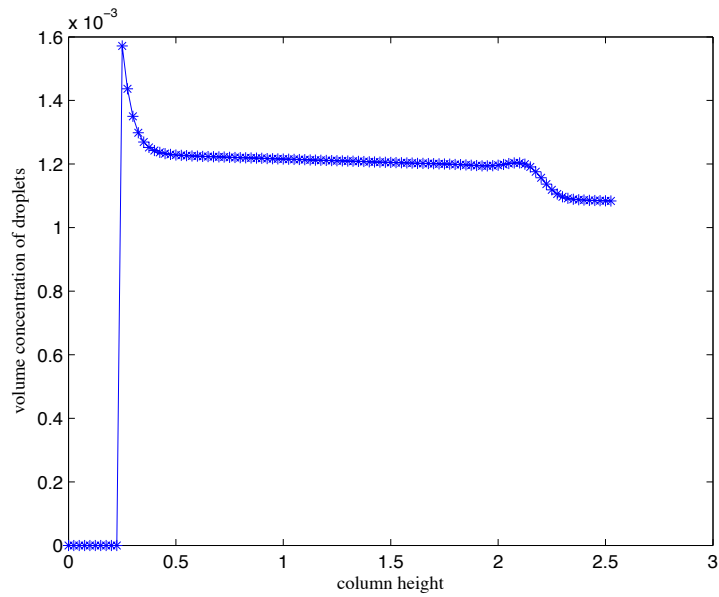


Figure 4.16: The volume concentration of the droplets with non-constant breakage kernel and coalescence kernel.

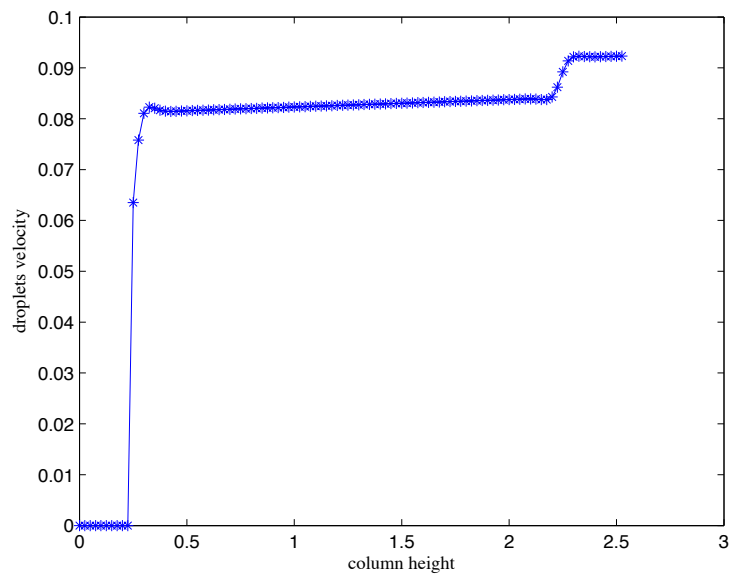


Figure 4.17: The average velocity of the droplets with non-constant breakage kernel and coalescence kernel.

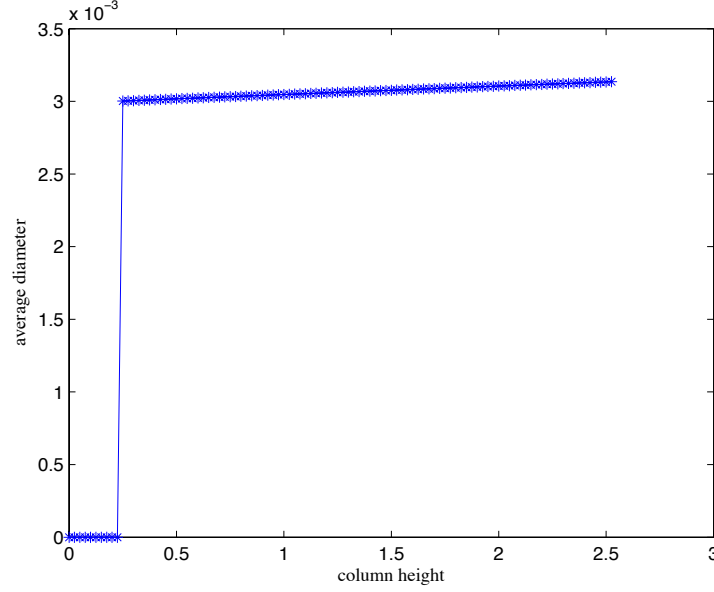


Figure 4.18: The average diameter of the droplets with non-constant breakage kernel and coalescence kernel.

aggregation kernel dominates slightly which is clear from Figures 4.15 and 4.18 since the number density of droplets decreases and the average diameter of droplets increases slightly.

Figures 4.16 and 4.17 show the volume concentration and velocity profiles of droplets respectively. We can see a little jump in velocity profile in the top part of the column which appears due to inlet of continuous phase.

4.1.4 Realistic Breakage and Coalescence Kernels

We implement the realistic breakage and coalescence kernels in the model and validate the results with experimental data. The droplet breakage frequency has been taken from the correlation based on single droplet experiments [30] and is given by :

$$\Gamma(d, \alpha_d) = P_r(d, N) \frac{|u_d|}{H_c}. \quad (4.1)$$

The breakage probability P_r is correlated with the system physical properties and the energy dissipation in the form below after Modes [68] based on a

correlation after Cauwenberg [69] :

$$\frac{P_r}{1 - P_r} = 1.2 \times 10^{-6} \cdot \left[\frac{\rho_c^{0.8} \mu_c^{0.2} d D_R 1.6 (2\pi)^{1.8} (N^{1.8} - N_{crit}^{1.8})}{\sigma} \right]^{2.88}, \quad (4.2)$$

where H_c is the RDC compartment height and N_{crit} is the critical rotor speed below which the breakage probability falls to zero and according to Schmidt [28] can be expressed as :

$$N_{crit} = 0.016 \frac{D_R^{-2/3} \mu_d d^{-4/3}}{(\rho_c \rho_d)^{1/2}} + \left[\left(0.008 \frac{D_R^{-2/3} \mu_d d^{-4/3}}{(\rho_c \rho_d)^{1/2}} \right)^2 + 0.127 \frac{\sigma}{\rho_c D_R^{4/3} d^{5/3}} \right]^{0.5}. \quad (4.3)$$

The daughter droplet distribution is assumed to follow the beta distribution [33] :

$$\beta(d|d') = 3\nu(\nu - 1) \left[1 - \left(\frac{d}{d'} \right)^3 \right]^{\nu-2} \frac{d^2}{d'^3}, \quad (4.4)$$

where $\nu \geq 2$ is the mean number of daughter droplets produced upon breakage of mother droplet of diameter d' . It is experimentally correlated and found dependent on the energy dissipation. In this work, we have taken $\nu = 2$.

According Coulaloglou [70] expressed the coalescence frequency as a product of collision rate and coalescence efficiency based on the kinetic theory of gases and obtained the following expression :

$$\omega(d, d', \alpha_d) = c_3 \frac{\phi^{1/3}}{1 + \alpha_d} (d + d')^2 (d^{2/3} + d'^{2/3})^{1/2} \times \exp \left(- \frac{c_4 \mu_c \rho_c \phi}{\sigma^2 (1 + \alpha_d)^3} \left(\frac{d d'}{d + d'} \right)^4 \right), \quad (4.5)$$

4.1.5 Pilot Plant RDC (height 2.55m)

To completely specify the column, the following geometry is used for a pilot plant RDC (see Figure 1.1) : *Column diameter* = 0.15m, $z_c = 2.25m$, *column diameter* = 0.15m, *compartment height* = 0.030m and $z_d = 0.25m$. The total flow rate of the continuous and dispersed phases are 1.66×10^{-5} and $2.22 \times 10^{-5} m^3/s$ respectively.

Figure (4.19) depicts the hold-up profiles of dispersed phase, where the hold-up at 200 rpm rotor speed is increased due to the increase of small droplets residence time. It is clear that the hold-up profiles of droplets decrease from its initial value to terminal value as the droplets accelerate from its initial

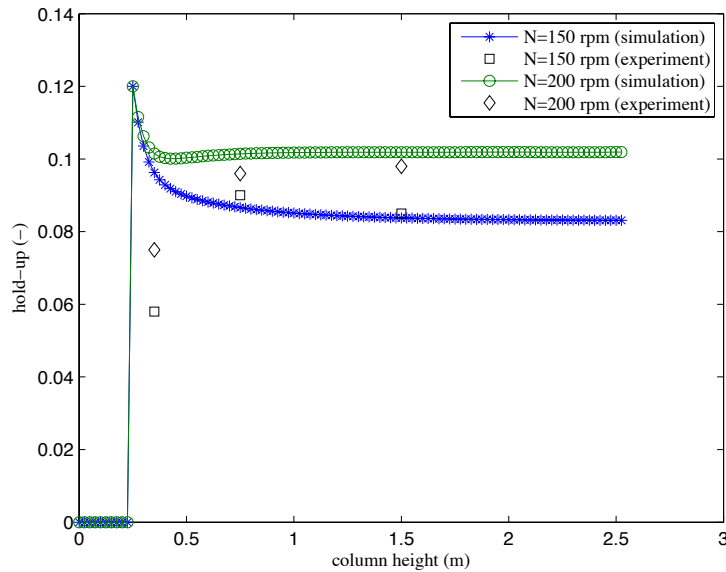


Figure 4.19: Simulated and experimental [71] hold-up profiles in a pilot plant RDC column at different rotor speeds using the system water/n-butyl acetate.

velocity to terminal velocity as shown in Figure (4.21). The steady state hold-up profiles were fairly predicted in the whole column except at the bottom of the column, where the general trend is predicted.

Figure 4.20 shows that droplet coalescence is dominant at the rotor speed of 150 rpm as indicated by the increase of the average droplet diameter along the column height. As the rotor speed is increased to 200 rpm, the two droplets interaction mechanisms (breakage and coalescence) are almost balanced with slight dominance of droplet breakage. This fact was reflected by the model of Tsouris and Tavlarides [36], where the coalescence efficiency decreases as the energy input increases.

Figure 4.21 gives the velocity profiles of the dispersed phase. It shows that the velocity at 150 rpm rotor speed is increased due to the increase of average diameter. This fact is reflected from the momentum balance equation, where drag force is a function of average diameter. Moreover, the steady state discontinuities due to the dispersed phase and continuous phase inlets are resolved by the mesh free method used in the simulation. The CPU time requirements on a PC of 3.06 GHz speed for this case is 14 s using a time

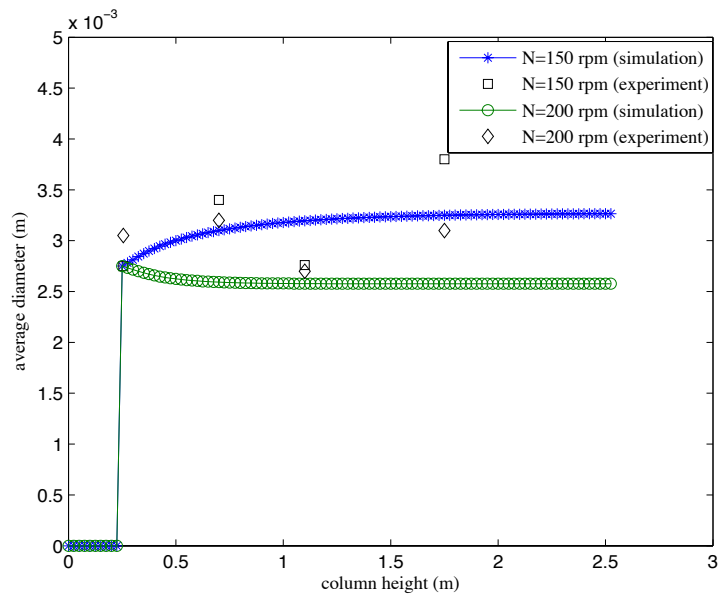


Figure 4.20: Simulated and experimental [71] average diameter in a pilot plant RDC column at different rotor speeds using the system water/n-butyl acetate.

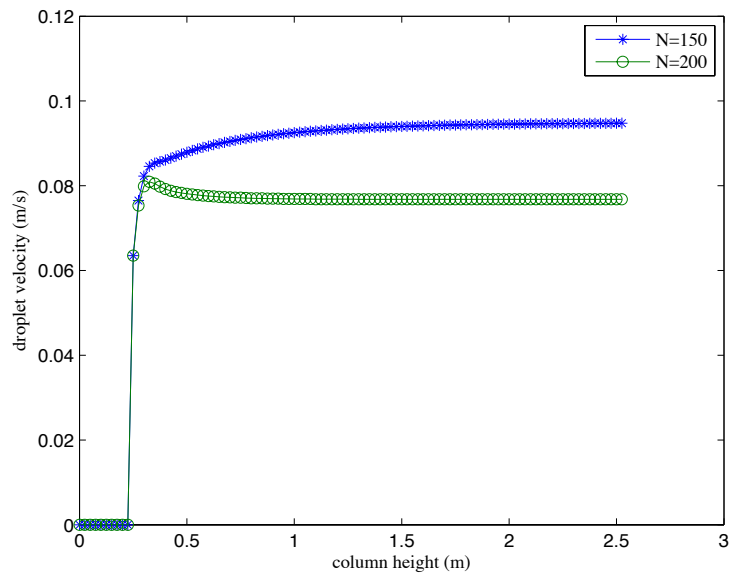


Figure 4.21: Simulated velocity profiles of dispersed phase in a pilot plant RDC column at different rotor speed using the system water/n-butyl acetate.

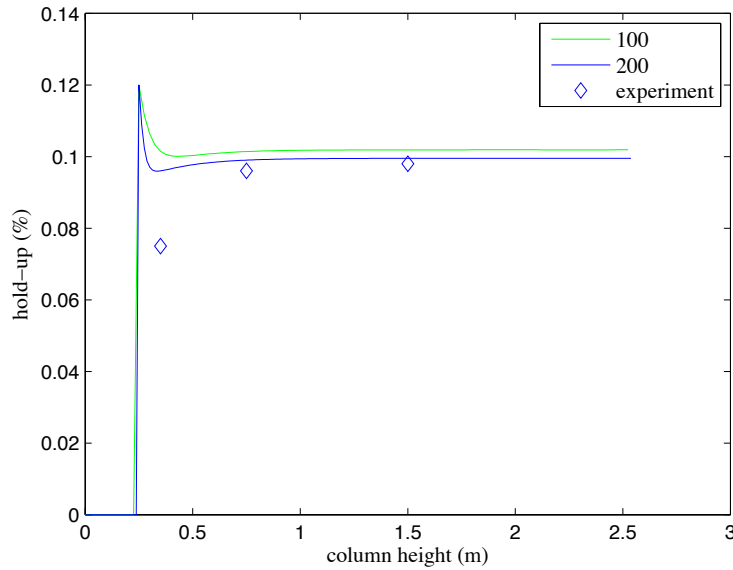


Figure 4.22: Simulated and experimental [71] hold-up profiles in a pilot plant RDC column at rotor speed 200 rpm at different FPM particles numbers 100 and 200 using the system water/n-butyl acetate.

step of 5×10^{-3} where only five equations are solved in this model.

To improve the accuracy of the model in the case of rotor speed 200 rpm (more turbulence), we increase the number of FPM particles (spatial particles) and simulate the model to see the impact of more FPM particles. We find that we can improve hold-up profiles which one can see in Figure 4.22 but the average diameter (Figure 4.23) is not improved as the number density of droplets also changes accordingly (Figure 4.24). This fact is reflected from the Equation (??). When we increase the number of FPM particles then the computational time of simulation also increases linearly. So we discuss the other way of improving the accuracy of model in the case of rotor speed 200 rpm (more turbulence) by increasing the number of primary particles in next section 4.2.

4.1.6 Pilot Plant RDC (height 4.0m)

The experimental hold-up, Sauter mean diameter and concentration profiles of the continuous and dispersed phases are taken from the work of Schmidt [72] and Garthe [73]. The simulation parameters used are from Schmidt [72],

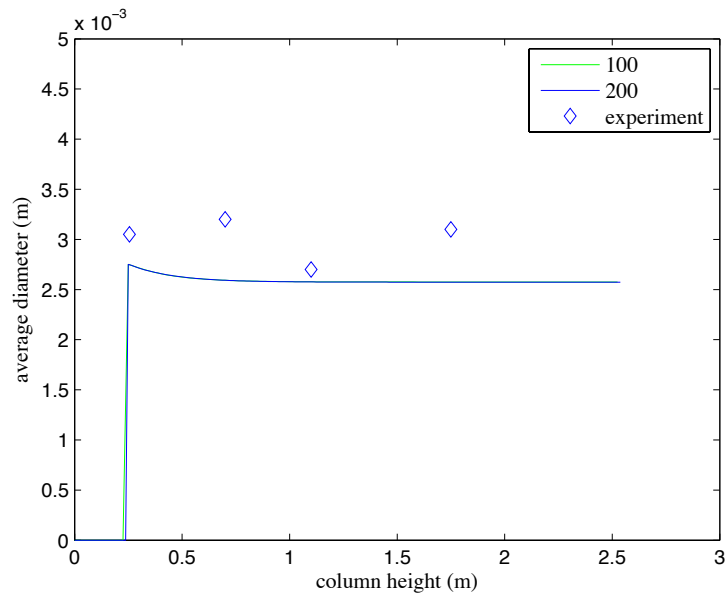


Figure 4.23: Simulated and experimental [71] average diameters in a pilot plant RDC column at rotor speed 200 rpm at different FPM particles numbers 100 and 200 using the system water/n-butyl acetate.

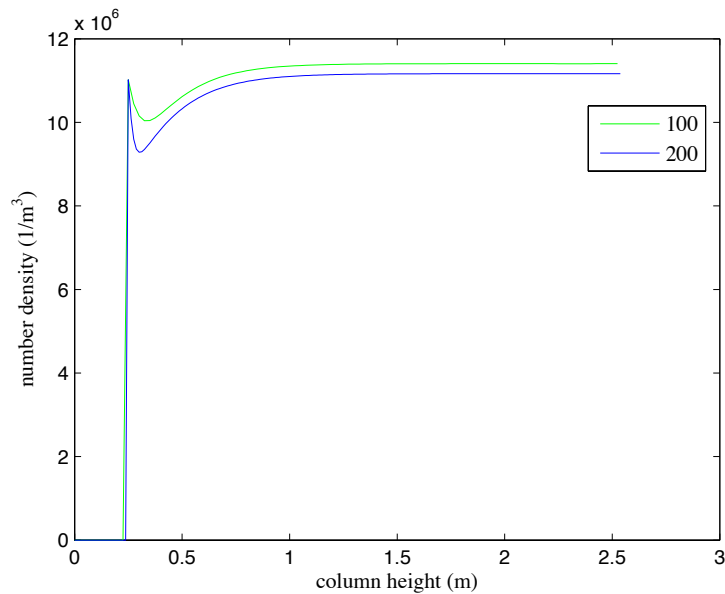


Figure 4.24: Simulated average number densities of droplets in a pilot plant RDC column at rotor speed 200 rpm at different FPM particles numbers 100 and 200 using the system water/n-butyl acetate.

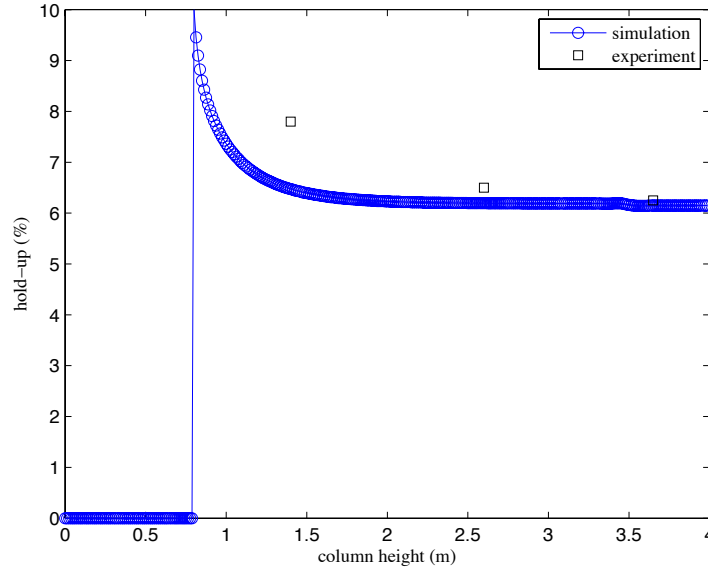


Figure 4.25: Comparison of simulated and experimental [73] hold-up profiles of droplets in a pilot plant RDC at 220 rpm.

and the mass transfer data from Garthe [73]. The total flow rate of the continuous and dispersed phases are 1.11×10^{-5} and $1.33 \times 10^{-5} m^3/s$ respectively.

Figure 4.25 shows the simulated hold-up profile of the dispersed phase along the column height. The discrepancy of the simulated results from those obtained in the experiment amounts to 12%, 4% and 1% in the lower, centre and top parts of the column respectively. We can see a peak in the hold-up profile which reflects the fact that the particles accelerate from its initial velocity to its terminal velocity over a short distance along the column. Figure 4.26 shows the simulated and experimental average diameter profiles. The relative errors are 0.05%, 10%, 5% and 5% in the lower, middle and top parts of the column respectively.

4.1.7 Simulation of a Kuehni Column (DN-150)

The simulation of a Kuehni column (DN-150) (Figure 4.27) is carried out using CFD-PBM coupled model with a specified correlations for the breakage and coalescence frequencies. The experimental data at steady state from [74] and [71] were used for comparison and the simulation parameters are summarized in Table 4.4. The simulation were done at a rotational speed

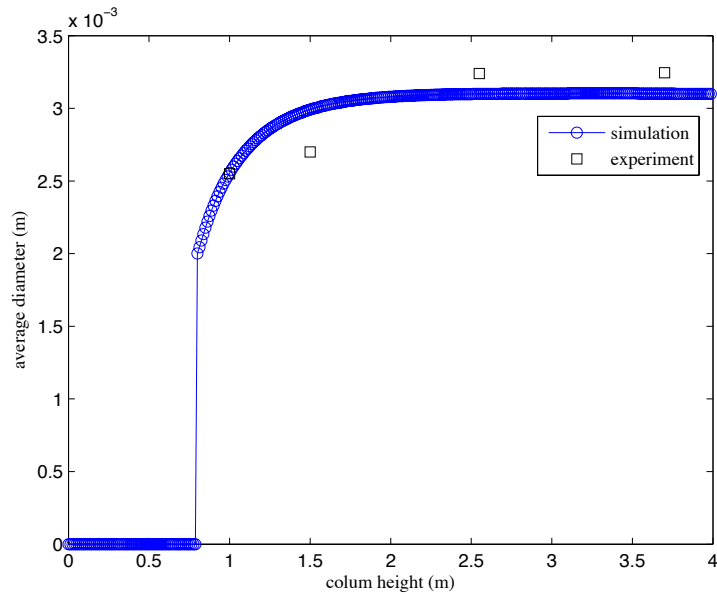


Figure 4.26: Comparison of simulated and experimental [73] droplet average diameter (d_{30}) of droplets in a pilot plant RDC DN-150 at 220 rpm.

Table 4.4: Physical Quantities

Volume flow rate of dispersed phase (l/h)	130/160/190
Volume flow rate of water (l/h)	130.00
Stirr speed (rpm)	160

of 160 rpm with water inflow of 130 l/h and solvent flow rate of 130 l/h, 160 l/h and 190 l/h. Both coalescence parameters, according to the model of (Coughlaloglou and Tavlarides), were estimated at rotational speed of 160 rpm. The results of simulations at a rotational speed of 190 rpm show that the hydrodynamics of the column is inaccurately predicted with this parameter set.

Figures 4.28, 4.29 and 4.30 show the hold-up profile of dispersed phase at different volumetric flow rates. The relative error in the simulated hold up for different dispersed phase flow rates (130 l/h and 160 l/h) is smaller than 5% which is clear from Figures 4.28 and 4.29. In Figure 4.30, we can see that the relative error in the simulated hold up for a volumetric flow rate 190 l/h is around 8%. We can notice that the change in the dispersed phase volumetric flow rate significantly affects the steady state hold-up profile.

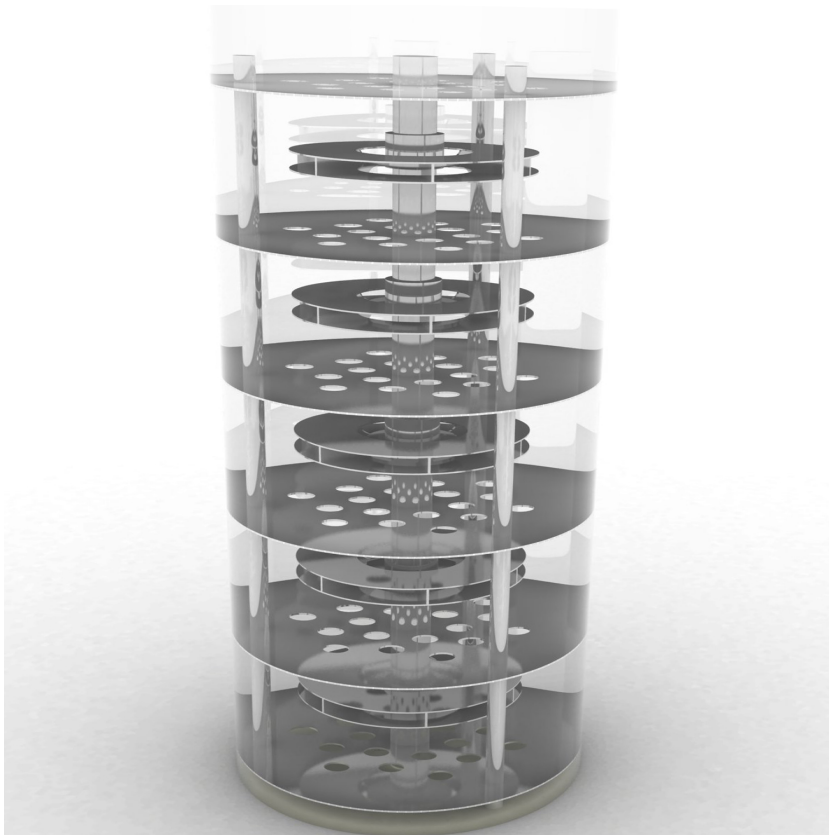


Figure 4.27: Kuehni Column.

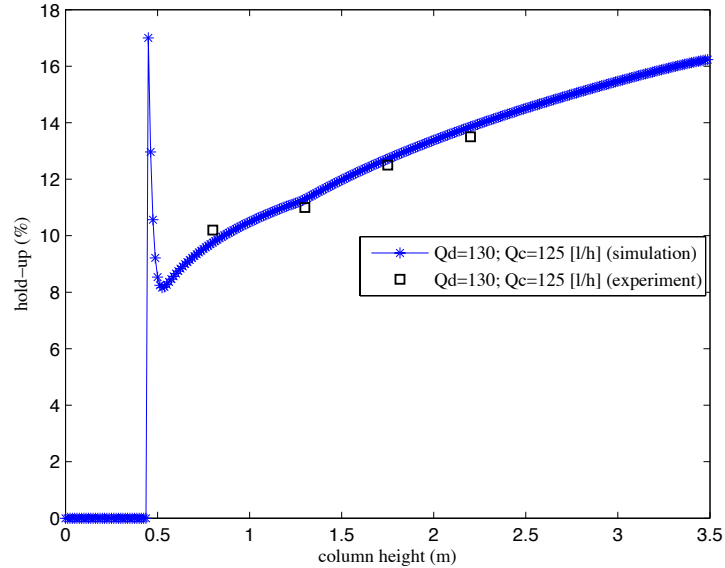


Figure 4.28: Comparison of simulated and experimental [74] hold - up profiles for Kuehni column DN-150 with inflow rates of continuous phase and dispersed phase 125 [l/h] and 130 [l/h] respectively at 160 rpm.

4.2 FPM-MPOSPM Solver

As we have mentioned in chapter 3 that sometimes to get better accuracy, we have to increase the number of primary particles which depends on the nature of breakage and coalescence kernels. In this section we show the solution of the model using MPOSPM. We can use this solver in two ways. One as two fluid model and other one as multi-fluid model.

4.2.1 Two-Fluid Model

In the case of two fluid model, we consider one continuous phase and other one dispersed phase. We take more classes (primary particles) of droplets but we assume that all primary particles move with same average velocity. In this case we have more sections for droplets so we need more equations for number density and volume fraction. After calculating the number density and volume fraction, we evaluate the average diameter then we plug this diameter in momentum equation to evaluate the velocity of the dispersed phase. We have used same column geometry which was given in Table 4.2.

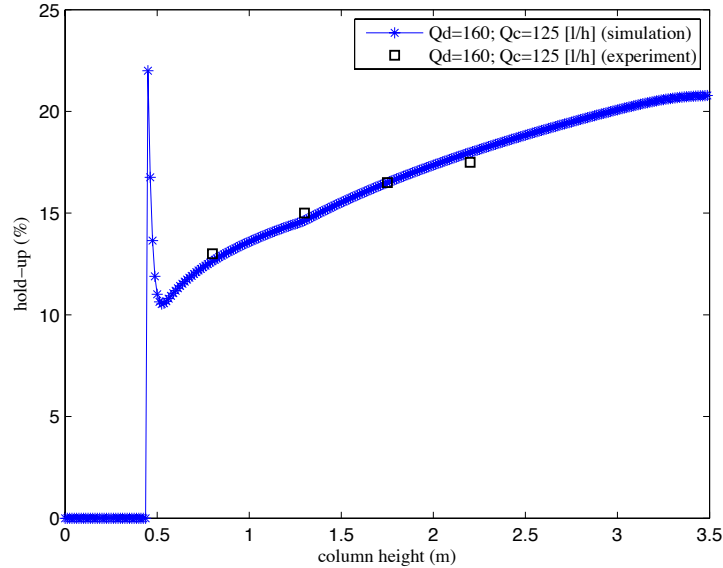


Figure 4.29: Comparison of simulated and experimental [74] hold - up profiles for Kuehni column DN-150 with inflow rates of continuous phase and dispersed phase 125 [l/h] and 160 [l/h] respectively at 160 rpm.

Constant kernels

We have taken the constant breakage kernel 0.03 and coalescence kernels 10^{-6} to solve the model. We have chosen two primary particles and have displayed the number density (Figure 4.31), volume concentration of droplets (Figure 4.32) and average diameter of droplets (Figure 4.34) of each primary particle. As we have noticed in the previous section, that the aggregation kernel dominates in this case which we can see in Figure 4.31 as the number density for second primary particles is increasing and the number density for first primary particle is decreasing. It means that drops aggregate in first class (first primary particle) and jump to second class (second primary particle). Figure 4.32 shows the volume concentration profile of each primary particle. We can see that the volume concentration of second primary particle is increasing along the column height which is expected as aggregation kernel is dominating. Figure 4.34 show the average diameter of droplets for each class. We can see that the average diameter for second primary particle is increasing continuously along column height after the inlet of dispersed phase which again reflects the fact of dominance of aggregation kernel. We can see the velocity profiles of dispersed phase and continuous phase in Figures 4.33

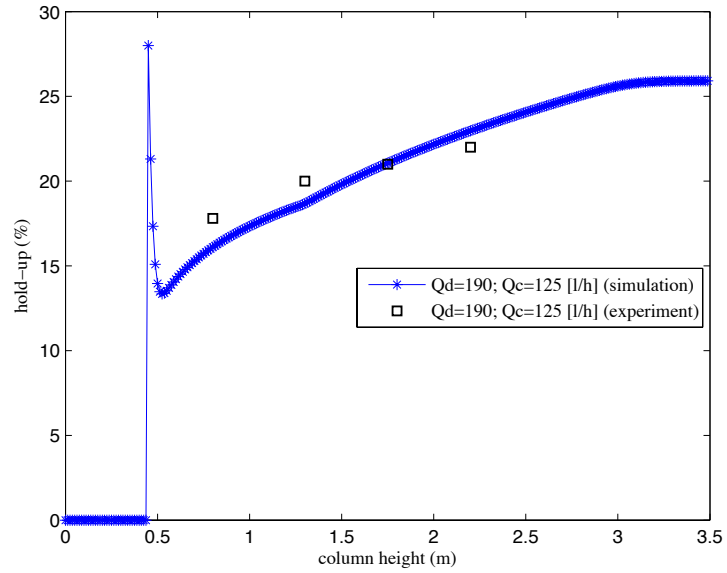


Figure 4.30: Comparison of simulated and experimental [74] hold - up profiles for Kuehni column DN-150 with inflow rates of continuous phase and dispersed phase 125 [l/h] and 190 [l/h] respectively at 160 rpm.

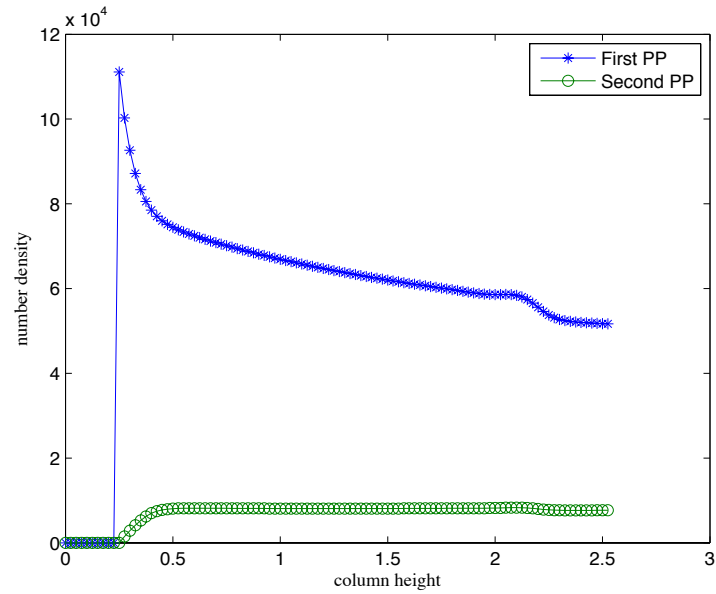


Figure 4.31: The number density of the droplets with constant breakage kernel 0.03 and coalescence kernel 10^{-6} .

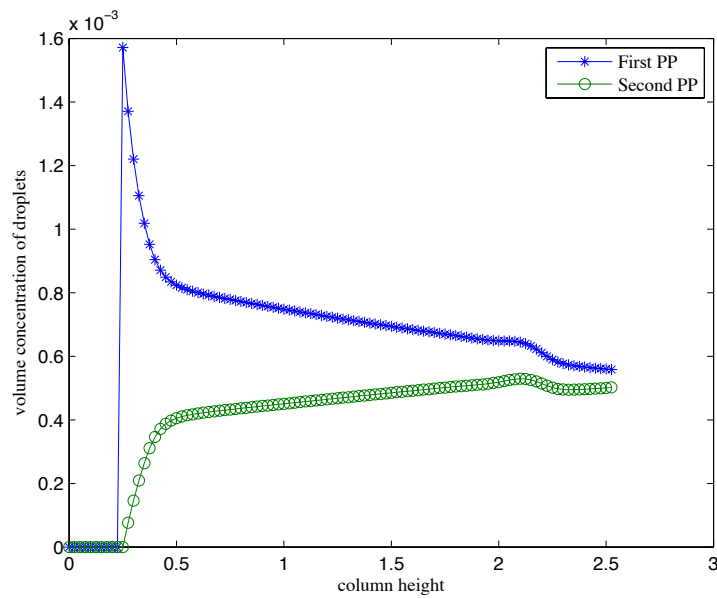


Figure 4.32: The volume concentration of the droplets with constant breakage kernel 0.03 and coalescence kernel 10^{-6} .

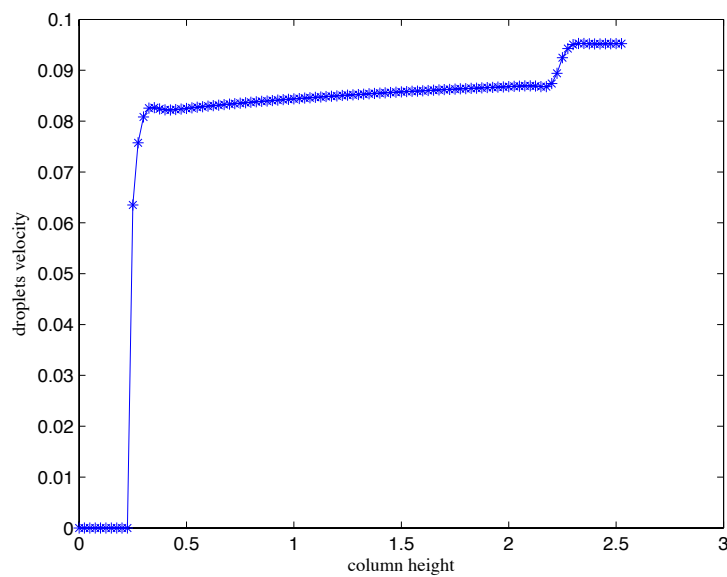


Figure 4.33: The average velocity of the droplets with constant breakage kernel 0.03 and coalescence kernel 10^{-6} .

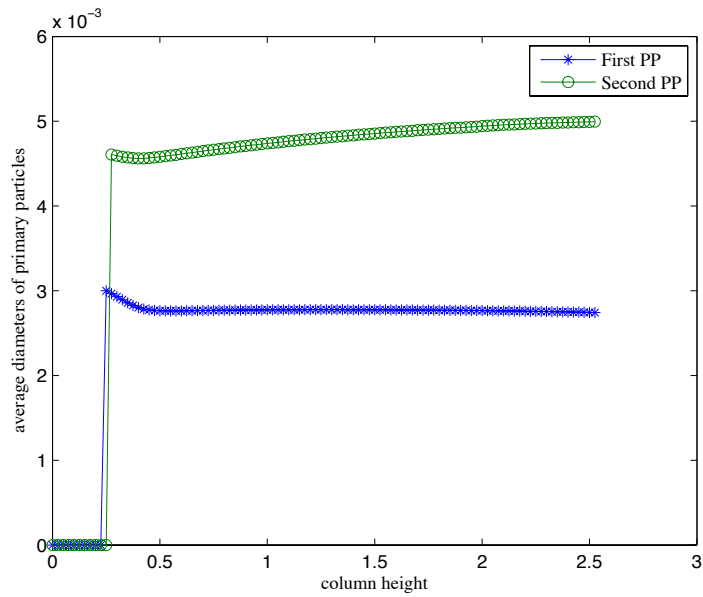


Figure 4.34: The average diameter of the droplets with constant breakage kernel 0.03 and coalescence kernel 10^{-6} .

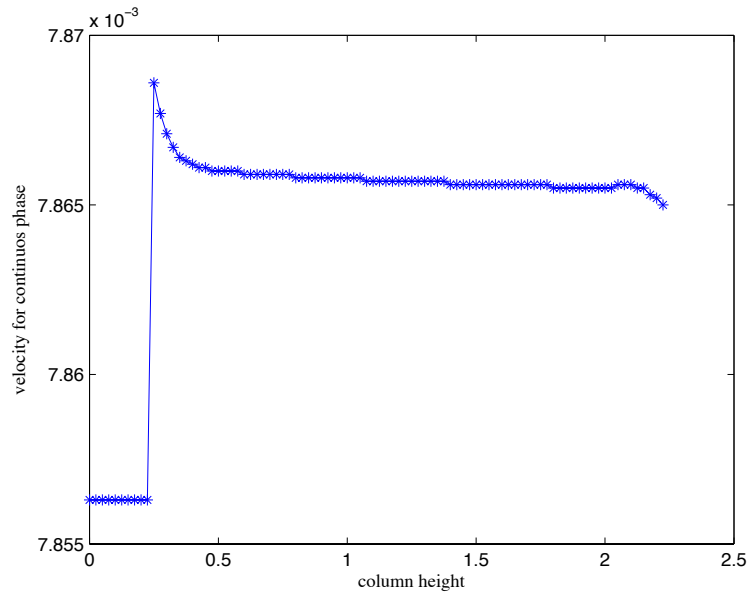


Figure 4.35: The average diameter of the droplets with constant breakage kernel 0.03 and coalescence kernel 10^{-6} .

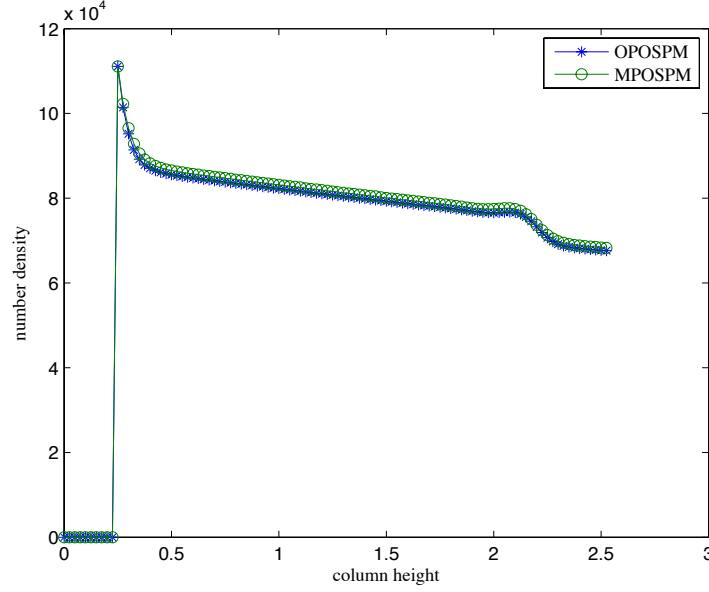


Figure 4.36: The average number density of the droplets with non-constant breakage kernel $0.1 \times d^3$ and coalescence kernel $2(d^3 + d'^3)$.

and 4.35.

Non-constant kernels

In this subsection we consider the non-constant breakage and coalescence kernels and then we compare the results of FPM-OPOSPM solver and FPM-MPOSPM solver.

Figure 4.36 shows the comparison of the FPM-OPOSPM and FPM-MPOSPM solvers for the number density profiles of the droplets. It is clear that the profile of number density (Figure 4.36), volume concentration (Figure 4.37), velocity of droplets (Figure 4.38) and the average diameter of droplets (4.39) are quite similar for both solvers (FPM-OPOSPM and FPM-MPOSPM) in the case of breakage kernel ($0.1 \times d^3$) and aggregation kernel ($2(d^3 + d'^3)$). It is clear that FPM-OPOSPM solver is quite a good choice to solve the coupled CFD-PBM model as in this case the time of computation is quite small as we have to solve only three equations in the case of only momentum transfer between phases in one-dimensional space but on the other hand, in case of FPM-MPOSPM solver, one has to solve $2 \times n_{pp} + 1$ equations which is quite expensive in the terms of computation. Note that one has to

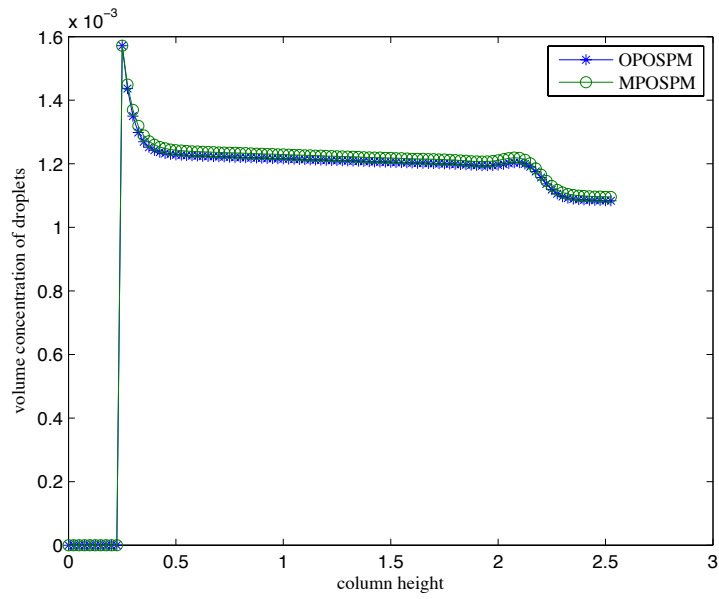


Figure 4.37: The volume concentration density of the droplets with non-constant breakage kernel $0.1 \times d^3$ and coalescence kernel $2(d^3 + d'^3)$.

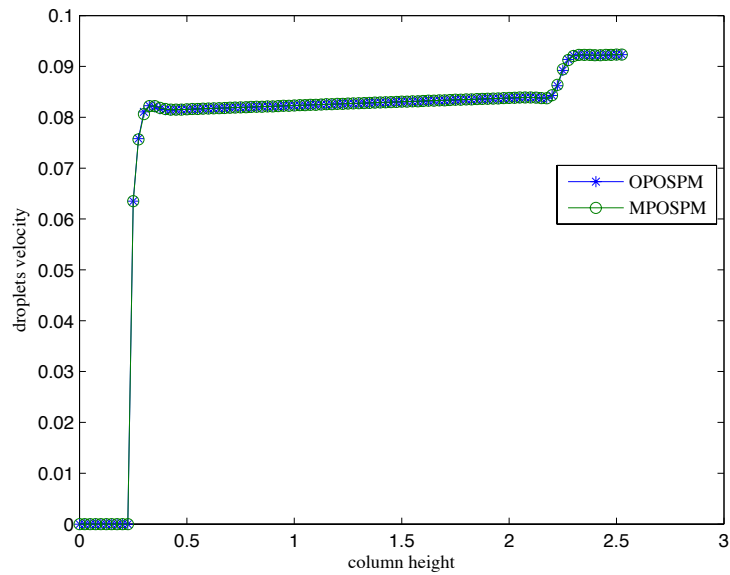


Figure 4.38: The velocity of the droplets with non-constant breakage kernel $0.1 \times d^3$ and coalescence kernel $2(d^3 + d'^3)$.

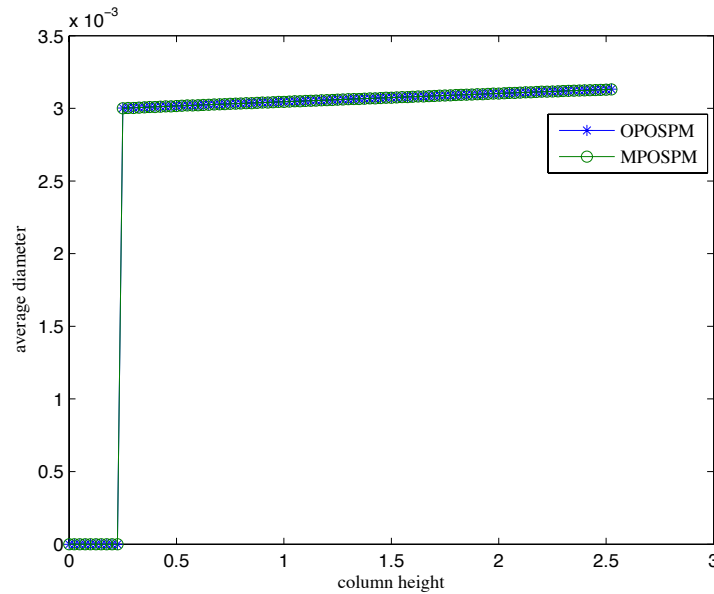


Figure 4.39: The volume concentration density of the droplets with non-constant breakage kernel $0.1 \times d^3$ and coalescence kernel $2(d^3 + d'^3)$.

take more primary particles to predict the physical quantities of both phases sometimes in the cases of complicated breakage and coalescence kernels.

4.2.2 Multi-Fluid Model

As we have mentioned at the start of the current section that one can use FPM-MPOSPM solver as a multi-fluid model. In this case we suppose that each primary particle moves with its own velocity which means that the momentum equation for each primary particle has to be solved separately. When the breakage and aggregation kernels are too complicated and the flow is turbulent then we need to consider the model as a multi-fluid model to predict the experimental data more accurately. Solving the model equations in this way is a bit expensive as one has to solve all the model equations for each phase at each time step.

The comparison of two-fluid model (FPM-OPOSPM solver) with experimental data, in the case of the Pilot Plant RDC (height $2.55m$) has been shown in subsection 4.1.5. Now we consider a three-fluid model by choosing two primary particles so that one phase from continuous phase and the other two

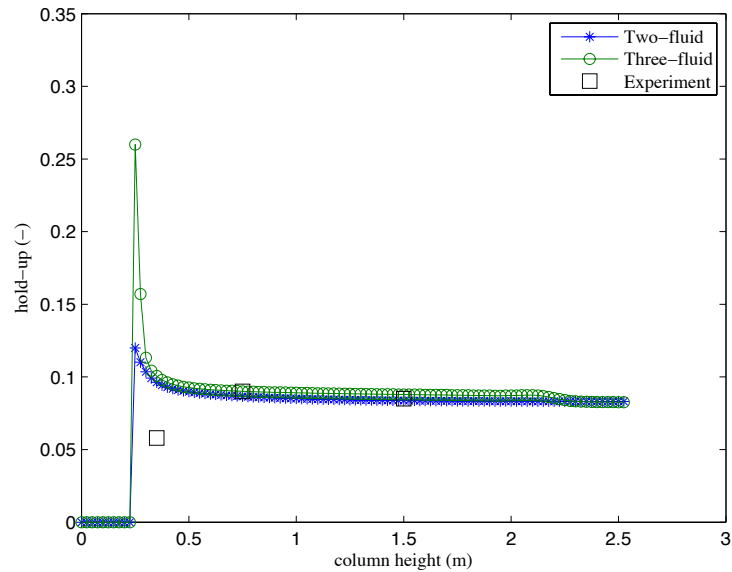


Figure 4.40: Simulated and experimental [71] hold-up profiles in a pilot plant RDC column at rotor speed 150rpm using the system water/n-butyl acetate.

phase from the dispersed phase.

Figure 4.40 and 4.41 show the comparison of hold-up profile and average diameter of droplets solved by two-fluid model and multi-fluid model with experimental data at rotor speed 150 rpm. We find that multi-fluid model does not make much difference in this case as two-fluid model also predicts the experimental data quite accurately.

The comparison of hold-up profiles solved by two-fluid model and three-fluid model with experimental data at rotor speed 200 rpm is shown in Figure 4.42. The relative error in this case is reduced a little bit but in the case of average diameter (Figure 4.43), the accuracy has increased and the relative error is less than 8%, which is around 12% for the two-fluid model. We find that the three-fluid model reduce the relative error in the case of higher rotor speed (more turbulence). Figure 4.44 shows the velocity profiles of both primary particles (both dispersed phases). The velocity of second primary particle is higher than the velocity of first primary particle along the column height which is due to the dependency of drag force on average diameter (momentum equation). The velocity of second primary particle decreases near the

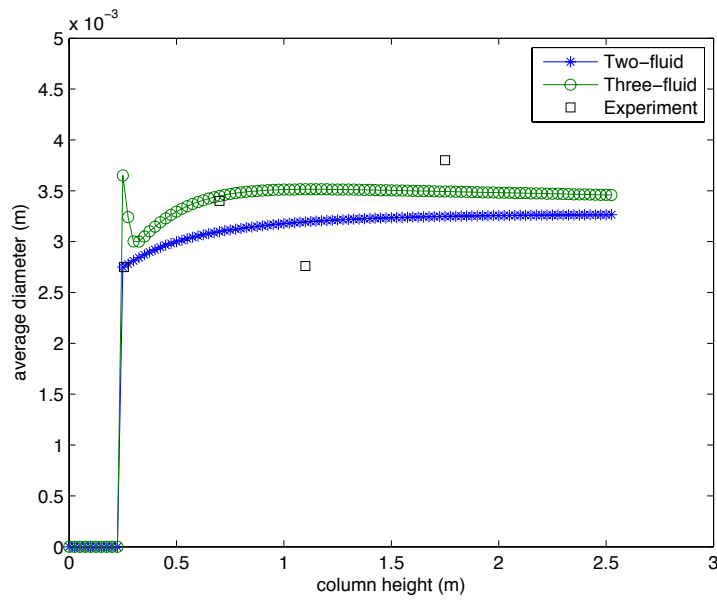


Figure 4.41: Simulated and experimental [71] average diameter of droplets in a pilot plant RDC column at rotor speed 150 rpm using the system water/n-butyl acetate.

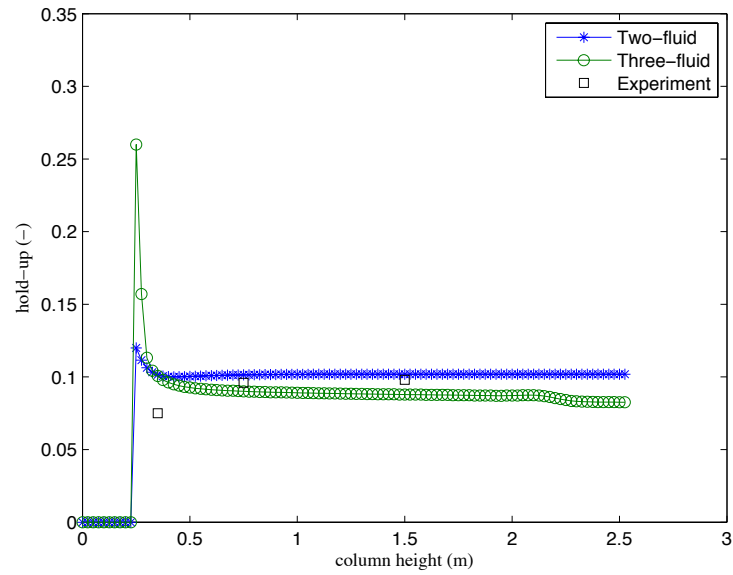


Figure 4.42: Simulated and experimental [71] hold-up profiles in a pilot plant RDC column at rotor speed 200 rpm using the system water/n-butyl acetate.

inlet of dispersed phase but after that it increases as particles accelerate to its terminal velocity. We can see jumps in velocity profiles at inlet of continuous phase because the velocity of continuous phase becomes zero after its inlet.

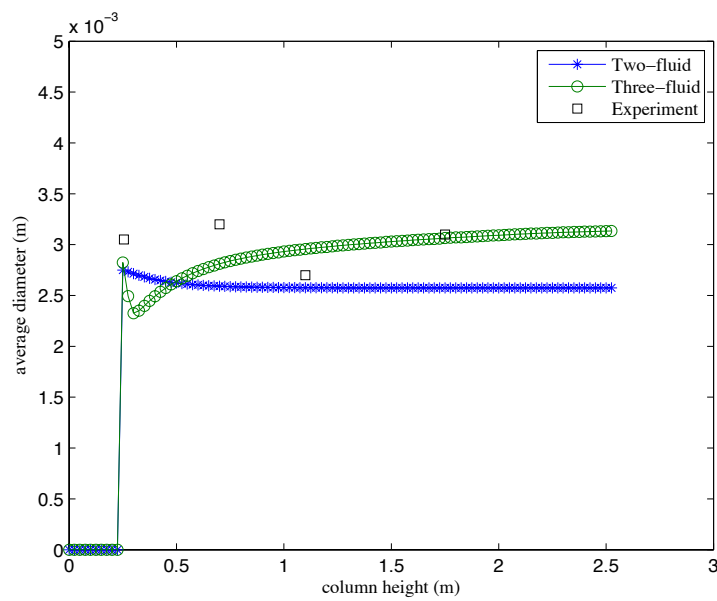


Figure 4.43: Simulated and experimental [71] average diameter of droplets in a pilot plant RDC column at rotor speed 200 rpm using the system water/n-butyl acetate.

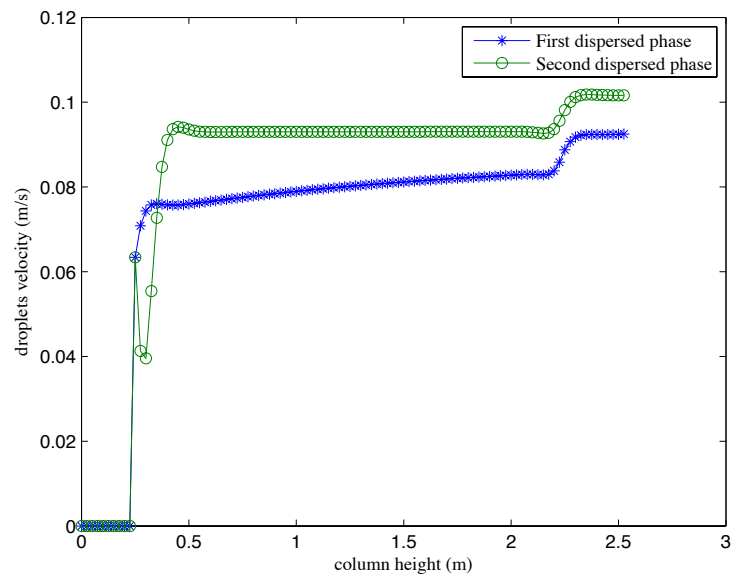


Figure 4.44: Simulated velocity profile of droplets in a pilot plant RDC column at rotor speed 200 rpm using the system water/n-butyl acetate.

Chapter 5

Mass Transfer Between Liquid-Liquid Phases

In this chapter, the solution of CFD-bivariate PBE coupled model is discussed. We have considered two phases (continuous and dispersed) and mass transfer between them. A two fluid model that considers only one primary particle is discussed. To solve the model we have used FPM-OPOSPM solver. OPOSPM is used to simplify the BPBE and then FPM solver is needed to solve the model equations numerically. The numerical results are validated with experimental data which is also discussed at the end of this chapter.

5.1 Influence of Breakage and Coalescence Kernels

The impact of the coalescence and breakage kernels on the solute concentrations is shown in Figures 5.1,5.2. The dependency of mass transfer from continuous phase to dispersed phase is not much like the mass transfer coefficient. But we can see that when the aggregation kernel dominates in the flow i.e. the average diameter of the droplets increases or the number density of droplets decreases, then the solute concentration of dispersed phase decreases (Figure 5.1). And on the other side, the solute concentration of the continuous phase slightly increases along the column height which is clear from Figure 5.2.

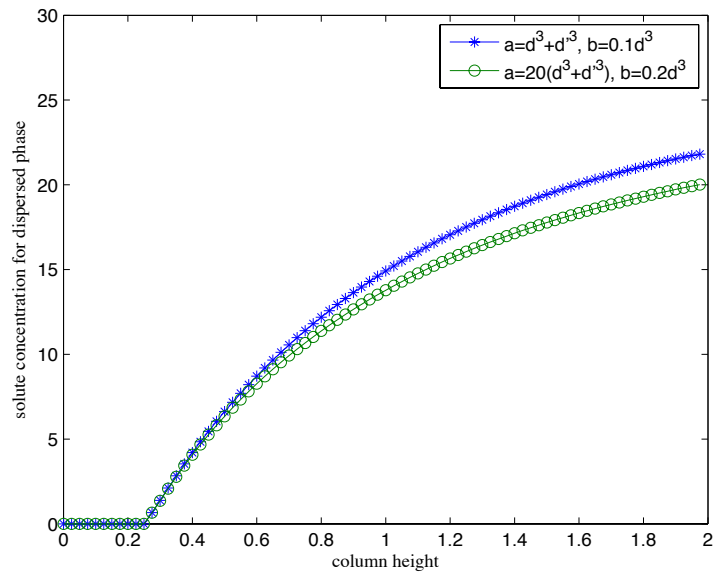


Figure 5.1: The comparison of the solute concentrations of the dispersed phase for different coalescence and breakage kernels.

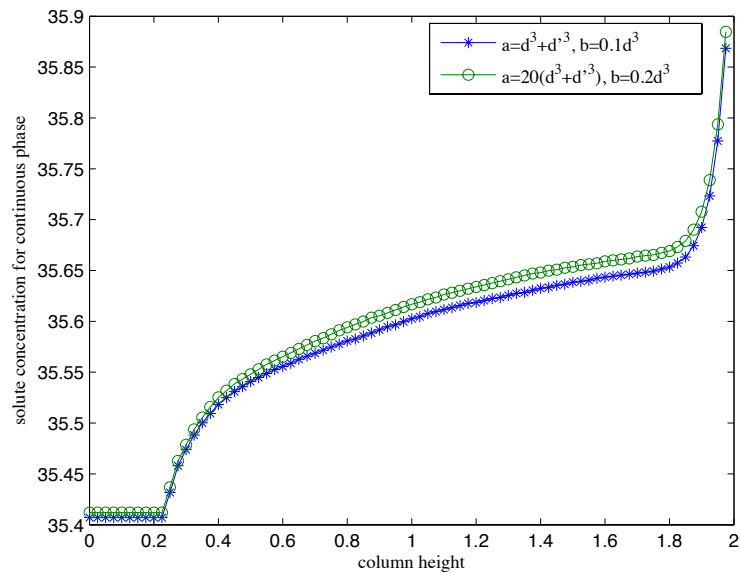


Figure 5.2: The comparison of the solute concentrations of the continuous phase for different coalescence and breakage kernels.

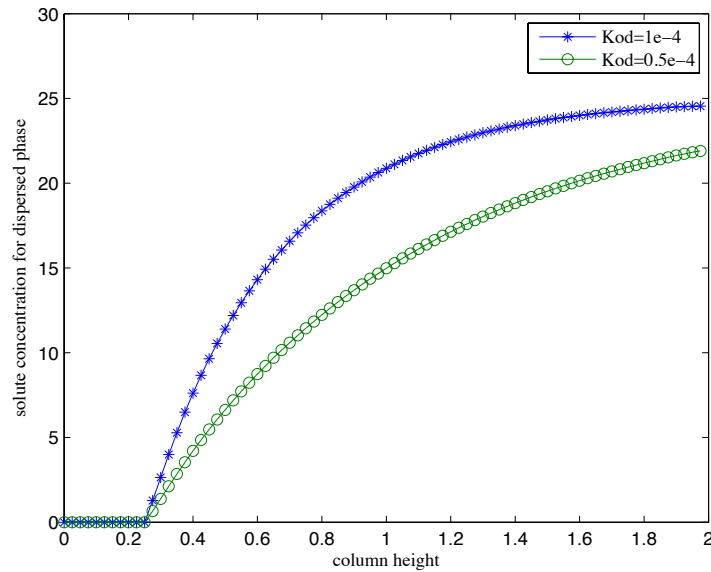


Figure 5.3: The comparison of the solute concentrations of the dispersed phase for different mass transfer coefficient.

5.2 Influence of Mass Transfer Coefficient

In this section, the impact of mass transfer coefficient on the solute concentration profiles for both phases is discussed. The model is solved by FPM-OPOSPM solver. When we talk about bivariate PBE then we have to consider mass transfer coefficient as breakage kernel and coalescence kernels. Mass transfer coefficient plays an important role in the solution of bivariate PBE. First, we have considered a constant mass transfer coefficient.

5.2.1 Constant Mass Transfer Coefficient

In the Figures 5.3,5.4, we can see the effect of mass transfer coefficient. Figure 5.3 shows the profile of solute concentration of the dispersed phase for different mass transfer coefficients as we can notice that when mass transfer coefficient is double then the mass transfers a bit faster and solute concentration in the dispersed phase increases. The profile of solute concentration of the continuous phase is shown in Figure 5.4 which concludes that when mass transfer coefficient is large then the mass transfers a bit fast in the lower half part of the column and the solute concentration in the continuous

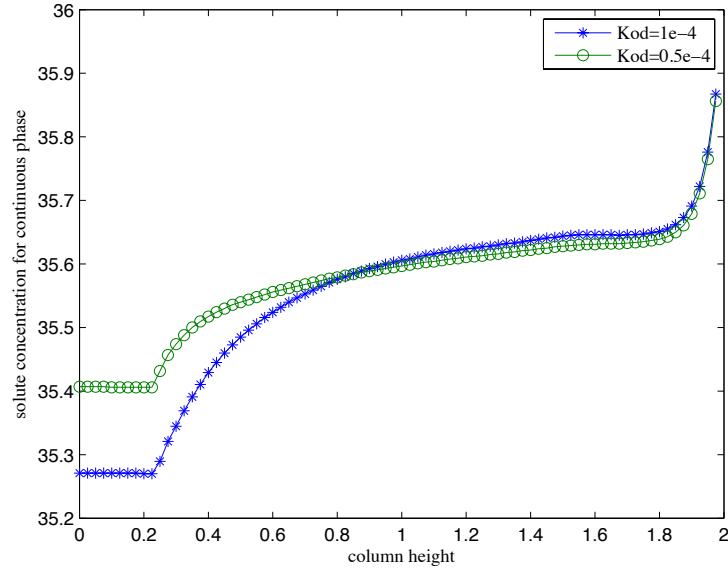


Figure 5.4: The comparison of the solute concentrations of the continuous phase for different mass transfer coefficient.

phase decreases in this part of the column. From Figures 5.3,5.4, one can say that the mass transfer from continuous phase to dispersed phase is strongly depends on the mass transfer coefficient.

5.2.2 Realistic Mass Transfer Coefficient

In this section, the model is simulated for realistic mass transfer coefficients and the results are compared with the experimental data for the columns RDC (DN-150) and Kuehni column (DN-150).

The mass transfer coefficients for the dispersed phase k_d and for the continuous phase k_c have been given by Handlos and Baron [75] and Heertjes [76] respectively as :

$$k_d = 0.00375 \cdot \frac{u_d}{1 + (\mu_d/\mu_c)} \quad (5.1)$$

and

$$k_c = 0.83 \cdot \sqrt{\frac{D_c |u_d - u_c|}{d}}. \quad (5.2)$$

The axial dispersion coefficients for both phases have been taken approximately as constants of magnitude 10^{-5} [77].

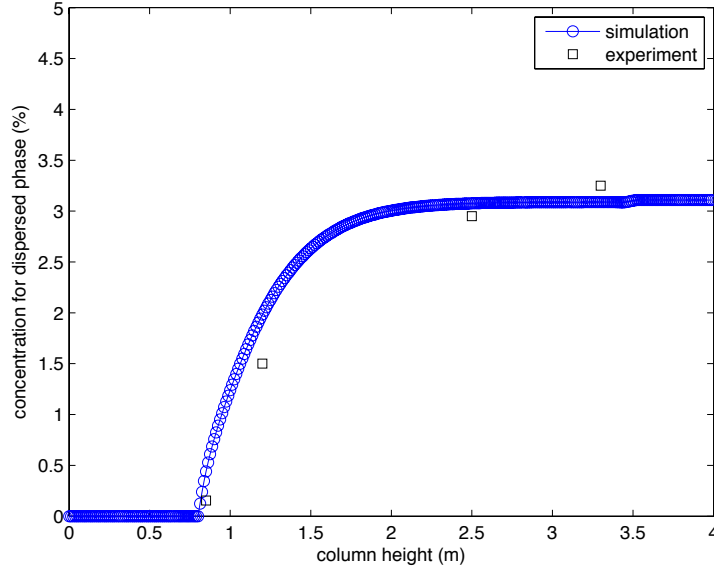


Figure 5.5: Comparison of simulated and experimental [73] concentration profiles of droplets in a pilot plant RDC at 220 rpm.

Overall mass transfer coefficient (K_{od}) is expressed as

$$K_{od} = \frac{1}{\frac{m}{K_c} + \frac{1}{K_d}}, \quad (5.3)$$

where m is the solute distribution coefficient.

Pilot Plant RDC (height 4.0m)

The experimental concentration profiles of the continuous and dispersed phases are taken from the work of Schmidt [72] and Garthe [73]. The simulation parameters are used from Schmidt [72], and mass transfer data from Garthe [73]. The total flow rate of the continuous and dispersed phases are 1.11×10^{-5} and $1.33 \times 10^{-5} m^3/s$ respectively.

Figures 5.5 and 5.6 show the simulated and experimental solute concentration profiles in the dispersed and continuous phases along the column height respectively at 220 rpm. The relative error is less than 12%, with the exception of the dispersed phase concentration at the column exit.

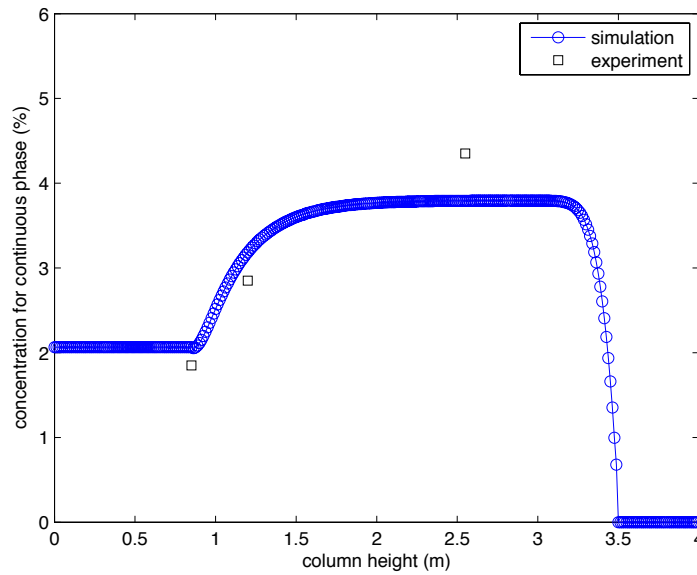


Figure 5.6: Comparison of simulated and experimental [73] concentration profiles of the continuous phase in a pilot plant RDC at 220 rpm.

Kuehni Column (DN-150)

We have simulated the model for Kuehni column (DN-150). We have used stirrer speed as 160 rpm, flow rate for dispersed phase Q_d as 160 l/h and flow rate for continuous phase Q_c as 130 l/h. Figure 5.7 shows the simulated and experimental solute concentration profiles in the dispersed phase. The relative error is less than 5% along the column height except the upper part of column where it is around 7%. The simulated and experimental solute concentration profiles in the continuous phase is shown in Figure 5.8. It is clear that the relative error is less than 10%. One can conclude from Figures 5.5, 5.6, 5.7 and 5.8 that the FPM-OPOSPM solver predict the solute concentration quite accurately for RDC (DN-150) and Kuehni (DN-150) columns.

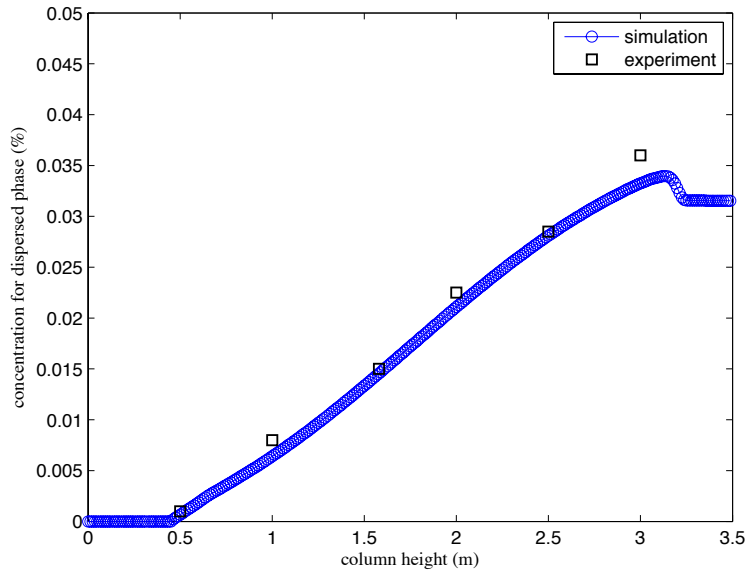


Figure 5.7: Concentration profile for the dispersed phase in a Kuehni column (experimental data are from Zamponi [74]).

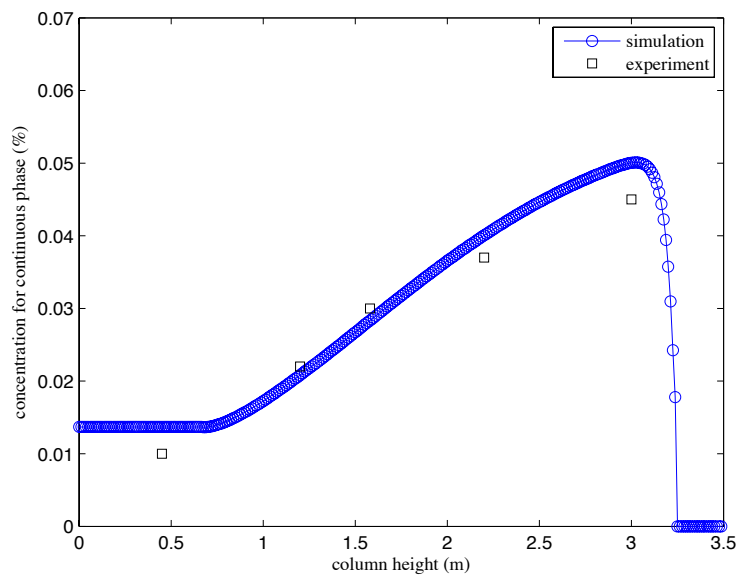


Figure 5.8: Concentration profile for the continuous phase in a Kuehni column (experimental data are from Schmidt [72]).

Chapter 6

Conclusion

In this thesis a comprehensive mathematical framework and meshfree Lagrangian particle method, called Finite Pointset Method (FPM) are presented for the coupled model of CFD and Population Balance Equation (PBE); that can be used for the numerical simulation of one-dimensional liquid-liquid flow in extraction column. The hyperbolicity nature of the model is studied. We have shown that the reduced meshfree population balance model using the OPOSPM and MPOSPM can be viewed as a multi-fluid model.

The derivation of PBE is discussed. The analytical solution and the numerical solution of PBE are discussed. We have compared the numerical methods to solve PBE and have chosen the OPOSPM and MPOSPM in terms of accuracy and the time of computation. The model is solved by using two solvers i.e. FPM-OPOSPM solver and FPM-MPOSPM solver. The CFD-PBM model is coupled for both the monovariate PBE and bivariate PBE. The OPOSPM and MPOSPM are successfully implemented in a mesh free framework for one-dimensional case. The hydrodynamics and mass transfer between liquid-liquid phases are shown. The error analysis of MPOSPM is also shown.

The influence of breakage and aggregation kernels on the momentum transfer and mass transfer between liquid-liquid phases are studied in the case of constant and non-constant kernels. We have seen the influence of average diameter of droplets on the physical quantities like number density, volume concentration, solute concentration and velocity of liquid. The constant and non-constant mass transfer coefficient and impact of them are shown.

Correlated aggregation and breakage kernels as well as mass transfer coefficients are used to close the reduced model. The simulated results are successfully compared with the experimental data available from the literature. The impact of rotor speed (turbulent nature of flow) on the simulation of model is shown. The numerical results are validated for Rotating Disc Contactor (RDC DN-150) and Kuehni column. We have seen the good agreement between numerical results and experimental data.

Appendix A

A.1 Analytical formulation of the velocity of the continuous phase

The analytical formulation of the velocity of the continuous phase is given by Attarakih [5]. The continuity equations for continuous phase and the dispersed phase in the case of one-dimension can be written in the following form :

$$\frac{\partial \alpha_c}{\partial t} - \frac{\partial(\alpha_c u_c)}{\partial z} = \frac{Q_c^{in}}{Ac} \delta(z - z_c) \quad (A.1)$$

and

$$\frac{\partial \alpha_d}{\partial t} + \frac{\partial(\alpha_d u_d)}{\partial z} = \frac{Q_d^{in}}{Ac} \delta(z - z_d). \quad (A.2)$$

The velocity for the continuous phase is considered negative as the flow is taken from bottom of the column to the top of the column. By adding the Equations (A.1 and A.2), we get

$$\frac{\partial(\alpha_c + \alpha_d)}{\partial t} + \frac{\partial(\alpha_d u_d - \alpha_c u_c)}{\partial z} = \frac{Q_c^{in}}{Ac} \delta(z - z_c) + \frac{Q_d^{in}}{Ac} \delta(z - z_d). \quad (A.3)$$

The first term of Equation (A.3) becomes zero because of the constraint $\alpha_c + \alpha_d = 1$. After integrating Equation (A.3) from 0 to H (height of column), we get the expression for the velocity of continuous phase as

$$u_c = \frac{1}{Ac(1 - \alpha_d)} (Q_c^{in} \Delta c + Q_d^{in} \Delta d - \alpha_d(H) u_d(H) + \alpha_d u_d), \quad (A.4)$$

Where

$$\Delta c = \begin{cases} 1 & \text{if } z < z_c \\ 0 & \text{otherwise} \end{cases}$$

and

$$\Delta d = \begin{cases} 1 & \text{if } z > z_d \\ 0 & \text{otherwise} \end{cases} .$$

To get the analytical formulation for the velocity of continuous phase at steady state, we write the continuity equation of continuous phase at steady state as

$$-\frac{\partial}{\partial z}(\alpha_c u_c) = \frac{Q_c^{in}}{Ac} \delta(z - z_c). \quad (\text{A.5})$$

After integrating the Equation (A.5) from 0 to H (column height) , we get the analytical formulation for the velocity of continuous phase at steady state in the following form :

$$u_c = \frac{1}{(1 - \alpha_d)} \frac{Q_c^{in}}{Ac} \Delta c. \quad (\text{A.6})$$

Appendix B

B.1 Length-based form of PBE (Population Balance Equation)

The transformation of PBE from volume form to length-based form is presented by Marchisio [78].

The homogeneous population balance equation in volume form is given by

$$\begin{aligned} \frac{\partial f'(v, t)}{\partial t} + \frac{\partial}{\partial v}(G(v, t)f'(v, t)) &= \frac{1}{2} \int_0^v a'(v - v', v')f'(v - v', t)f'(v', t)dv' \\ &- f'(v, t) \int_0^\infty a'(v, v')f'(v', t)dv' \\ &+ \int_v^\infty b'(v')\beta'(v | v')f'(v', t)dv' - b'(v)f'(v, t). \end{aligned} \quad (\text{B.1})$$

The volume-based and length-based kernels are related as follows :

$$b'(v) = b'(L^3) = b(L) \quad (\text{B.2})$$

$$a'(v, v') = a'(L^3, L'^3) = b(L, L'). \quad (\text{B.3})$$

Birth rate due to aggregation :

$$\begin{aligned} B'_a(v; t) &= \frac{1}{2} \int_0^v a'(v - v', v')f'(v - v', t)f'(v', t)dv' \\ \implies B'_a(L^3; t) &= \frac{1}{2} \int_0^L a((L^3 - L'^3)^{1/3}, L')f'(L^3 - L'^3; t)f'(L'^3; t)3L'^2 dL' \\ &= \frac{1}{2} \int_0^L a((L^3 - L'^3)^{1/3}, L') \frac{3(L^3 - L'^3)^{2/3}}{3(L^3 - L'^3)^{2/3}} f'(L^3 - L'^3, t)f(L', t)L' dL' \end{aligned}$$

$$= \frac{1}{2} \int_0^L a((L^3 - L'^3)^{1/3}, L') \frac{f((L^3 - L'^3)^{2/3}; t)}{3(L^3 - L'^3)^{2/3}} f(L', t) dL' \quad (\text{B.4})$$

and thus using $B_a(L; t) = 3L^2 B'_a(L^3; t)$ we find that

$$B_a(L; t) = \frac{L^2}{2} \int_0^L \frac{a((L^3 - L'^3)^{1/3}, L')}{(L^3 - L'^3)^{2/3}} f((L^3 - L'^3)^{2/3}; t) f(L', t) dL'. \quad (\text{B.5})$$

Death rate due to aggregation :

$$\begin{aligned} D'_a(v; t) &= f'(v, t) \int_0^\infty a'(v, v') f'(v', t) dv' \\ \implies D'_a(L^3; t) &= f'(L^3, t) \int_0^\infty a'(L^3, L'^3) f'(L'^3, t) 3L'^2 dL' \\ &= f'(L^3, t) \int_0^\infty a'(L^3, L'^3) f(L', t) 3L'^2 dv' \end{aligned} \quad (\text{B.6})$$

and thus using $D_a(L; t) = 3L^2 D'_a(L^3; t)$ we find that

$$D_a(L; t) = f(L, t) \int_0^\infty a(L, L') f(L', t) dL'. \quad (\text{B.7})$$

Birth rate due to breakage :

$$\begin{aligned} B'_b(v; t) &= \int_v^\infty b'(v') \beta'(v | v') f'(v', t) dv' \\ \implies B'_b(L^3; t) &= \int_L^\infty b'(L'^3) \beta'(L^3 | L'^3) f'(L'^3, t) 3L'^2 dL' \end{aligned} \quad (\text{B.8})$$

and thus using $B_b(L; t) = 3L^2 B'_b(L^3; t)$ we find that

$$B_b(L; t) = \int_L^\infty b(L) \beta(L | L') f(L', t) dL' \quad (\text{B.9})$$

where $\beta(L | L') = 3L^2 \beta'(L | L')$.

Death rate due to breakage :

$$D'_b(v; t) = b'(v) f'(v; t) \quad (\text{B.10})$$

and thus using $D_b(L; t) = 3L^2 D'_b(L^3; t)$ we find that

$$D_b(L; t) = b(L) f(L; t). \quad (\text{B.11})$$

Appendix C

C.1 Product Difference Algorithm (P-D Algorithm)

The procedure used to find weights (w_i) and abscissas (L_i) from the moments is based on the PD algorithm [59]. The first step is the construction of a matrix P with components $P_{i,j}$ starting from the moments. The components in the first column of P are

$$P_{i,1} = \delta_{i,1}, \quad i \in 1, \dots, 2N + 1, \quad (\text{C.1})$$

where $\delta_{i,1}$ is the Kronecker delta. The components in the second column of P are

$$P_{i,2} = (-1)^{i-1} m_{i-1}, \quad i \in 1, \dots, 2N + 1. \quad (\text{C.2})$$

Since the final weights can be corrected by multiplying the true m_0 , the calculations can be done assuming a normalized distribution (i.e., $m_0 = 1$). Then the remaining components are found from the PD algorithm :

$$\begin{aligned} P_{i,j} &= O_{1,j-1} P_{i+1,j-2} - P_{1,j-2} P_{i+1,j-1}, \\ j &\in 3, \dots, 2N + 1 \quad \text{and} \quad i \in 1, \dots, 2N + 2 - j. \end{aligned} \quad (\text{C.3})$$

If, for example, $N=2$ then P becomes

$$\begin{bmatrix} 1 & 1 & m_1 & m_2 - m_1^2 & m_3 m_1 - m_2^2 \\ 0 & -m_1 & -m_2 & -m_3 + m_2 m_1 & 0 \\ 0 & m_2 & m_3 & 0 & 0 \\ 0 & -m_3 & 0 & 0 & 0 \\ 0 & 0 & 0 & 0 & 0 \end{bmatrix}.$$

The coefficients of the continued fraction (α_i) are generated by setting the first element equal to zero ($\alpha_1 = 0$) and computing the others according to

the following recursive relationship :

$$\alpha_i = \frac{P_{1,i+1}}{P_{1,i}P_{1,i-1}}, \quad i \in 2, \dots, 2N. \quad (\text{C.4})$$

A symmetric tridiagonal matrix is obtained from sums and products of α_i ,

$$a_i = \alpha_{2i} + \alpha_{2i-1}, \quad i \in 1, \dots, 2N - 1, \quad (\text{C.5})$$

and

$$b_i = -\sqrt{\alpha_{2i+1}\alpha_{2i-1}}, \quad i \in 1, \dots, 2N - 2, \quad (\text{C.6})$$

where a_i and b_i are the diagonal and the codiagonal of the Jacobi matrix respectively. Once the tridiagonal matrix is determined, generation of the weights and abscissas is done by finding its eigenvalues and eigenvectors. In fact, the eigenvalues are the abscissas and the weights can be found as

$$w_j = m_0 v_{j1}^2 \quad (\text{C.7})$$

where v_{j1} is the first component of the j th eigenvector v_j .

List of Figures

1.1	Rotating disc contactor (RDC).	2
2.1	Flow domain with non-structured grid	21
3.1	The sauter mean diameter for the breakage only.	46
3.2	The sauter mean diameter for the breakage and aggregation both.	46
3.3	The sauter mean diameter for the breakage only.	50
3.4	The sauter mean diameter for the breakage and aggregation both.	51
3.5	The sauter mean diameter for the breakage only.	54
3.6	The sauter mean diameter for the breakage and aggregation both.	55
3.7	The sauter mean diameter for the breakage only.	59
3.8	The sauter mean diameter for both the breakage and aggre- gation.	60
3.9	The comparison of the sauter mean diameter for both the breakage and aggregation for different number of primary and secondary particles.	60
3.10	Average number concentration using different primary parti- cles as predicted by the SQMOM.	61
3.11	The sauter mean diameter for the breakage only.	62
3.12	The sauter mean diameter for the breakage only.	64
3.13	The sauter mean diameter for both the breakage and aggre- gation.	64
3.14	The number density for the product coalescence kernel.	65

3.15	The number density for the additive coalescence kernel and linear breakage kernel.	65
3.16	The average diameter for the additive coalescence kernel and linear breakage kernel.	66
3.17	The number density for the productive coalescence kernel and linear breakage kernel.	66
3.18	The average diameter for the productive coalescence kernel and linear breakage kernel.	67
3.19	The sauter mean diameter for the breakage only.	68
3.20	The sauter mean diameter for the aggregation and breakage both.	68
4.1	The number density of the droplets without breakage and coalescence kernels.	73
4.2	The volume concentration of the droplets without breakage and coalescence kernels.	73
4.3	The average velocity of the droplets without breakage and coalescence kernels.	74
4.4	The velocity of the continuous phase without breakage and coalescence kernels.	74
4.5	The average diameter of the droplets without breakage and coalescence kernels.	75
4.6	The droplets velocity profile on the different time frames.	75
4.7	The number density of the droplets with constant breakage kernel 0.03 and coalescence kernel 10^{-6}	77
4.8	The volume concentration of the droplets with constant breakage kernel 0.03 and coalescence kernel 10^{-6}	77
4.9	The average velocity of the droplets with constant breakage kernel 0.03 and coalescence kernel 10^{-6}	78
4.10	The average diameter of the droplets with constant breakage kernel 0.03 and coalescence kernel 10^{-6}	78
4.11	The number density of the droplets with constant breakage kernel 0.03 and coalescence kernel 10^{-7}	79
4.12	The volume concentration of the droplets with constant breakage kernel 0.03 and coalescence kernel 10^{-7}	79

4.13	The average velocity of the droplets with constant breakage kernel 0.03 and coalescence kernel 10^{-7}	80
4.14	The average diameter of the droplets with constant breakage kernel 0.03 and coalescence kernel 10^{-7}	81
4.15	The number density of the droplets with non-constant breakage kernel and coalescence kernel.	81
4.16	The volume concentration of the droplets with non-constant breakage kernel and coalescence kernel.	82
4.17	The average velocity of the droplets with non-constant breakage kernel and coalescence kernel.	82
4.18	The average diameter of the droplets with non-constant breakage kernel and coalescence kernel.	83
4.19	Simulated and experimental [71] hold-up profiles in a pilot plant RDC column at different rotor speeds using the system water/n-butyl acetate.	85
4.20	Simulated and experimental [71] average diameter in a pilot plant RDC column at different rotor speeds using the system water/n-butyl acetate.	86
4.21	Simulated velocity profiles of dispersed phase in a pilot plant RDC column at different rotor speed using the system water/n-butyl acetate.	86
4.22	Simulated and experimental [71] hold-up profiles in a pilot plant RDC column at rotor speed 200 rpm at different FPM particles numbers 100 and 200 using the system water/n-butyl acetate.	87
4.23	Simulated and experimental [71] average diameters in a pilot plant RDC column at rotor speed 200 rpm at different FPM particles numbers 100 and 200 using the system water/n-butyl acetate.	88
4.24	Simulated average number densities of droplets in a pilot plant RDC column at rotor speed 200 rpm at different FPM particles numbers 100 and 200 using the system water/n-butyl acetate.	88
4.25	Comparison of simulated and experimental [73] hold-up profiles of droplets in a pilot plant RDC at 220 rpm.	89
4.26	Comparison of simulated and experimental [73] droplet average diameter (d_{30}) of droplets in a pilot plant RDC DN-150 at 220 rpm.	90

4.27	Kuehni Column.	91
4.28	Comparison of simulated and experimental [74] hold - up profiles for Kuehni column DN-150 with inflow rates of continuous phase and dispersed phase 125 [l/h] and 130 [l/h] respectively at 160 rpm.	92
4.29	Comparison of simulated and experimental [74] hold - up profiles for Kuehni column DN-150 with inflow rates of continuous phase and dispersed phase 125 [l/h] and 160 [l/h] respectively at 160 rpm.	93
4.30	Comparison of simulated and experimental [74] hold - up profiles for Kuehni column DN-150 with inflow rates of continuous phase and dispersed phase 125 [l/h] and 190 [l/h] respectively at 160 rpm.	94
4.31	The number density of the droplets with constant breakage kernel 0.03 and coalescence kernel 10^{-6}	94
4.32	The volume concentration of the droplets with constant breakage kernel 0.03 and coalescence kernel 10^{-6}	95
4.33	The average velocity of the droplets with constant breakage kernel 0.03 and coalescence kernel 10^{-6}	95
4.34	The average diameter of the droplets with constant breakage kernel 0.03 and coalescence kernel 10^{-6}	96
4.35	The average diameter of the droplets with constant breakage kernel 0.03 and coalescence kernel 10^{-6}	96
4.36	The average number density of the droplets with non-constant breakage kernel $0.1 \times d^3$ and coalescence kernel $2(d^3 + d'^3)$	97
4.37	The volume concentration density of the droplets with non-constant breakage kernel $0.1 \times d^3$ and coalescence kernel $2(d^3 + d'^3)$	98
4.38	The velocity of the droplets with non-constant breakage kernel $0.1 \times d^3$ and coalescence kernel $2(d^3 + d'^3)$	98
4.39	The volume concentration density of the droplets with non-constant breakage kernel $0.1 \times d^3$ and coalescence kernel $2(d^3 + d'^3)$	99
4.40	Simulated and experimental [71] hold-up profiles in a pilot plant RDC column at rotor speed 150rpm using the system water/n-butyl acetate.	100

4.41	Simulated and experimental [71] average diameter of droplets in a pilot plant RDC column at rotor speed 150 rpm using the system water/n-butyl acetate.	101
4.42	Simulated and experimental [71] hold-up profiles in a pilot plant RDC column at rotor speed 200 rpm using the system water/n-butyl acetate.	102
4.43	Simulated and experimental [71] average diameter of droplets in a pilot plant RDC column at rotor speed 200 rpm using the system water/n-butyl acetate.	103
4.44	Simulated velocity profile of droplets in a pilot plant RDC column at rotor speed 200 rpm using the system water/n-butyl acetate.	104
5.1	The comparison of the solute concentrations of the dispersed phase for different coalescence and breakage kernels.	106
5.2	The comparison of the solute concentrations of the continuous phase for different coalescence and breakage kernels.	106
5.3	The comparison of the solute concentrations of the dispersed phase for different mass transfer coefficient.	107
5.4	The comparison of the solute concentrations of the continuous phase for different mass transfer coefficient.	108
5.5	Comparison of simulated and experimental [73] concentration profiles of droplets in a pilot plant RDC at 220 rpm.	109
5.6	Comparison of simulated and experimental [73] concentration profiles of the continuous phase in a pilot plant RDC at 220 rpm.	110
5.7	Concentration profile for the dispersed phase in a Kuehni column (experimental data are from Zamponi [74]).	111
5.8	Concentration profile for the continuous phase in a Kuehni column (experimental data are from Schmidt [72]).	111

List of Tables

3.1	Error analysis of MPOSPM for the case of breakage only . . .	67
3.2	Error analysis of MPOSPM for the case of both the breakage and aggregation	69
3.3	Comparison of numerical methods to solve PBE for the case of breakage only	69
3.4	Comparison of numerical methods to solve PBE for the case of breakage and aggregation both.	70
4.1	Initial and inlet boundary conditions for the RDC liquid-liquid extraction columns.	72
4.2	Column Geometry	72
4.3	Physical Quantities	76
4.4	Physical Quantities	90

Bibliography

- [1] S. Mohanty, Modeling of liquid-liquid extraction column : a review, *Review Eng. Sci.* **16** (2000) 199-248.
- [2] H. -J. Bart, Reactive extraction in stirred columns : a review, *Chem. Eng. and Tech.* **26** (2003) 723-731.
- [3] C. Gourdon, G. Casamatta & G. Muratet, Population based modeling of solvent extraction columns, *Godfrey, J. C. Slater, M. J. (Eds.), Liquid-liquid extraction equipment, John Wiley & Sons, New York* (1994) 137-226.
- [4] M. M. Attarakih, H. -J. Bart, L. G. Lager & N. M. Faqir, LLECMOD : A Windows-based program for hydrodynamics and simulation of liquid-liquid extraction columns, *Chem. Eng. Proc.* **45(2)** (2006) 113-123.
- [5] M. M. Attarakih, H. -J. Bart & N. M. Faqir, Numerical solution of the bivariate population balance equation for the interacting hydrodynamics and mass transfer in liquid-liquid extraction column, *Chem. Eng. Proc.* **61(1)** (2006) 113-123.
- [6] S. A. Schmidt, M. Simon, M. M. Attarakih, L. Lager & H. -J. Bart, Droplet population balance modeling - hydrodynamics and mass transfer, *Chem. Eng. Sci.* **61(1)** (2006) 246-256.
- [7] C. Drumm & H. -J. Bart, Hydrodynamics in a RDC extractor : single and two phase PIV measurements and CFD simulations, *Chem. Eng. Tech.* **29(11)** (2006) 1-8.
- [8] C. Drumm, S. Tiwari, J. Kuhnert & H. -J. Bart, Finite pointset method for simulation of the liquid-liquid flow field in an extractor *Comp. Chem. Eng.* **32** (2008) 2946-2957.
- [9] C. Drumm, M. M. Attarakih, & H. -J. Bart, Coupling of CFD with DPBM for a RDC extractor, *Chem. Eng. Sci.* **64** (2009) 721-732.
- [10] A. Vikhansky, M. Kraft, M. Simon, S. Schmidt & H. -J. Bart, Droplets population balance in a rotating disc contactor : an inverse problem approach, *AIChE Journal* **52(4)** (2006) 1441-1450.
- [11] L. B. Lucy, A numerical approach to the testing of the fission hypothesis, *Astron. J.* **82** (1977) 1013-1024.

- [12] R. A. Gingold & J. J. Monaghan, *MNRAS* **181** (1977) 375.
- [13] J. J. Monaghan, Smooth particle hydrodynamics, *Annu. Rev. Astron.* **30** (1992) 543-574.
- [14] J. P. Morris, Simulating surface tension with smoother particle hydrodynamics, *Int. J. Num. Meth. Fluids* **33** (2000) 333-353 J. P. Morris, *J. Comput. Appl. Math.* (2000) 155(2)-263.
- [15] T. Belytschko, Y. Krongauz, D. Organ, M. Flemming & P. Krysl, Meshless methods : An overview and recent developments, *Comput. Methods Appl. Mech. Eng.* (1996).
- [16] G. A. Dilts, Moving least squares particle hydrodynamics I, consistency and stability, *Hydrodynamics methods group report, Los Alamos National Laboratory* (1996).
- [17] J. Kuhnert, General smoothed particle hydrodynamics, *PhD Thesis, University of Kiaserslautern, Germany* (1999).
- [18] S. Tiwari & S. Manservigi, Modeling incompressible Navier-Stokes flows by LSQ-SPH, *The Nepali Math. Sci. report* **20** (2002).
- [19] S. Tiwari & J. Kuhnert, Modeling of two-phase flows with surface tension by Finite Pointset Method (FPM), *J. Comp. Appl. Math.* (2007) 203-376.
- [20] S. Tiwari, C. Drumm, V. K. Sharma, J. Kuhnert, M. M. Attarakih, A. Klar & H.-J. Bart, A meshfree CFD-Population balance equation coupled model, *6th International Conference on CFD in Oil & Gas, Metallurgical and Process Industries SINTEF/NTNU, Trondheim, Norway* (2008).
- [21] V. K. Sharma, S. Tiwari, M. M. Attarakih, M. Jaradat, A. Klar, J. Kuhnert & H.-J. Bart, Simulation of two phase flow with incorporated population balance equation using a meshfree method, *ESCAPE19* (2009).
- [22] M. M. Attarakih, C. Drumm & H.-J. Bart, Solution of the population balance equation using the sectional quadrature method of moments, *Chem. Eng. Sci.* **64** (2009) 742-752.
- [23] C. Drumm, M. M. Attarakih, S. Tiwari, J. Kuhnert & H.-J. Bart, Implementation of the section quadrature method of moments in a CFD code, *6th Int. Conf. on CFD in Oil and Gas, Metallurgical and Process Industries, CFD08* (2008) 80-90.
- [24] M. M. Attarakih, M. Jaradat, C. Drumm, H.-J. Bart, S. Tiwari, V. K. Sharma, J. Kuhnert & A. Klar, Solution of the Population Balance Equation using the One Primary and One Secondary Particle Method (OPOSPM), *ESCAPE19* (2009).
- [25] M. M. Attarakih, M. Jaradat, C. Drumm, H.-J. Bart, S. Tiwari, V. K. Sharma, J. Kuhnert & A. Klar, A Multivariate Population Balance Model for Liquid Extraction Columns, *ESCAPE19* (2009).

- [26] M. M. Attarakih, V.K. Sharma, M. Jaradat, C. Drumm, H.-J. Bart, S. Tiwari, J. Kuhnert & A. Klar, A multivariate sectional quadrature method of moments for the solution of the population balance equation, *Escape20* (2010).
- [27] V. K. Sharma, S. Tiwari, M. M. Attarakih, M. Jaradat, A. Klar, J. Kuhnert & H.- J. Bart, A spatially meshfree population balance model for the simulation of liquid extraction columns, *4th International Conference on Population Balance Modelling hosted by the Max Plank Institute for Dynamics of Complex Technical Systems, Berlin, Germany* (2010).
- [28] M. M. Attarakih, V. K. Sharma, M. Jaradat, H.-J. Bart & J. Kuhnert, Solution of the population balance equation using the Cumulative Quadrature Method of Moments (CQMOM), *4th International Conference on Population Balance Modelling hosted by the Max Plank Institute for Dynamics of Complex Technical Systems, Berlin, Germany* (2010).
- [29] M. Jaradat, V. K. Sharma, M. Attarakih, M. Hlawitschka & H.-J. Bart, A multivariate population balance model for liquid extraction columns, *4th International Conference on Population Balance Modelling hosted by the Max Plank Institute for Dynamics of Complex Technical Systems, Berlin, Germany* (2010).
- [30] D. Zeidan, M.M. Attarakih, J. Kuhnert, S. Tiwari, V. K. Sharma, C. Drumm & H.-J. Bart, On a high-resolution Godunov Method of two-phase flow in liquid-liquid extraction column, *accepted in International Journal of Computational Methods* (2010).
- [31] M. J. Hounslow, R. L. Ryall & V. R. Marshall, A discretized population balance for nucleation, growth and aggregation, *AICHE J.* **34(11)** (1988) 1821-1832.
- [32] R. McGraw, Description of aerosol dynamics by the quadrature method of moments, *Aerosol Sci. & Tech.* **27(2)** (1997) 255-265.
- [33] S. Lo., Application of population balance to CFD modelling of gas-liquid reactors, *Proc. "Trends in numerical and physical modelling for industrial multiphase flows", Corsica France* (2002)
- [34] F. Wang & Z. -S. Mao, Numerical and experimental investigation of liquid-liquid two-phase flow in stirred tanks, *Ind. Eng. Chem. Res.* **44** (2005) 5776.
- [35] E. Krepper, T. Frank, D. Lucas, H. -M. Prasser & P. J. Zwart, Inhomogeneous MUSIG model - a population balance approach for polydispersed bubbly flows, *Proc. of the ICMF-2007, M. Sommerfeld (Ed.), 6th International conference on Multiphase Flow, Leipzig* (2007).
- [36] D. Ramkrishna, Population Balances, *Academic Press, San Diego* (2000).
- [37] G. Modes, Grundsatzliche Studie zur Populationsdynamik einer Extraktionsskolone auf Basis von Einzeltropfenuntersuchungen, Aachen : Shaker Verlag (2000).

- [38] T. C. Lo, M.H.I. Baird & C. Hanson, Handbook of solvent extraction, *New York: John Wiley and Sons* (1983).
- [39] A. E. Handlos & T. Baron, Mass transfer from drops in liquid extraction, *AIChE J.* **3** (1957) 127-136.
- [40] A. Kumar & S. Hartland, Correlations for prediction of mass transfer coefficients in single drop systems and liquid-liquid extraction columns, *Trans. Inst. Chem. Eng.* **77A** (1999) 372-384.
- [41] S. H. Zhang, S. C. Yu, Y. C. Zhou, & Y. F. Su, A model for liquid-liquid extraction column performance- the influence of drop size distribution on extraction efficiency, *Can. J. Chem. Eng.* **63** (1985) 212-226.
- [42] O. Weinstein, R. Semiat, & D. R. Lewin, Modeling, simulation and control of liqui-liquid extraction columns, *Chem. Eng. Sci.* **53** (1998) 325-339.
- [43] T. Wang & J. Wang, Numerical simulation of gas-liquid mass transfer in bubble columns with a CFD-PBM coupled model, *Chem. Eng. Sci.* **62** 7107-7118.
- [44] L. Schiller & Z. Naumann, A drag coefficient correlation, *Z. Ver. Deutsch. Ing.* **77** (1935) 318.
- [45] S. A. Schmidt, M. Simon, M. M. Attarakih, L. Lagar & H. -J. Bart, Droplet population balance modelling - hydrodynamics and mass transfer, *Chem. Eng. Sci.* **61** (2006) 246-256.
- [46] C. B. Laney, Computational gasdynamics, *Cambridge University Press*.
- [47] P. Chadwick, Continuum mechanics : concise theory and problems, *Wiley*.
- [48] V. V. Sychev, Asymptotic theory of seprated flows, *Cambridge University Press*.
- [49] T. Liszka & J. Orkisz, The finite difference method on arbitrary irregular grid and its application in applied mechanics, *Comp. and Struc.* **11** (1980) 83.
- [50] S. Tiwari & J. Kuhnert, Finite pointset method based on the projection method for simulations of the incompressible Navier-Stokes equations, (*M. Griebel and M. A. Schweitzer, eds.*), *Lec. Notes in Comp. Sci. and Eng.* **26**, Springer (2002) 373-387.
- [51] O. Iliev & S. Tiwari, A generalized (meshfree) finite difference discretization for elliptic interface problems, (I. Dimov, I. Lirkov, S. Margenov and Z. Zlatev, eds.), *Num. Methods and App., Lecture notes in Comp. Sci., Springer* (2002) 480.
- [52] B. J. McCoy & G. Madras, Analytical solution for a population balance equation with aggregation and fragmentation, *Chem. Eng. Sci.* **58(13)** (2003) 3049-3051.

- [53] R. J. Batterham, J. S. Hall & G. Barton, Pelletizing kinetics and simulation of full-scale balling circuits, *3rd Int. Symp. on Agglo., Nuernberg Germany* **A136** (1981).
- [54] M. J. Hounslow, R. L. Ryall & V. R. Marshall, A discretized population balance for nucleation, growth and aggregation, *AICHE J.* **34(11)** (1988) 1821-1832.
- [55] J. D. Lister, D. J. Smith & M. J. Hounslow, Adjustable discretized population balance for growth and aggregation, *AICHE J.* **41(3)** (1995) 591-603.
- [56] S. Kumar & D. Ramkrishna, On the solution of population balance equations by discretization - i. a fixed pivot technique, *Chem. Eng. Sci.* **51(8)** (1996a) 1311-1332.
- [57] H. M. Hulbert & S. Katz, *Some problems in particle technology*, *Chem. Eng. Sci.* **19** (1964) 555-574.
- [58] R. B. Diemer & J. H. Olson, A moment methodology for coagulation and breakage problems : part ii - moment models and distribution reconstruction, *Chem. Eng. Sci.* **57** (2002) 2211-2228.
- [59] R. G. Gordon, Error bounds in equilibrium statistical mechanics, *J. of Math. Phy.* **9** (1968) 655-663.
- [60] D. L. Marchisio, J. T. Pikturka, R. O. Fox & R. D. Vigil, Quadrature method of moments for population balance equations, *AICHE J.* **49(5)** (2003a) 1266-1276.
- [61] J. C. Barrett & N. A. Webb, A comparison of some approximate methods for solving the aerosol general dynamic equation, *J. of Aerosol Sci.* **29** (1998) 31-39.
- [62] D. L. Wright, R. McGraw & D. E. Rosner, Bivariate extension of the quadrature method of moments for modeling simultaneous coagulation and sintering of particle populations, *J. of Coll. and Int. Sci.* **236** (2001) 242-251.
- [63] D.E. Rosner & J.J. Pykonen, Bi-variate Moment Simulation of Coagulating and Sintering Nano-particles in Flames, *AICHE J.* **48(3)** (2002) 476-491.
- [64] V. N. Piskunov, A. I. Golubev, J. C. Barrett & N. A. Ismallova, The generalized approximation method for modeling coagulation kinetics?Part 2: comparison with other methods, *J. of Aerosol Sci.* **33** (2002) 65-75.
- [65] D. L. Marchisio, R. O. Fox, Solution of population balance equations using the direct quadrature method of moments, *J. of Aerosol Sci.* **36** (2005) 43-73.
- [66] S. Bove, Computational fluid dynamics of gas-liquid flows including bubble population balances, *Ph. D. Thesis, Aalborg University Esbjerg, Denmark* (2005).

- [67] S. Motz, A. Mitrovic & E. -D. Gilles, Comparison of numerical methods for the simulation of dispersed phase systems, *Chem. Eng. Sci.* **57** (2002) 4329-4344.
- [68] G. Modes, Grundsatzliche studie zur populationsdynamik einer extraktionskolone auf basis von einzeltröpfenuntersuchungen, *Aachen : Shaker Verlag*.
- [69] V. Cauwenberg, J. Degreve & M. J. Slater, The interaction of solute transfer contaminants and drop break-up in rotating disc contactors : part II, The coupling of mass transfer and breakage process via interfacial tension, *Canadian J. of Chem. Eng.* **75** (1997) 1056-1066.
- [70] C. Couglaloglou & L. L. Tavlarides, Description of interaction processes in agitated liquid-liquid dispersions, *Chem. Eng. Sci.* **32** (1977) 1289-1297.
- [71] M. M. Attarakih, H. -J. Bart, T. Steinmetz, M. Dietzen & N. M. Faqir, LLECMOD : A bivariate population balance simulation tool for liquid-liquid extraction columns, *The Open Chem. Eng. J.* **2** (2008) 10-34.
- [72] S. A. Schmidt, Populationdynamische simulation geruehrter extraktionskolonnen auf basis von einzeltröpfen- und tröpfenschwarmuntersuchungen, *Diss., TU Kaiserslautern, Germany* (2005).
- [73] G. Garthe, Fluid dynamics and mass transfer and swarm of particles in extraction column, *Diss., TU Muenchen, Germany* (2006).
- [74] G. Zamponi, J. Stichlmair, A. Gerstlauer & E. -E. Gilles, Simulation of the transient behaviour of a stirred liquid/liquid extraction column, *Comp. Chem. Eng.* **20** (1996) 963-968.
- [75] A. E. Handlos & T. Baron, Mass and heat transfer from drops in liquid-liquid extraction, *AICHE J.* **3(1)** (1957) 127-135.
- [76] P. M. Heertjes, W. A. Holve & H. Talsma, Mass transfer between isobutanol and water in a spray column, *Chem. Eng. Sci.* **3** (1954) 122-142.
- [77] S. A. Schmidt, M. Simon, M. M. Attarakih, L. Lager & H. -J. Bart, Droplet population balance modeling - hydrodynamics and mass transfer, *Chem. Eng. Sci.* **61** (2006) 246-256.
- [78] D. L. Marchisio, R. D. Vigil & R. O. Fox, Quadrature method of moments for aggregation-breakage processes, *Journal of Colloid and Interface Science* **258** (2003) 322-334.

CURRICULUM VITAE

Personal Information

Name Vikash Kumar Sharma
Date of Birth 04 Apr 1982
Place of Birth Bulandshahr, India

Education

Oct 2007 – till date : Doctorate studies at Department of Mathematics,
Technische Universität Kaiserslautern, Germany

2004 – 2006 : Master of Technology in Industrial Mathematics
and Scientific Computing (9.37 GPA),
Indian Institute of Technology Madras, India

2001 – 2003 : Master of Science in Mathematics
(75%), Aligarh Muslim University, India

1998 – 2001 : Bachelor of Science in Physics, Chemistry and
Mathematics (72.2%),
C. C. S. University Meerut, India

1987-1998 : Primary and Secondary school : Bulandshahr,
India

Academic Honors

- Deutscher Akademischer Austausch Dienst (DAAD) scholarship
- Institute medal and Prof. Helmut Neunzert award for securing first rank in M.Tech.
- Ramanujam award for securing highest CGPA in first three semester of M.Tech.
- Secured a percentile of 98.49 in Graduate Aptitude Test in Engineering in India with an all India rank of 23 in 2004
- Half-time Teaching Assistantship for two years during M.Tech. programme
- Scholarship award during M.Sc. for securing 3rd rank in scholarship test in AMU